



AFRL-RY-WP-TR-2014-0230

INFLUENCE OF SPECTRAL TRANSFER PROCESSES IN COMPRESSIBLE LOW FREQUENCY PLASMA TURBULENCE ON SCATTERING AND REFRACTION OF ELECTROMAGNETIC SIGNALS

Vladimir Sotnikov

**Antennas & Electromagnetics Technology Branch
Multispectral Sensing & Detection Division**

**JANUARY 2015
Final Report**

Approved for public release; distribution unlimited.

See additional restrictions described on inside pages

STINFO COPY

**AIR FORCE RESEARCH LABORATORY
SENSORS DIRECTORATE
WRIGHT-PATTERSON AIR FORCE BASE, OH 45433-7320
AIR FORCE MATERIEL COMMAND
UNITED STATES AIR FORCE**

NOTICE AND SIGNATURE PAGE

Using Government drawings, specifications, or other data included in this document for any purpose other than Government procurement does not in any way obligate the U.S. Government. The fact that the Government formulated or supplied the drawings, specifications, or other data does not license the holder or any other person or corporation; or convey any rights or permission to manufacture, use, or sell any patented invention that may relate to them.

This report was cleared for public release by the USAF 88th Air Base Wing (88 ABW) Public Affairs Office (PAO) and is available to the general public, including foreign nationals.

Copies may be obtained from the Defense Technical Information Center (DTIC)
[\(http://www.dtic.mil\)](http://www.dtic.mil).

**AFRL-RY-WP-TR-2014-0230 HAS BEEN REVIEWED AND IS APPROVED FOR PUBLICATION
IN ACCORDANCE WITH ASSIGNED DISTRIBUTION STATEMENT.**

*//Signature//

VLADIMIR I. SOTNIKOV, Program Manager
Antenna & Electromagnetic Technology Branch
Multispectral Sensing & Detection Division

//Signature//

TONY C. KIM, Branch Chief
Antenna & Electromagnetic Technology Branch
Multispectral Sensing & Detection Division

*//Signature//

TRACY W. JOHNSTON, Division Chief
Multispectral Sensing & Detection Division
Sensors Directorate

This report is published in the interest of scientific and technical information exchange, and its publication does not constitute the Government's approval or disapproval of its ideas or findings.

*Disseminated copies will show “//signature//” stamped or typed above the signature blocks.

REPORT DOCUMENTATION PAGE

*Form Approved
OMB No. 0704-0188*

The public reporting burden for this collection of information is estimated to average 1 hour per response, including the time for reviewing instructions, searching existing data sources, gathering and maintaining the data needed, and completing and reviewing the collection of information. Send comments regarding this burden estimate or any other aspect of this collection of information, including suggestions for reducing this burden, to Department of Defense, Washington Headquarters Services, Directorate for Information Operations and Reports (0704-0188), 1215 Jefferson Davis Highway, Suite 1202, Arlington, VA 22202-4302. Respondents should be aware that notwithstanding any other provision of law, no person shall be subject to any penalty for failing to comply with a collection of information if it does not display a currently valid OMB control number. **PLEASE DO NOT RETURN YOUR FORM TO THE ABOVE ADDRESS.**

1. REPORT DATE (<i>DD-MM-YY</i>) January 2015			2. REPORT TYPE Final		3. DATES COVERED (<i>From - To</i>) 1 October 2011 – 30 June 2014	
4. TITLE AND SUBTITLE INFLUENCE OF SPECTRAL TRANSFER PROCESSES IN COMPRESSIBLE LOW FREQUENCY PLASMA TURBULENCE ON SCATTERING AND REFRACTION OF ELECTROMAGNETIC SIGNALS			5a. CONTRACT NUMBER In-house			
			5b. GRANT NUMBER			
			5c. PROGRAM ELEMENT NUMBER 61102F			
			5d. PROJECT NUMBER 3001			
			5e. TASK NUMBER 12RY07COR			
			5f. WORK UNIT NUMBER Y0R7			
6. AUTHOR(S) Vladimir Sotnikov			8. PERFORMING ORGANIZATION NAME(S) AND ADDRESS(ES) Antennas & Electromagnetics Technology Branch (AFRL/RYMH) Multispectral Sensing & Detection Division Air Force Research Laboratory, Sensors Directorate Wright-Patterson Air Force Base, OH 45433-7320 Air Force Materiel Command, United States Air Force			
			8. PERFORMING ORGANIZATION REPORT NUMBER AFRL-RY-WP-TR-2014-0230			
9. SPONSORING/MONITORING AGENCY NAME(S) AND ADDRESS(ES) Air Force Research Laboratory Sensors Directorate Wright-Patterson Air Force Base, OH 45433-7320 Air Force Materiel Command United States Air Force			10. SPONSORING/MONITORING AGENCY ACRONYM(S) AFRL/RYMH			
			11. SPONSORING/MONITORING AGENCY REPORT NUMBER(S) AFRL-RY-WP-TR-2014-0230			
12. DISTRIBUTION/AVAILABILITY STATEMENT Approved for public release; distribution unlimited						
13. SUPPLEMENTARY NOTES PAO Case Number 88ABW-2014-5801, Clearance Date 5 December 2014. Report contains color.						
14. ABSTRACT <p>The overall goal of this research is to analyze influence of plasma turbulence on hypersonic sensor systems and NGOTHR applications and to meet the Air Force's ever-increasing demand for reduced cost, size, weight, and power (CSWAP) while maintaining or increasing system functionality. This basic research effort consists of several sub-tasks that use experiments, analytical and numerical methods to examine linear and nonlinear stages of instabilities of plasma flow with velocity shear. Refraction and scattering of high frequency electromagnetic waves on nonlinear vortex structures produced in the process of instability development will be analyzed as well.</p>						
15. SUBJECT TERMS plasma physics, ionospheric plasmas, electromagnetic scattering, plasma turbulence, plasma perturbations						
16. SECURITY CLASSIFICATION OF: a. REPORT Unclassified		17. LIMITATION OF ABSTRACT: b. ABSTRACT Unclassified c. THIS PAGE Unclassified SAR		18. NUMBER OF PAGES 84	19a. NAME OF RESPONSIBLE PERSON (Monitor) Vladimir Sotnikov 19b. TELEPHONE NUMBER (Include Area Code) N/A	

Table of Contents

Section	Page
List of Figures	iv
List of Tables	v
1.0 EXECUTIVE SUMMARY.....	1
2.0 INTRODUCTION.....	2
3.0 EXCITATION OF LOWER HYBRID WAVES BY A FLOW WITH VELOCITY SHEAR.5	
3.1 Numerical Modeling of Parametric Interaction of Finite Amplitude Very Low Frequency (VLF) Waves.....	10
3.2 Analyses of the preliminary results	15
3.3 Modulation Instability of Lower-Hybrid waves.....	16
3.4 Modulation Instability of magnetosonic waves.....	22
3.5 Influence of electron- neutral collisions	25
4.0 ANALYTICAL AND EXPERIMENTAL INVESTIGATIONS HIGH FREQUENCY RF INTERACTION WITH LOCALIZED DENSITY STRUCTURES AT THE NAVAL RESEARCH LABORATORY.....	27
4.1 Linear Theory Extension	30
4.2 EM Scattering Experiments.....	33
4.3 EM Scattering Theory	39
4.4 Summary of NRL Effort.....	40
5.0 INTERCHANGE INSTABILITY.....	42
6.0 ADDITIONAL SCATTERING SIMULATIONS: RAY TRACING.....	56
6.1 Hamilton-Jacobi Ray Tracing approximation	56
6.2 Analytical Solution to Flute-Type Density Structures	58
6.3 Integration of Ray Tracing Algorithm with Vortex Solutions	60
6.4 Fokker-Planck description of Diffusion, Future Work.....	62
7.0 SCATTERING SIMULATIONS: PARTICLE IN CELL	64
References.....	
List of Symbols, Abbreviations, and Acronyms.....	75

List of Figures

Figure	Page
1. (left panel) World-line plots of the Cluster, DMSP, Polar satellites during the 18-March-2002 substorm event. The SAID channels from Cluster 1 (C1) are superimposed. Shown in the middle are (top) the C1/C4 outward electric field E_x in the inertial frame, (mid) C1/EDI 1-keV electron counts (thick line) and the cold plasma density n_0 (thin), and (bottom) C4/STAFF frequency-time spectrograms for the electric spectral power in $(\text{mV/m})^2/\text{Hz}$ (in log scale). Horizontal lines indicate the lower hybrid resonance (solid) and the 10th, 4th, and 2nd harmonics of the H^+ -ion gyrofrequency (dashed), derived from the observed magnetic field. Shown on the right are the features of the northern SAID channel from Polar. (top) the outward electric field, (mid) the plasma density, and (bottom) spectral amplitudes of electric fields at 32 (dashed line), 256 (thick), and 2048 (thin) Hz.....	3
2. In this figure a nonuniform electric field $E_{0x}(x)$ and an external magnetic field B_{0z} create a nonuniform electron flow with velocity shear along the y -direction	7
3. Normalized real frequency (solid black line) and growth rate (dashed red line) dependence on normalized collision frequency	8
4. Normalized real frequency (solid black line) and growth rate (dashed red line) dependence on normalized perpendicular wave number comparing local and non-local solutions	10
5. Dispersion relation for electromagnetic (magnetosonic) and electrostatic (lower-hybrid) waves; for $k < k^*$, the waves are magnetostatic and for $k > k^*$, lower-hybrid	11
6. In this figure a nonuniform electric field E0 and an external magnetic field B0 create a nonuniform electron flow with velocity shear along the y -direction.	15
7. Initial ($t = 0$) electric field distribution (squire of electric field) in dimensionless units (top) and 2D spatial spectrum of electric field (bottom).....	17
8. Electric field distribution (top) and its 2D spectrum (bottom) at time $t = 800$; instability just starts to develop.....	18
9. Electric field distribution (at the left) and its 2D spectrum (at the right) at time $t = 1800$; modulation instability is fully developed, amplitude is still small.....	19
10 . Electric field distibution distribution (at the left) and its 2D spectrum (at the right) at time $t = 2400$; amplitude is already large.	19
11. Electric field distribution (at the left) and its 2D spectrum (at the right) at time $t = 2600$; amplitude is very large.	20
12. Square of electric field and square of plasma density as a function of time.	20
13. Plasma density irregularity spatial distribution at the left) and its 2D spectrum (at the right) at time $t = 1600$; nonlinear term starts to play only when electric field increases up to 10-4.	21
14. Plasma density irregularity spatial distribution at the left) and its 2D spectrum (at the right) at time 1800; instability is fully developed, amplitude is still small.....	21
15. Plasma density irregularity spatial distribution at the left) and its 2D spectrum (at the right) at time $t = 2400$; amplitude is large already.....	22
16. Plasma density irregularity spatial distribution (at the left) and its 2D spectrum (at the right) at time $t=2600$. Amplitude is very large (more then 1), this stage is already out of model applicability.	22
17. Electric field distribution for lower-hybrid (at the left) and magnetosonic (at the right) waves after $t = 400$. The difference is visible. stochastic distribution of the field for the lower-hybrid waves in contrast to magnetosonic waves where amplitude of the field is order of magnitude larger and large-scale structure is developed.....	23

18. Electric field distribution for lower-hybrid (at the left) and magnetosonic (at the right) waves after $t = 600$. Instability is not developed for the lower-hybrid waves (still stochastic distribution). Large-scale objects start to align along y-axis for the magnetosonic waves. Amplitude of the magnetosonic waves is larger than amplitude of the lower-hybrid waves in two orders of magnitude.	23
19. Electric field distribution for lower-hybrid (at the left) and magnetosonic (at the right) waves after $t = 1000$. Modulation instability is developed for the lower-hybrid waves. Large-scale objects aligned along y-axis are still in place for the magnetosonic waves. Amplitude of the magnetosonic waves is larger than amplitude of the lower-hybrid waves in four orders of magnitude.	24
20. Electric field distribution for lower-hybrid (at the left) and magnetosonic (at the right) waves after $t = 1400$. Modulation instability is fully developed for the lower-hybrid waves and just start to develop for the magnetosonic waves. The amplitude of the wave is in the same order already.	24
21. Electric field distribution for lower-hybrid (at the left) and magnetosonic (at the right) waves after $t = 1600$. Starting from this time, the electric field distribution is almost indistinguishable between lower-hybrid and magnetosonic waves.	25
22. Plasma density distribution for lower-hybrid (at the left) and magnetosonic (at the right) waves after $t = 1600$. Starting from this time, the density distribution is almost indistinguishable between the two types of waves.	25
23. Squire of electric field density as a function of time for various values of normalized electron-neutral collision coefficient.	26
24. Schematic diagram of the experimental setup showing the two interpenetrating plasmas.	27
25. Radial profile of lower hybrid wave amplitude for the uniform density case and wave spectrum as inset.	28
26. Comparison of experimentally observed (filled symbols) and theoretically predicted (line) values of mode frequency as a function of magnetic field strength.	28
27. New linear plasma source installed in the SPSC.	29
28. Density profile produced by new linear plasma source with the width of the plot representing the size of the chamber. The blocking disk is shown at the top of the plot and the purple bars represent the size of the background plasma.	29
29. Typical eigenfunction magnitude (top pane) resulting from the numerical shooting code for experimental conditions with normalized electric field (middle pane) and density (bottom pane) profiles used in the calculations.	31
30. Comparison between trends in real frequency for theory and experimental data as the electric field is varied for various normalized electron –neutral collisions frequencies. (a) 0.035, (b) 0.039, (c) 0.044, and (d) 0.048.	32
31. Variation in real frequency as a function of electron-neutral collision frequency as determined from the theory for four different normalized $\mathbf{E} \times \mathbf{B}$ drift velocities for experimental parameters.	33
32. Experimental setup, in which microwaves were launched into a) a uniform plasma slab or b, c) a patterned plasma slab.	34
33. Typical profile of the plasma slab in the x-direction.	34
34. Representative density profiles of the plasma in the y-direction, with the patterned plasma slab.	35
35. Microwave transmission through a uniform plasma slab at frequencies of 2.0, 2.5, and 3.0 GHz.	35
36. Microwave transmission through a density minimum in a patterned plasma slab at frequencies of 2.0, 2.4, and 2.8 GHz. The dashed line is the transmission through vacuum.	36
37. Microwave transmission through a density maximum in a patterned plasma slab at frequencies of 2.0, 2.4, and 2.8 GHz. The dashed line is the transmission through vacuum	37
38. Transmission through a minimum in the plasma density for various conditions	37

39. Transmission through a maximum in the plasma density for various conditions.....	38
40. Total transmission through a patterned plasma slab as a function of density for different frequencies.....	38
41. Transmission through a minimum in the plasma for two different magnetic field configurations at frequencies of 2.0 and 2.8 GHz.....	39
42. Results from numerical integration for normal incidence on a plasma slab matching experimental conditions for three frequencies. 2.0, 2.5, and 3.0 GHz.....	40
43. Density (a) and Potential (b) profile plots in the radial direction for a vortex with b value of 0.1439.....	48
44. Potential profile for b of 0.3278.....	49
45. Potential profile for b of 5.6939. As can be seen, as b increases, the profile for $r < Ro$ is dominated by the linear component. For large b, H is nearly equal to D. As such, high b values are not fitting with the desired solution for the vortex quantities.....	49
46. Two dimensional maps of the potential for b values of 0.1439 (left) and 0.6663 (right).	49
47. Fourier spectrum of the vortex density. The wave number, marked above, of the incoming wave with the frequency 1 GHz is $ \mathbf{k}_0 \sim 0.133 \times 10^{-3} \text{ cm}^{-1}$	52
48. Calculated normalized cross section for a vortex with background density of 1.238 * 1010 cm – 3, radius of 7.02 cm, velocity of 280.2 cm/s, and magnetic field of 715 G.	52
49. Expected differential cross section of a 1 Ghz wave from the analytic results in the case where the background plasma frequency is 0.998 GHz.....	53
50. Diagram of LSP simulation. An electromagnetic plane wave is generated at the edge of the simulation (bottom) and propagates until it makes contact with the plasma. The wave travels through the plasma (orange), interacting with the vortex (red and blue) and produces scattered waves (blue arcs).	54
51. Density profile of vortex portion of simulation. The scattering cross section calculation and this density profile were generated using the same physical parameters.....	55
52. Normalized angular distribution of scattered wave output from LSP simulation of a 1 Ghz electromagnetic wave hitting a flute vortex. The physical parameters of these simulations were the same as those used for Figure 49.	55
53. Example of ionospheric flute vortex density perturbation	60
54. Iteratively placed flute vortex field having high separation tolerance	60
55. Iteratively placed flute vortex field having low percentage radius separation tolerance.	60
56. a) Generated 2D density map, b) simulation parameters, c) 3D line plots of ray tracing predominately in the y-z plane with slices of the density map superimposed, d) 3D line plot of the same data rotated so that it is approximately isometric.	61
57. Scatter geometry for Fokker-Planck approximation	62
58. Fokker-Planck comparison; future work.....	63
59. Perturbed Density (left) and the potential (right) of a Flute vortex structure using plasma parameters shown in the table above.....	65
60. Total density profile imbedded in the ambient ionospheric plasma.....	65
61. Theoretical (left) and numerically calculated (right) differential cross section due to the Flute vortex structure shown in Figure 2. Note that the y-axis values are multiplied by 10^{-6} in both plots.	66
62. Flute vortex structures used to calculate the differential cross section shown in Figure 6.5. All plasma parameters are identical to Figure 60 as is the size of the simulation domain, cell size and time step.	66
63. (Left) Differential cross section due to the Flute structure shown the left panel of Figure 62. (Right) Differential cross section due to the Flute structure shown in the right panel of Figure 62..	67

64. Differential cross section due to Flute vortex structure with $\delta n = 15\%$	67
65. Initial density profile input into LSP. The density profile is calculated in a numerical program called FLUTE.....	68
66. Differential cross section due to the numerically calculated vortex structure shown in Figure 63.	68

List of Tables

Figure		Page
1.	The values of parameters for typical ionosphere conditions.....	13
2.	Flute vortex input parameters for density perturbation shown in figure below.	59
3.	Ionospheric plasma parameters used for generating Flute vortex structure shown in the figure below	64

1.0 Executive Summary

In Sections 3 theoretical analysis and numerical results on the Lower Hybrid excitation by velocity shear are presented. The Electron-Ion Hybrid instability, a transverse velocity shear-driven instability with frequency near the lower hybrid frequency, has been observed theoretically and experimentally. It was shown previously that the scale length of the gradient in the velocity must be much smaller than the ion gyroradius and larger than the electron gyroradius in order to generate the short wavelength electron-ion hybrid mode. In this report, the original theory for the electron-ion hybrid instability has been extended to include finite gyroradius effects and electron-neutral collisions with the intention of applying this theory to the plasma region surrounding hypersonic vehicles. In this plasma layer, these sorts of transverse sheared flows can exist in a collisional plasma. While this dense layer of plasma can itself impede communications, the density structures created by the lower hybrid turbulence can also be a source of scattering for these electromagnetic signals.

In Sections 4, 5 and 6 simulation results on scattering of high frequency electromagnetic waves by vortex density structures generated on the nonlinear stage of interchange instability are presented. The interchange instability plays important role in understanding of physical processes in the earth ionosphere and magnetosphere. In particular it is considered as the driving mechanism for the equatorial spread F (ESF) events. In order to analyze interchange instability we employed a two-fluid non-ideal MHD model with inclusion of kinetic effects. This is a step forward in comparison with previously developed models. This approach allows us to resolve spatial scales of turbulent plasma density irregularities comparable with the ion Larmor radius – the spatial scale in the ionospheric F layer of the order of the wavelength of the OTH radar signals. This is the reason why it is important to develop a model which can adequately describe short scale plasma density irregularities. We formulated and derived system of nonlinear two fluid hydrodynamic equations for description of interchange turbulence with included kinetic effects in a high-beta and low beta plasmas and analyzed linear stage of interchange instability with plasma parameters relevant to the equatorial Spread F in the ionosphere. Next, we obtained analytical solutions to the nonlinear equations for density irregularities in the form of double vortex structures. Using these results model of scattering of high frequency electromagnetic waves on vortex density structures was developed and differential and total scattering cross sections were calculated. These results were compared with the results for the scattering cross section obtained in fully kinetic LSP PIC simulations of EM wave scattering on a single density vortex. Analytical and LSP simulation results revealed very good agreement.

2.0 Introduction

The presence of plasma turbulence can strongly influence the propagation properties of electromagnetic signals used for surveillance and communication. In particular, we are interested in the generation of low frequency plasma turbulence in the form of coherent vortex structures coexisting with short scale density irregularities and of lower hybrid turbulence. Lower-hybrid type density irregularities are excited by plasma flows with velocity shear, whereas interchange or flute type oscillations in magnetized plasma are associated with Rayleigh-Taylor type instabilities. These types of density irregularities play important roles in refraction and scattering of high frequency electromagnetic signals propagating in the Earth's ionosphere, inside the plasma sheath of reentry and hypersonic vehicles, and in many other applications. We will discuss the generation of low frequency density irregularities due to the presence of plasma flows with velocity shear and the interchange instability.

The scattering of high-frequency (HF) electromagnetic (EM) waves is a fundamental phenomenon in plasma physics. In a stable plasma EM scattering occurs due to the thermal electron density fluctuations and it is known as "Thomson scattering" [1]. Due to the nonlinear interaction of waves in a plasma, scattering can also arise from single waves excited in the plasma and is explained as a three-wave nonlinear interaction [2]. Scattering can also take place due to the interaction of HF waves with electrostatic solitons [3] or from charged dust particles [4]. We will analyze the formation of plasma density irregularities due to the development of lower hybrid and interchange instabilities. These types of density irregularities play an important role in the analysis of high frequency EM scattering and refraction in the ionospheric plasma. The reason for this is that the spatial scales of these plasma waves are comparable or smaller than the typical wavelengths of EM signals used for surveillance, communication, and OTH radar applications.

In the terrestrial high-latitude (auroral) magnetosphere and ionosphere, whistler-lower-hybrid fluctuations in their electromagnetic or electrostatic limits are usually found in association with energetic electron beams along the geomagnetic field and/or anisotropic electron distributions. In particular, the energetic electron acceleration within the terrestrial auroral region results in the emission of short-wavelength, primarily electrostatic waves near the resonance cone of the whistler-lower-hybrid branch [5]. Another source of enhanced lower hybrid waves in the auroral ionosphere is related to strongly sheared plasma flows driven by structured electric fields in the vicinity of small scale auroral arcs [6].

At subauroral latitudes, lower hybrid/fast magnetosonic waves accompany such well-known space weather phenomena as subauroral ion drifts (SAID) and subauroral polarization streams (SAPS) [7, 8]. Figure 1 presents an overview of one of such events that occurred on 18 March 2002 when three independent spacecraft (Cluster, DMSP, and Polar) crossed the SAID channel virtually at the same time and within the same magnetic flux tube. It is seen that the wave activity is abruptly enhanced inside the SAID channel, just inside the plasmapause boundary (the plasmapause).

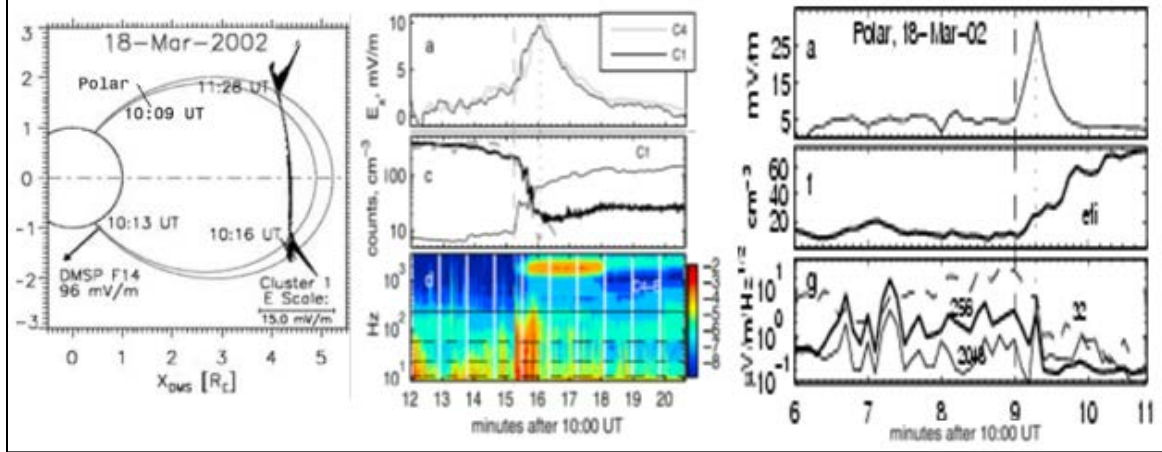


Figure 1: (left panel) World-line plots of the Cluster, DMSP, Polar satellites during the 18-March-2002 substorm event. The SAID channels from Cluster 1 (C1) are superimposed. Shown in the middle are (top) the C1/C4 outward electric field E_x in the inertial frame, (mid) C1/EDI 1-keV electron counts (thick line) and the cold plasma density n_0 (thin), and (bottom) C4/STAFF frequency-time spectrograms for the electric spectral power in $(\text{mV}/\text{m})^2/\text{Hz}$ (in log scale). Horizontal lines indicate the lower hybrid resonance (solid) and the 10th, 4th, and 2nd harmonics of the H^+ -ion gyrofrequency (dashed), derived from the observed magnetic field. Shown on the right are the features of the northern SAID channel from Polar: (top) the outward electric field, (mid) the plasma density, and (bottom) spectral amplitudes of electric fields at 32 (dashed line), 256 (thick), and 2048 (thin) Hz

The remainder of this report is organized as follows. In Section 3, excitation of the lower hybrid instability by flows with velocity shear in the presence of electron-neutral collisions is analyzed. Linearized equations for the lower hybrid eigenmodes inside a plasma slab with velocity shear will be derived and solved numerically. Numerical solution is based on the implementation of a shooting code. In Section 3, nonlinear equations describing the interaction of the lower hybrid waves inside a plasma flow with velocity shear and low frequency ion acoustic oscillations will be derived, and a dispersion equation for the modified decay instability will be presented. In Section 4, the results of the laboratory experiments in the NRL Space Chamber on excitation of lower hybrid turbulence by $\mathbf{E} \times \mathbf{B}$ flows with velocity shear will be presented. In Section 5, linear and nonlinear stages of interchange instability with the ionospheric plasma parameters corresponding to the equatorial F-layer will be discussed. In the description of the interchange instability we retain finite ion Larmor radius effects. Inclusion of spatial scales comparable with the ion Larmor radius is important for the analysis of radar generated high-frequency EM waves interacting with density irregularities associated with the equatorial spread F in the ionosphere.

Over the past twenty years, there have been numerous studies into the destabilizing effects of inhomogeneous electric fields transverse to the ambient magnetic field. It has been demonstrated that the electric field gradient scale length LE is the key length scale that determines the nature of the instability [14]. If LE is on the order of the ion gyroradius ρ_i , then the instability will be driven by the dynamics of the ions and could be an electrostatic ion cyclotron wave or an Alfvén wave depending on the plasma β [15]. However, if $\rho_e < LE < \rho_i$, then the ions do not experience the $\mathbf{E} \times \mathbf{B}$ drift and the instability will be driven by the dynamics of the electrons. These waves are

primarily electrostatic lower hybrid waves in the VLF range. All of these velocity shear-driven instabilities are primarily azimuthally propagating in the direction of the $\mathbf{E} \times \mathbf{B}$ drift.

3.0 Excitation of Lower Hybrid Waves by a Flow with Velocity Shear

In this Section we will analyze instability of a plasma flow with a transverse velocity shear scale length much smaller than the ion gyroradius but larger than the electron gyroradius. As shown in [11] [12], under these conditions electrostatic oscillations with the frequencies above the lower hybrid frequency

$$\omega_{LH}^2 = \frac{\omega_{pi}^2}{1 + \frac{\omega_{pe}^2}{\omega_{ce}^2}} \quad (1)$$

can be excited. In equation (1) ω_{pe} and ω_{pi} are the corresponding electron and ion plasma frequencies and ω_{ce} is the electron cyclotron frequency. Below in the hydrodynamic approximation we will derive linearized equation for excitation of oscillations in the frequency range just above the lower hybrid frequency ω_{LH} . In this equation we will include wave dispersion due to the thermal effects and electron neutral collision frequency. We will also include into our analysis not only the waves propagating strictly perpendicular to the external magnetic field but also waves propagating nearly perpendicular to the magnetic field. These waves should satisfy the condition $\frac{k_z^2}{k_\perp^2} \ll \frac{m}{M}$ (m and M are electron and ion masses respectively), k_\perp - is the wave vector perpendicular to an external magnetic field and k_z - is the wave vector of excited oscillations along the magnetic field. Electrons in the lower hybrid oscillations are magnetized, but ions are unmagnetized. An external electric field varies along the x -direction $E_{0x}(x)$ and creates electron flow with velocity shear directed along the y -direction $V_{0y}(x)$ (see Figure 2). The width of the layer with electric field inhomogeneity is smaller than the ion Larmor radius. In such a system, we have electron flow with velocity shear moving in y -direction, whereas ions, being unmagnetized, do not experience **ExB** drift and are at rest in the laboratory coordinate system. We will use linearized electron momentum equation which also contains electron-neutral collision term. For the electron motion across the magnetic field we can write:

$$\frac{\partial \mathbf{v}_{\perp 1}}{\partial t} + (\mathbf{v}_{\perp 0} \cdot \nabla) \mathbf{v}_{\perp 1} + (\mathbf{v}_{\perp 1} \cdot \nabla) \mathbf{v}_{\perp 0} + \frac{V_{Te}^2}{N_{0e}} \nabla_\perp n_{e1} = \frac{e}{m_e} \frac{\partial \Phi}{\partial \mathbf{r}_\perp} - \frac{e}{m_e c} [\mathbf{v}_{\perp 1} \times B_{0z} \mathbf{e}_z] - v_{en} \mathbf{v}_{\perp 1} \quad (2)$$

For the electron motion along the magnetic field (z -axis) we have:

$$\frac{\partial \mathbf{v}_{1z}}{\partial t} + v_{0y} \frac{\partial \mathbf{v}_z}{\partial y} + \frac{V_{Te}^2}{N_{0e}} \frac{\partial n_{e1}}{\partial z} = \frac{e}{m_e} \frac{\partial \Phi}{\partial z} - v_{en} \mathbf{v}_{1z} \quad (3)$$

The linearized ion momentum equation for unmagnetized ions has the form:

$$\frac{\partial \mathbf{u}_1}{\partial t} = -\frac{e}{m_i} \frac{\partial \Phi}{\partial \mathbf{r}} \quad (4)$$

We will use also continuity equations for electrons:

$$\frac{\partial N_e}{\partial t} + \operatorname{div}(N_e \mathbf{v}_e) = 0 \quad (5)$$

and ions:

$$\frac{\partial n_{i1}}{\partial t} + N_{0i} \operatorname{div} \mathbf{u}_1 = 0 \quad (6)$$

Final equation is the Poisson equation for the electrostatic potential of a lower hybrid wave:

$$\Delta \Phi = 4\pi e(n_{e1} - n_{i1}) \quad (7)$$

Using the system of equations we can arrive to the following linearized equation which describes LH wave excitation in the non-local approximation:

$$\begin{aligned} & \frac{\partial^2}{\partial t^2} \left[\left(\frac{\omega_{pi}^2}{\omega_\alpha^2} (1 + R^2 \Delta) \hat{L}_z^2 \Delta \Phi + \omega_{pe}^2 \frac{\partial^2 \Phi}{\partial z^2} + \nu_{en} \left((1 + 2 \frac{\omega_{pe}^2}{\omega_{ce}^2}) \hat{L}_z + \nu_{en} \frac{\omega_{pe}^2}{\omega_{ce}^2} \right) \Delta \Phi \right. \right. \\ & \left. \left. - \frac{\omega_{pe}^2}{\omega_{ce}^2} (\hat{L}_z + \nu_{en}) \frac{\partial^2 V_{0y}}{\partial x^2} \frac{\partial \Phi}{\partial y} \right] + \omega_{pi}^2 [\hat{L}_z^2 + \nu_{en} \hat{L}_z] \Delta \Phi = 0 \right] \end{aligned} \quad (8)$$

In equation (7) ν_{en} is an electron-neutral collision frequency, $V_{0y}(x)$ is the flow velocity and operator \hat{L}_z is defined as: $\hat{L}_z = \frac{\partial}{\partial t} + V_{0y}(x) \frac{\partial}{\partial y}$.

We are interested in the solution of the equation (7) which represents waves propagating along the y and z directions inside a plasma slab and the solution in the form of the eigenfunction in the x-direction of the flow inhomogeneity:

$$\Phi \sim \Psi(x) e^{(-i\omega t + k_y y + k_z z)} \quad (9)$$

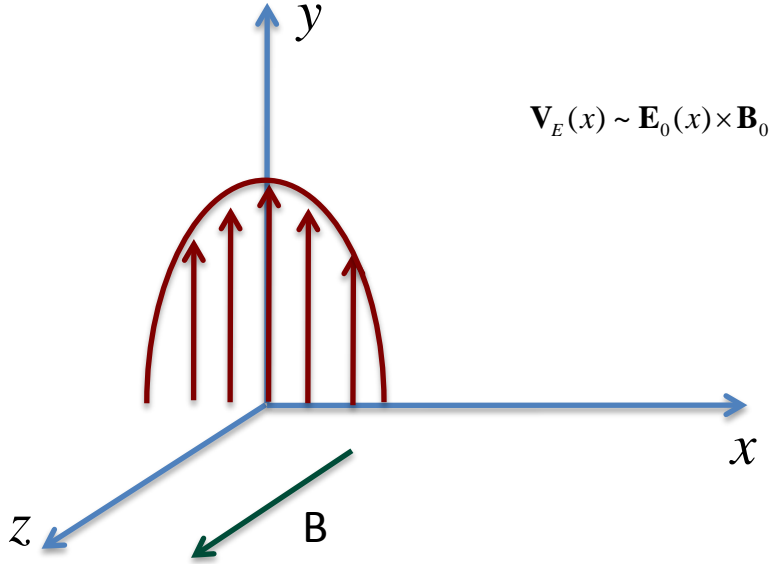


Figure 2: In this figure a nonuniform electric field $E_{0x}(x)$ and an external magnetic field B_{0z} create a nonuniform electron flow with velocity shear along the y -direction

We set $x = 0$ at the conducting surface of the vehicle and require

$$\phi(x=0) = 0. \quad (10)$$

In the free space beyond the sheath edge at $x = L$, the potential $\phi(x) = \phi(L) \exp[-k(x-L)]$ so that

$$\left[\frac{d\phi}{dx} + k\phi \right]_{x=L} = 0. \quad (11)$$

Equation (8) together with boundary conditions (10) and (11) constitute the eigenvalue problem to be solved numerically for the complex eigenfrequency ω using a standard shooting method [12].

Using equation (8) for conditions used in Ganguli *et al.* and neglecting thermal dispersion of lower hybrid waves ($R = 0$), electron-neutral collisions ($\nu_{en} = 0$) and restricting analysis to the waves with $k_z = 0$, the shooting code recovers the previously published

solutions $\omega = (1.89 + i1.94)\omega_{LH}$ (see [8]). From this point using equation (8), the shooting code was used to investigate the effect of finite electron-neutral collisions on the mode. Figure 3 shows the real frequency (solid black line) and growth rate (dashed red line) normalized to the lower hybrid frequency as a function of electron-neutral collision frequency normalized to the electron cyclotron frequency for plasma conditions similar to those from published experimental observations of this instability [13]: $\omega_{pe}/\Omega_e = 8.0$, $v_E/\Omega_e L_E = 13.6$, $k_y L_E = 0.5$, $k_z L_E = 0$, and argon ions. The following electric field profile was used in the code:

$$E_{0x}(x) = E_0 \sec h^2\left(\frac{x}{L_E}\right) \quad (12)$$

where L_E is the velocity shear scale length in the electron flow and the shear flow velocity along the y-direction is defined as:

$$\mathbf{V}_{0y}(x)\mathbf{e}_y = c \frac{\mathbf{E}_0(x) \times \mathbf{B}_0}{B_0^2} \quad (13)$$

where c – is the speed of light.

Results of numerical solution of equation (8) with inclusion of electron-neutral collisions, but with omission of thermal dispersion and with $k_z = 0$ are presented by Figure 3. It can be seen that the presence of weak collisions has a strong effect on both the growth rate and real frequency, though the mode is not completely stabilized. We stop at $\nu_{en} \sim 0.1\omega_{ce}$ to remain in the regime where the drift approximation is valid. However, it is expected that $\nu_{en} \sim \Omega_e$ is needed before collisions could totally suppress the excitation of the mode.

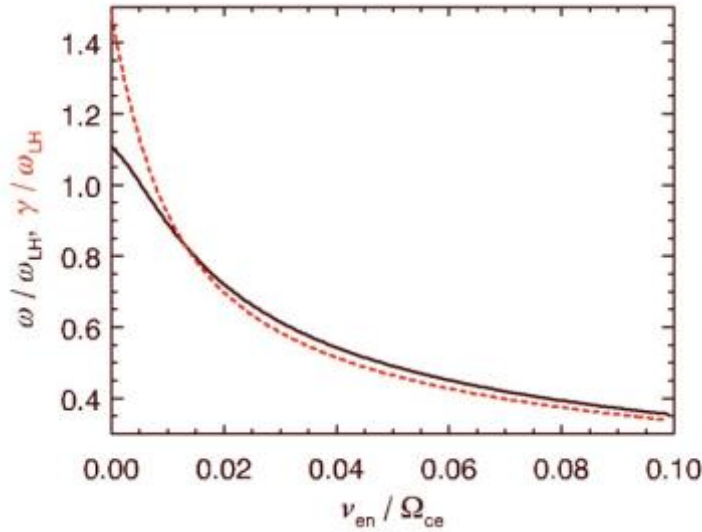


Figure 3: Normalized real frequency (solid black line) and growth rate (dashed red line) dependence on normalized collision frequency.

To obtain solution for the frequency and the growth rate of excited modes in the local approximation, we again will use equation (8) neglecting the thermal dispersion of lower hybrid waves($R=0$), electron-neutral collisions ($\nu_{en} = 0$) and restricting analysis to the waves with $k_z = 0$. This will allow us to examine the qualitative behavior of this instability without employing the full numerical solution. To arrive at the local approximation for the lower hybrid modes, we start from:

$$\frac{d^2\phi}{dx^2} - \bar{\kappa}^2 \phi = 0, \quad (14)$$

where

$$\bar{\kappa}^2 = \bar{k}_y^2 - \frac{\delta^2}{\delta^2 + 1} \frac{\bar{\omega}^2}{\bar{\omega}^2 - 1} \frac{\bar{k}_y \bar{v}_E''}{\bar{\omega} - \bar{k}_y \bar{v}_E}, \quad (15)$$

and $\delta = \omega_{pe}/\Omega_e$, $\bar{k}_y = k_y L_E$, $\bar{\omega} = \omega/\omega_{LH}$, and $\bar{v}_E = v_E/\omega_{LH} L_E$. We obtain the local dispersion relation by taking $\bar{\kappa}^2 = 0$ and using the values for \bar{v}_E and \bar{v}_E'' at $x = 0$ as in Romero *et al.* [9]. This results in a cubic equation for ω :

$$\bar{\omega}^3 + \bar{k}_y \bar{v}_{E0} \left(\frac{2}{\bar{k}_y^2} \frac{\delta^2}{\delta^2 - 1} - 1 \right) \bar{\omega}^2 - \bar{\omega} + \bar{k}_y \bar{v}_{E0} = 0, \quad (16)$$

Figure 4 shows the local and non-local solutions for the following parameters: $\delta = 8.0$, $\bar{v}_E = 1.1$, $k_y L_E = 0.5$, $k_z L_E = 0$, and argon ions. The local solution does a good job of approximating the general behavior of the non-local solutions. More importantly, the solutions below represent a good operating regime for studying the non-linear behavior of this mode. The maximum growth rate occurs for a real frequency just above the lower hybrid frequency, and the mode only exists for a small band of perpendicular wave numbers.

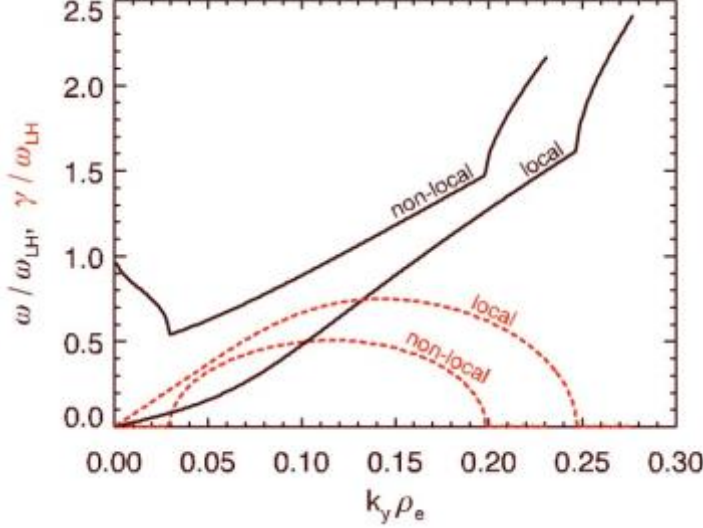


Figure 4: Normalized real frequency (solid black line) and growth rate (dashed red line) dependence on normalized perpendicular wave number comparing local and non-local solutions.

3.1 Numerical Modeling of Parametric Interaction of Finite Amplitude Very Low Frequency (VLF) Waves

Modulation instability of electromagnetic waves is a dominant feature of ionospheric plasma turbulence. Nonlinear stage of modulation instability leads to Langmuir collapse [16]. The latter causes wave localization within which the plasma is expelled by wave pressure. This phenomenon is also expected for the waves in a magnetized plasma with frequencies close to the frequency of the lower-hybrid resonance $\omega_\alpha = \left(\frac{\omega_{pi}^2}{1 + \frac{\omega_{pe}^2}{\omega_{ce}^2}} \right)^{1/2}$ [17,18], where $\omega_{pe} = (4\pi e^2 n_0/m)^{1/2}$ is electron

$$\omega_{pe} = (4\pi e^2 n_0/m)^{1/2}$$

Langmuir frequency, $\omega_{pi} = \omega_{pe}(m/M)^{1/2}$ is ion plasma frequency, $\omega_{ce} = eB_0/(mc)$ is the electron cyclotron frequency, m and M is the electron and ion masses, B_0 is the external magnetic field, n_0 is the density of electrons and e is the electron's electric charge. In plasma with magnetized electrons and unmagnetized ions, these oscillations obey the following dispersion relation:

$$\omega = \omega_\alpha \left(1 + \frac{1}{2} k^2 R^2 + \frac{M}{2m} \frac{k^2}{k_\parallel^2} - \frac{\omega_{pe}^2}{2k^2 c^2} \frac{\omega_{pe}^2}{\omega_{pe}^2 + \omega_{ce}^2} \right), \quad (17)$$

where the typical space scale of the dispersion length $R = \left(\frac{3T_i}{\omega_\alpha^2 M} + \frac{2T_e}{\omega_{ce}^2 m} \frac{\omega_{pe}^2}{\omega_{pe}^2 + \omega_{ce}^2} \right)^{1/2}$, k is the wave number and k_\parallel is the wave number in parallel to magnetic field direction. These waves have wave numbers almost normal to the magnetic field ($k_\perp \gg k_\parallel$, where k_\perp is the wave number in a normal to magnetic field direction). In the first phase of this project we studied the branch of oscillations of cold plasma transverse to the magnetic field ($k_\perp = 0$), i.e., two-dimensional (2D) case. Figure 5 shows the dispersion relation curve. We consider the waves with wave number close to

$k^* \approx (\alpha \omega_{pe}^2 / (c^2 R^2))$, where $\alpha = 1 / (1 + \omega_{ce}^2 / \omega_{pe}^2)$. There are two type of waves: electromagnetic (magnetosonic) for $k < k^*$ and electrostatic (lower-hybrid) waves for $k > k^*$. It has been shown that the frequency dispersion permits the onset of the modulation instability leading finally to collapse in both cases, i.e., magnetosonic and lower-hybrid waves [19]. The goal of this project is computational investigation of modulation instability and collapse of waves in the vicinity of the lower-hybrid resonance.

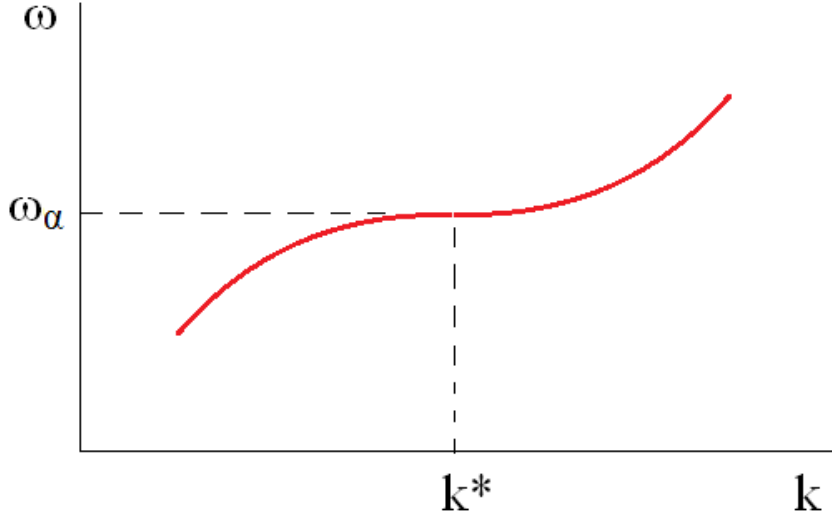


Figure 5: Dispersion relation for electromagnetic (magnetosonic) and electrostatic (lower-hybrid) waves; for $k < k^*$, the waves are magnetostatic and for $k > k^*$, lower-hybrid

The system of hydrodynamic equations of two component plasma in a magnetic field in approximation of magnetized electrons and unmagnetized ions in its general form includes the equation for the electric field and the equation for the electron density in ion-acoustic wave is as follows [14]:

$$\begin{aligned} & \frac{\partial^2}{\partial t^2} \left[\left(\frac{\omega_{pi}^2}{\omega_\alpha^2} + R^2 \Delta \right) \hat{L}_z^2 \Delta \Phi + \omega_{pe}^2 \left(1 - \frac{\omega_{ce}^2}{\omega_{pe}^2} \rho_e^2 \Delta \right) \frac{\partial^2 \Phi}{\partial z^2} + \frac{\omega_\alpha^2 \omega_{pe}^6}{c^2 \omega_{ce}^2} \Phi + V_{en} \left(1 + 2 \frac{\omega_{pe}^2}{\omega_{ce}^2} - 2 \rho_e^2 \Delta \right) \hat{L}_z \Delta \Phi + \frac{\omega_{pe}^2}{\omega_{ce}^2} (\hat{L}_z^2 + V_{en}^2) \Delta \Phi \right. \\ & \quad \left. - (V_{en}^2 \rho_e^2 \Delta) \Delta \Phi - \frac{\omega_{pe}^2}{\omega_{ce}^2} (\hat{L}_z + V_{en}) \frac{\partial^2 V_{0y}(x)}{\partial x^2} \frac{\partial \Phi}{\partial y} + \rho_e^2 (\hat{L}_z + V_{en}) \frac{\partial^2 V_{0y}(x)}{\partial x^2} \frac{\partial}{\partial y} \Delta \Phi \right] + \\ & \quad + \omega_{pi}^2 \left[(1 - \rho_e^2 \Delta) \hat{L}_z^2 \Delta \Phi - \omega_{ce}^2 \rho_e^2 \frac{\partial^2}{\partial z^2} \Delta \Phi + V_{en} \left(1 - 2 \rho_e^2 \Delta \right) \hat{L}_z \Delta \Phi - \rho_e^2 \hat{L}_z^2 \Delta^2 \Phi + \rho_e^2 (\hat{L}_z + V_{en}) \frac{\partial^2 V_{0y}(x)}{\partial x^2} \frac{\partial}{\partial y} \Delta \Phi \right] = \\ & = \frac{\omega_{pe}^2}{\omega_{ce}^2} \frac{\partial^2}{\partial t^2} (\hat{L}_z + V_{en}) \left[\left\{ \frac{\delta n}{n_0}, \Phi \right\} \right], \end{aligned} \tag{18}$$

$$\frac{\partial^2 \delta n}{\partial t^2} - (V_{Ti}^2 + V_{Te}^2) \Delta \delta n = - \frac{i}{4\pi M} \frac{\omega_{pe}^2}{\omega_{ce} \omega_\alpha} \Delta \{ \Phi, \Phi^* \} \tag{19}$$

where $\hat{L}_z = \frac{\partial}{\partial t} + V_{0y}(x) \frac{\partial}{\partial y}$, $\hat{L}_{zv} = \frac{\partial}{\partial t} + V_{0y}(x) \frac{\partial}{\partial y} + v_{en}$, $\hat{L}_{zvT} = \hat{L}_{zv} \hat{L}_z - V_{Te}^2 \frac{\partial^2}{\partial z^2}$ and $\hat{L}_{zz} = \hat{L}_{zv} \hat{L}_z$, Φ is the electric potential, n is the disturbed density of electrons ($n \ll n_0$), $\omega_{ci} = eB_0/(Mc)$ is the ion cyclotron frequency, $\rho_e = mV_{Te}/(eB_0)$ is the electron gyroradius, v_{en} is the electron-neutral collision coefficient, V_{0y} is the drift velocity of electrons normal to magnetic field, V_{Te} and V_{Ti} are the thermal velocity of electrons and ions and c is the speed of light; Δ is 3D Laplace operator, t is time and x , y and z are the spatial coordinates.

We need to simplify and normalize these equations. We omit all the terms with ρ_e^2 with the exception of the second term at the left hand side of equation (3.17) since they are small. We also consider v_{en} small but finite and we can drop it in the nonlinear term. Now instead of (18) in 2D case we get:

$$\begin{aligned} \frac{\partial^2}{\partial t^2} & \left[\left(\frac{\omega_{pi}^2}{\omega_\alpha^2} + R^2 \Delta \right) \hat{L}_z^2 \Delta \Phi + v_{en} \left(1 + 2 \frac{\omega_{pe}^2}{\omega_{ce}^2} \right) \hat{L}_z \Delta \Phi + \frac{\omega_{pe}^2}{\omega_{ce}^2} (\hat{L}_z^2 + v_{en}^2) \Delta \Phi + \frac{\omega_\alpha^2 \omega_{pe}^4}{c^2 \omega_{ce}^2} \Phi - \frac{\omega_{pe}^2}{\omega_{ce}^2} (\hat{L}_z + v_{en}) \frac{\partial^2 V_{0y}(x)}{\partial x^2} \frac{\partial \Phi}{\partial y} \right] + \\ & + \omega_{pi}^2 \left[(1 + R^2 \Delta) \hat{L}_z^2 \Delta \Phi + v_{en} \hat{L}_z \Delta \Phi \right] = \frac{\omega_{pe}^2}{\omega_{ce}^2} \frac{\partial^2}{\partial t^2} (\hat{L}_z + v_{en}) \left\{ \left\{ \frac{\delta n_e}{n_{0e}}, \Phi \right\} \right\}, \end{aligned} \quad (20)$$

where Δ is 2D Laplace operator. Equation (20) without terms which include electron-neutral collisions has the following form:

$$\frac{\partial^2}{\partial t^2} \left[\frac{\omega_{pi}^2}{\omega_\alpha^2} (1 + R^2 \Delta) \hat{L}_z^2 \Delta \Phi + \frac{\omega_\alpha^2 \omega_{pe}^4}{c^2 \omega_{ce}^2} \Phi - \frac{\omega_{pe}^2}{\omega_{ce}^2} \frac{\partial^2 V_{0y}}{\partial x^2} \hat{L}_z \frac{\partial \Phi}{\partial y} \right] + \omega_{pi}^2 \hat{L}_z^2 \Delta \Phi = \frac{\omega_{pe}^2}{\omega_{ce}^2} \frac{\partial^2}{\partial t^2} \hat{L}_z \left\{ \frac{\delta n}{n_0}, \Phi \right\} \quad (21)$$

Equation (21) could be further simplified when frequency is far from resonance which allows separation of the fast and slow times [19]:

$$[2i \frac{1}{\omega_\alpha} \frac{\partial}{\partial \tau} + R^2 \Delta] \hat{L} \Delta \Phi - \frac{\omega_\alpha^2}{\omega_{ce}^2} \frac{\omega_{pe}^2}{\omega_{pi}^2} \frac{\partial^2 V_{0y}}{\partial x^2} \frac{\partial \Phi}{\partial y} + \frac{\omega_\alpha^2 \omega_{pe}^4}{c^2 \omega_{ce}^2 \omega_{pi}^2} \Phi = \omega_{ce} \frac{\omega_\alpha^2}{\omega_{ce}^2} \frac{\omega_{pe}^2}{\omega_{pi}^2} \left\{ \frac{\delta n}{n_0}, \Phi \right\} \quad (22)$$

$$\hat{L} = -i\omega_\alpha + V_{0y}(x) \frac{\partial}{\partial y}.$$

where τ is new “slow” time and

Let us make equations dimensionless (all variables with \sim (tilde) on the top are dimensional, without \sim (tilde) variables are dimensionless, for example, \tilde{t} is dimensional, but t is dimensionless):

$$[2i \frac{\partial}{\partial t} + \Delta] (1 + i \frac{\tilde{V}_{0y}(x)}{\tilde{V}_s K^2} \frac{\partial}{\partial y}) \Delta \Phi - i \frac{\omega_\alpha^2}{\omega_{ce}^2} \frac{\omega_{pe}^2}{\omega_{pi}^2} \frac{\partial^2 (\tilde{V}_{0y}/\tilde{V}_s)}{\partial x^2} \frac{\partial \Phi}{\partial y} + i \frac{\omega_\alpha^2 \omega_{pe}^4}{c^2 \omega_{ce}^2 \omega_{pi}^2} \Phi = i \left\{ \frac{\delta n}{n_0}, \Phi \right\} \quad (23)$$

$$\frac{\partial^2}{\partial t^2} \delta n - \left(\frac{T_i}{T_e} + 1\right) \Delta \delta n = -i \frac{1}{s} \Delta \{\Phi, \Phi^*\} \quad (24)$$

$$t = \omega_\alpha \tilde{t} \frac{V_{T_i}^2}{\omega_\alpha^2 R^2} \frac{1}{R^2} = \omega_\alpha \tilde{t} \frac{1}{K^2}, \quad \tilde{t} = \frac{K^2}{\omega_\alpha} t, \quad K^2 = \frac{\omega_\alpha^2}{V_{T_i}^2} R^2, \quad s = \sqrt{1 + \frac{\omega_{ce}^2}{\omega_{pe}^2}},$$

where

$$x = \frac{\tilde{x}}{RK}, \quad \tilde{\Phi} = \frac{2T_e K}{es} \sqrt{\frac{m_e}{M_i}} \Phi, \quad \delta n = \frac{\delta \tilde{n}}{\tilde{n}_0} \frac{m_i}{m_e} \frac{\omega_\alpha}{\omega_{ce}} K^2, \quad \frac{\delta \tilde{n}}{\tilde{n}_0} = \frac{m_e}{M_i} \frac{\omega_{ce}}{\omega_\alpha} \frac{1}{K^2} \delta n, \quad \tilde{\Delta} = \frac{1}{K^2 R^2} \Delta$$

Let us estimate the typical parameter for the ionosphere plasma. Supposing $n_0 = 4 * 10^4 \text{ cm}^{-3}$, $T_e = 3 \cdot 10^3 \text{ K} = 0.2586 \text{ ev} = 0.4143 \cdot 10^{-12} \text{ g} \cdot \frac{\text{cm}^2}{\text{s}^2}$, $T_i = 4 \cdot 10^3 \text{ K} = 0.3448 \text{ ev} = 0.5524 \cdot 10^{-12} \text{ g} \cdot \text{cm/s}^2$, $B_0 = 0.35 \text{ Gs}$ (gauss), $M = 16 \cdot 1.6726 \cdot 10^{-24} \text{ g}$, $m = 9.10938 \cdot 10^{-28} \text{ g}$ we find all necessary parameters (see Table 1).

Table 1: The values of parameters for typical ionosphere conditions

ω_{ce} rad/sec	ω_{ci} rad/sec	ω_{pe} rad/sec	ω_{pi} rad/sec	ω_α rad/sec	s	m	V_{T_i} cm/s	V_s cm/s	K
6.16e6	2.1e2	1.13e7	.6e4	3.16e4	1.139	.3	1.437e5	1.244e5	0.9458

As mentioned earlier, we will consider two wave types: magnetosonic and lower-hybrid waves. For the lower-hybrid waves, the third term of equation (23) was removed. Considering the coefficient in

$$\frac{\omega_\alpha^2}{\omega_{ce}^2} \frac{\omega_{pe}^2}{\omega_{pi}^2} \approx 1$$

the second term of equation (23) and the coefficient in third term of equation (24) $s \approx 1$ we can rewrite system (23-24) in the following form:

$$[2i \frac{\partial}{\partial \tau} + \Delta] (1 + i \frac{\tilde{V}_{0y}(x)}{\tilde{V}_s} \frac{1}{K^2} \frac{\partial}{\partial y}) \Delta \Phi - i \frac{\partial^2 (\tilde{V}_{0y} / \tilde{V}_s)}{\partial x^2} \frac{\partial \Phi}{\partial y} + C \Phi = i \{\delta n, \Phi\}, \quad C = \frac{\omega_\alpha^2 \omega_{pe}^4}{c^2 \omega_{ce}^2}, \quad (25)$$

$$\frac{\partial^2}{\partial t^2} \delta n - \left(\frac{T_i}{T_e} + 1\right) \Delta \delta n = -i \Delta \{\Phi, \Phi^*\} \quad (26)$$

or in the form used for numerical calculations:

$$\frac{\partial}{\partial t} \Delta \varphi_1 = -\frac{V}{2K^2} \frac{\partial}{\partial y} \Delta^2 \varphi_1 - \frac{1}{2} \Delta^2 \varphi_2 + \frac{V''}{2} \frac{\partial}{\partial y} \varphi_1 - C \varphi_1 + \frac{1}{2} [\delta n, \varphi_1],$$

$$\frac{\partial}{\partial t} \Delta \varphi_2 = -\frac{V}{2K^2} \frac{\partial}{\partial y} \Delta^2 \varphi_2 + \frac{1}{2} \Delta^2 \varphi_1 + \frac{V''}{2} \frac{\partial}{\partial y} \varphi_2 - C \varphi_2 + \frac{1}{2} [\delta n, \varphi_2],$$

$$\frac{\partial \delta n}{\partial t} = u, \quad (27)$$

$$\frac{\partial \delta n}{\partial t} = u,$$

$$\frac{\partial u}{\partial t} = \frac{T}{T_e} \Delta \delta n - 2 \frac{T}{T_e} \Delta [\varphi_1, \varphi_2],$$

where $\Phi = \varphi_1 + i\varphi_2$.

If we count electron-neutral collision the first two equations from system (27) have a form as follows:

$$\begin{aligned} \frac{\partial}{\partial t} \Delta \varphi_1 &= -\frac{V}{2K^2} \frac{\partial}{\partial y} \Delta^2 \varphi_1 - \frac{1}{2} \Delta^2 \varphi_2 + \frac{V''}{2} \frac{\partial}{\partial y} \varphi_1 - C \varphi_1 + v \Delta \varphi_2 + \frac{1}{2} [\delta n, \varphi_1], \\ \frac{\partial}{\partial t} \Delta \varphi_2 &= -\frac{V}{2K^2} \frac{\partial}{\partial y} \Delta^2 \varphi_2 + \frac{1}{2} \Delta^2 \varphi_1 + \frac{V''}{2} \frac{\partial}{\partial y} \varphi_2 - C \varphi_2 - v \Delta \varphi_1 + \frac{1}{2} [\delta n, \varphi_2], \end{aligned} \quad (28)$$

$$v = \frac{v_{en}}{\omega_\alpha} \frac{\omega_{ce}^2}{\omega_{pe}^2}$$

where v is the normalized electron-neutral collision coefficient

For the 3D case (Phase II of this project) we will consider only lower-hybrid waves. However in this case we will keep second term in equation (18). The simplified version of system of equations (18) and (19) with negligence of dissipation terms is as follows:

$$[2i \frac{\partial}{\partial \tau} + \Delta] (1 + i \frac{\tilde{V}_{0y}(x)}{\tilde{V}_s}) \frac{1}{K^2} \frac{\partial}{\partial y} \Delta \Phi - i \frac{\partial^2 (\tilde{V}_{0y} / \tilde{V}_s)}{\partial x^2} \frac{\partial \Phi}{\partial y} + C \Phi + \omega_{pe}^2 \frac{\partial^2 \Phi}{\partial z^2} = i \{\delta n, \Phi\}, \quad (29)$$

$$\frac{\partial^2}{\partial t^2} \delta n - (\frac{T_i}{T_e} + 1) \Delta \delta n = -i \Delta \{\Phi, \Phi^*\} \quad (30)$$

System (29 , 30) in the form of numerical calculation are:

$$\begin{aligned} \frac{\partial}{\partial t} \Delta \varphi_1 &= -\frac{V}{2K^2} \frac{\partial}{\partial y} \Delta \varphi_1 - \frac{1}{2} \Delta \varphi_2 + \frac{V''}{2} \frac{\partial}{\partial y} \varphi_1 + C_1 \frac{\partial^2 \varphi_1}{\partial z^2} - C \varphi_1 + \frac{1}{2} [\delta n, \varphi_1], \\ \frac{\partial}{\partial t} \Delta \varphi_2 &= -\frac{V}{2K^2} \frac{\partial}{\partial y} \Delta \varphi_2 + \frac{1}{2} \Delta \varphi_1 + \frac{V''}{2} \frac{\partial}{\partial y} \varphi_2 + C_1 \frac{\partial^2 \varphi_2}{\partial z^2} - C \varphi_2 + \frac{1}{2} [\delta n, \varphi_2], \\ \frac{\partial \delta n}{\partial t} &= u, \end{aligned} \quad (31)$$

$$\frac{\partial \delta n}{\partial t} = u,$$

$$\frac{\partial u}{\partial t} = \frac{T}{T_e} \Delta \delta n - 2 \frac{T}{T_e} \Delta [\varphi_1, \varphi_2],$$

Note that here Δ is 3D Laplace operator. However, since k_z is much larger than k_\perp (indeed $k_z \ll k_\perp (m/M)^{1/2} \approx 171 \cdot k_\perp$), all terms with derivatives in z direction (except of the term $\omega_{pe}^2 \frac{\partial^2 \Phi}{\partial z^2}$) are negligible. Thus we should use Δ as 2D Laplace operator.

The source of instability is velocity shear of electron drift. To make a calculation we will use the velocity profile depicted on Figure 6.

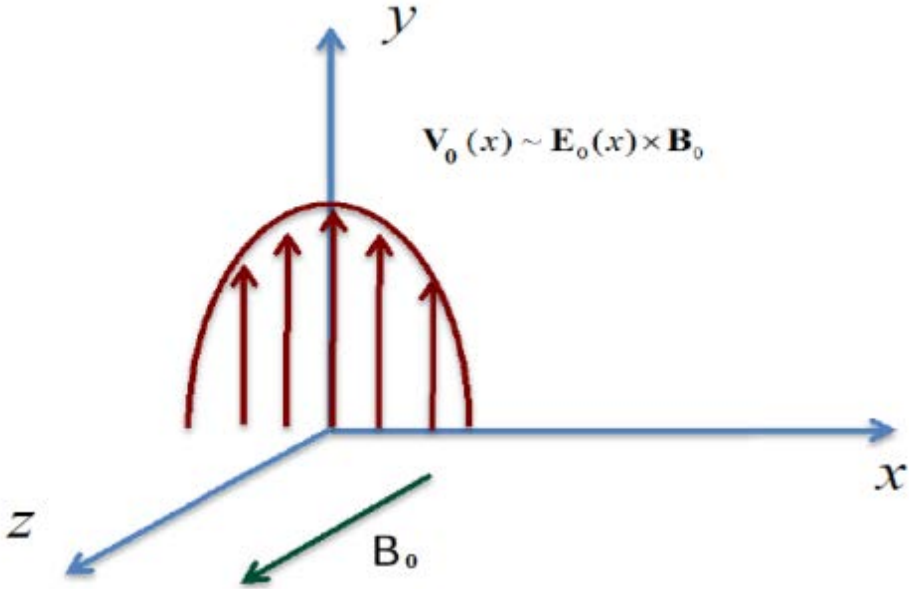


Figure 6: In this figure a nonuniform electric field E_0 and an external magnetic field B_0 create a nonuniform electron flow with velocity shear along the y-direction.

3.2 Analyses of the preliminary results

The “Beavercreek 2” code has been modified for solution of system of equations (3.26) describing parametric interaction of finite amplitude VLF waves in the presence of velocity shear. This work corresponds to the implementation of the first task of the portion of the work.

To test the new code, we solved 2D problem with periodic boundary conditions. We used the grid 256x256. The initial conditions were randomly distributed (very low) electric field and plasma density fluctuations: in dimensionless units, the electric field and fluctuation of plasma density were in the order of 10^{-8} . The source of instability, i.e., the electron velocity shear, was taken as follows: electrons drift in y-direction with velocity function is given by Gaussian distribution with the center in the middle of x-axis ($x=128$) with amplitude $V_0=1.0$. We consider two cases: lower-hybrid waves,

i.e., we did not count the correction term for magnetosonic waves ($C=0$ in equations (26)), and magnetosonic waves ($C>0$ in equations (26)).

3.3 Modulation Instability of Lower-Hybrid waves

Figure 7- 11 show the results of spatial distribution of the electric field as well as their 2D spatial Fourier spectrum for the different moments of time (t) starting from the initial random distribution ($t = 0$) (Figure 11). As one can see, the modulation instability begins to develop at $t = 800$ (Figure 8) along lines with nullify second x derivative of the velocity profile. This is a linear phase of instability. At time $t=800$, modulation instability is fully developed, however the amplitude of the electric field is still very small (Figure 9). At time $t=2600$, the amplitude of the field is already large (Figure 10).

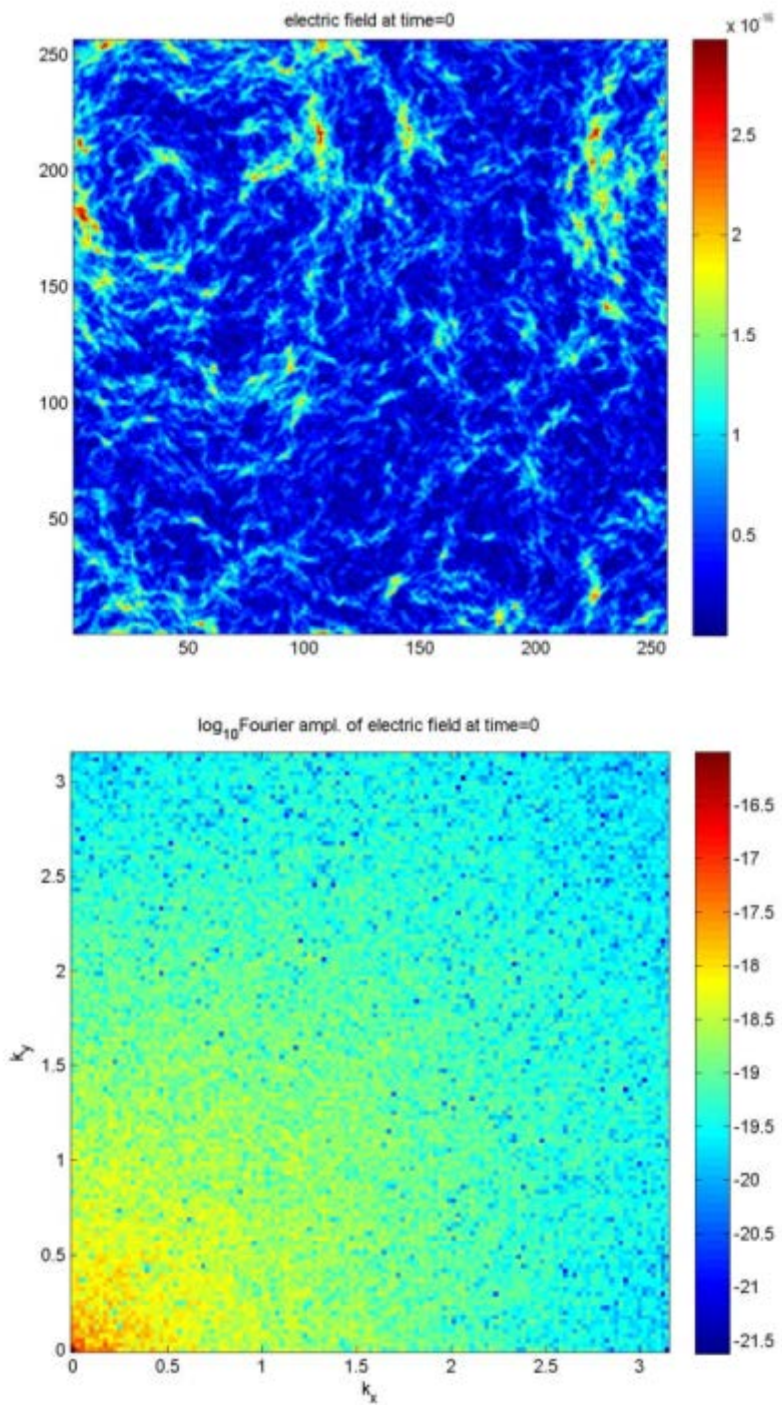


Figure 7: Initial ($t = 0$) electric field distribution (square of electric field) in dimensionless units (top) and 2D spatial spectrum of electric field (bottom).

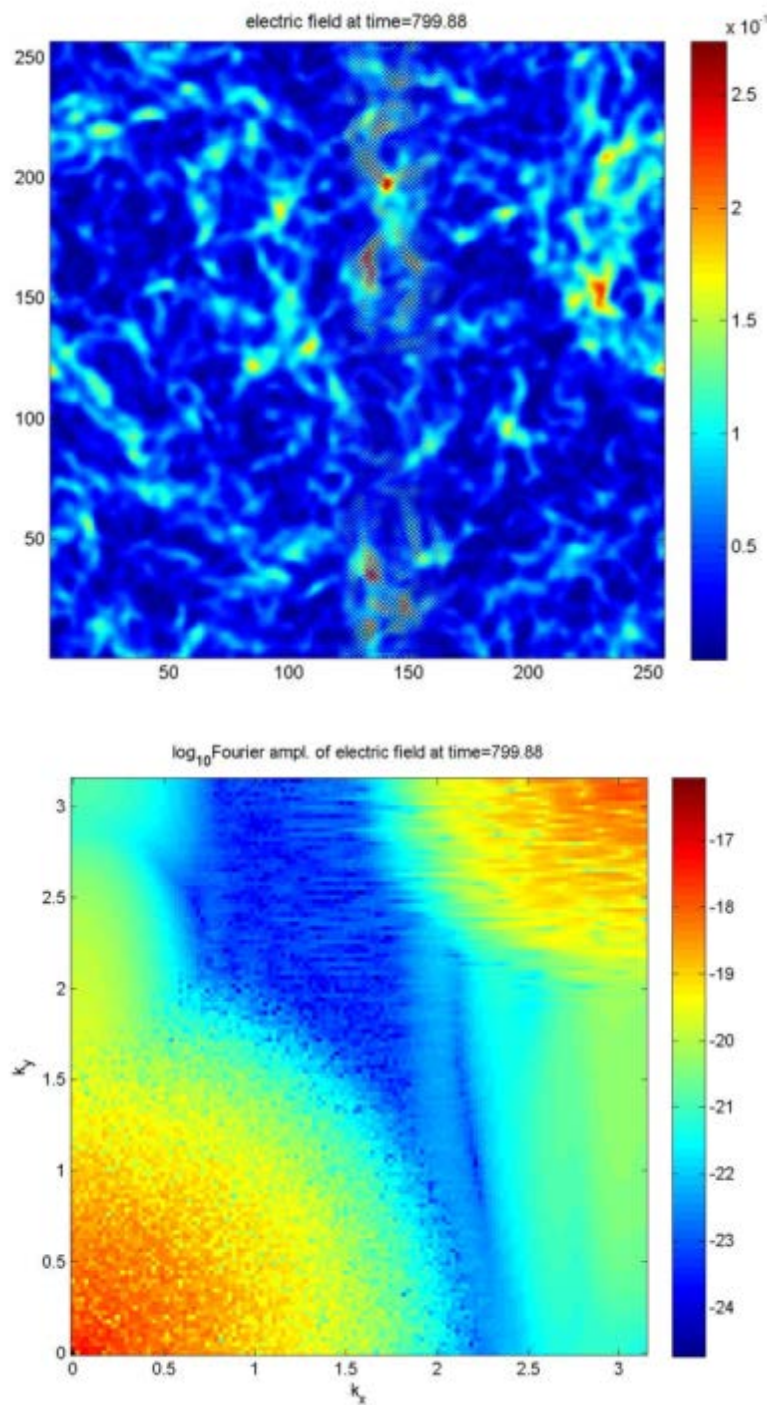


Figure 8: Electric field distribution (top) and its 2D spectrum (bottom) at time $t = 800$; instability just starts to develop.

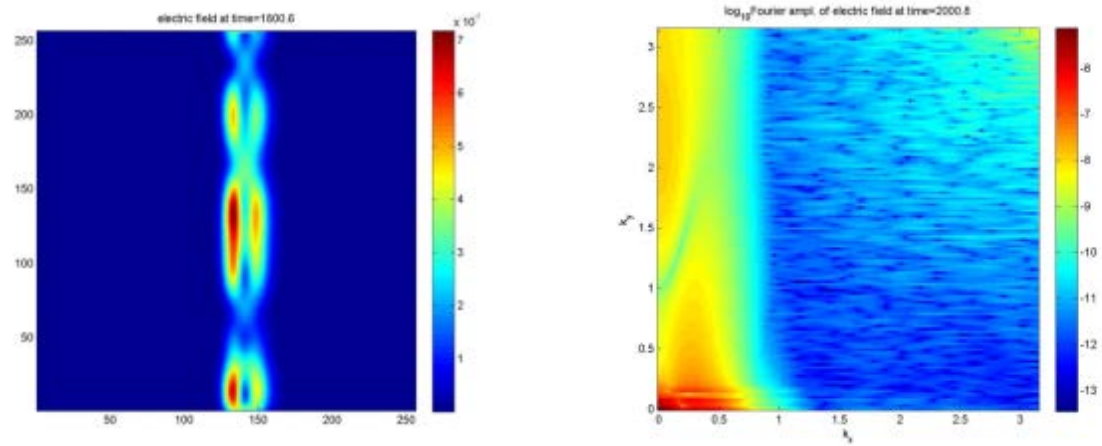


Figure 9: Electric field distribution (at the left) and its 2D spectrum (at the right) at time $t = 1800$; modulation instability is fully developed, amplitude is still small.

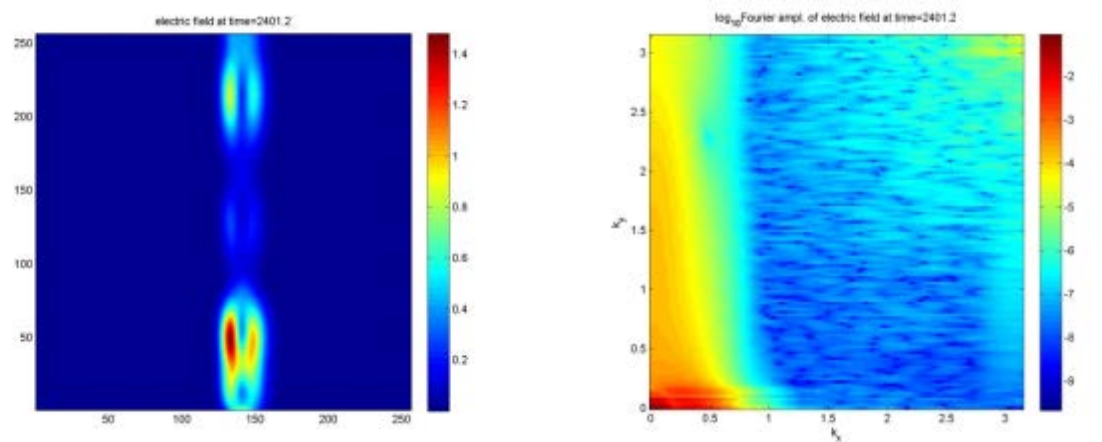


Figure 10 : Electric field distibution (at the left) and its 2D spectrum (at the right) at time $t = 2400$; amplitude is already large.

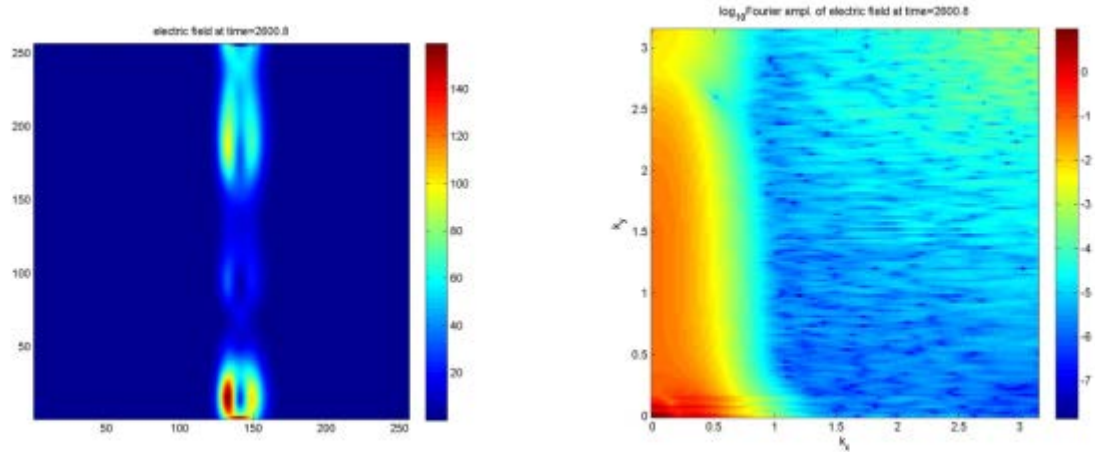


Figure 11: Electric field distribution (at the left) and its 2D spectrum (at the right) at time $t = 2600$; amplitude is very large.

Figure 12 shows the dynamic of modulation instability development. Linear instability is dominant up to the time $t = 2612$. Plasma density “begins to feel it” only after time $t = 1600$. Starting from $t = 2615.5$, the nonlinear terms become comparable with linear terms and then quickly overcome the latter. However this state is already out of model applicability.

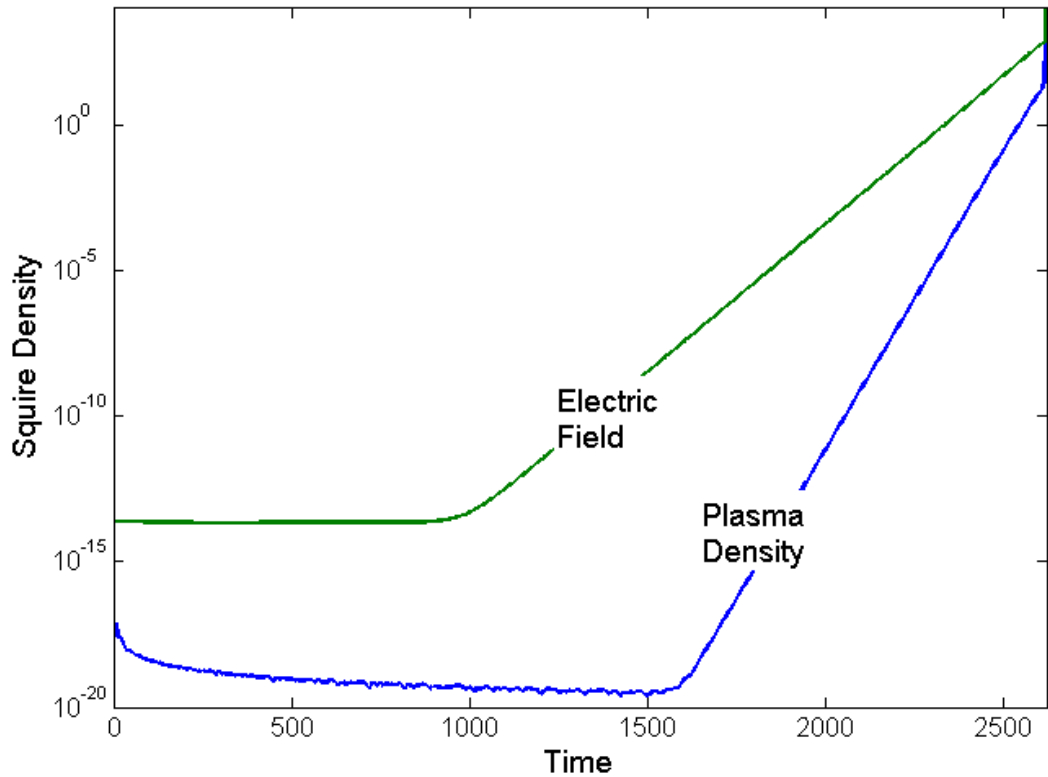


Figure 12: Square of electric field and square of plasma density as a function of time.

Figure 13- 16 show the results of spatial distribution of plasma density irregularity as well as their 2D spatial Fourier spectrum for the different moments of time. One may observe that up to the time $t = 1600$, nonlinear term is negligible and plasma density does not “feel” local increase of the

electric field. Starting from $t = 1600$, plasma density increases from the side of positive first derivative of velocity profile and decreases from the side of negative first derivative of velocity profile (Figure 13). This happens when the amplitude of the electric field increases up to 10^{-4} (in dimensionless units). Then, the spatial profile of plasma density remain essentially the same. However, the density quickly increases from 10^{-9} at $t=1600$ (Figure 13) to 10^{-7} at $t=1800$ (Figure 14) to 10^{-1} at $t=2400$ (Figure 15). Finally, the amplitude becomes larger than unity, which means that limitations of the model applicability are already exceeded (Figure 16).

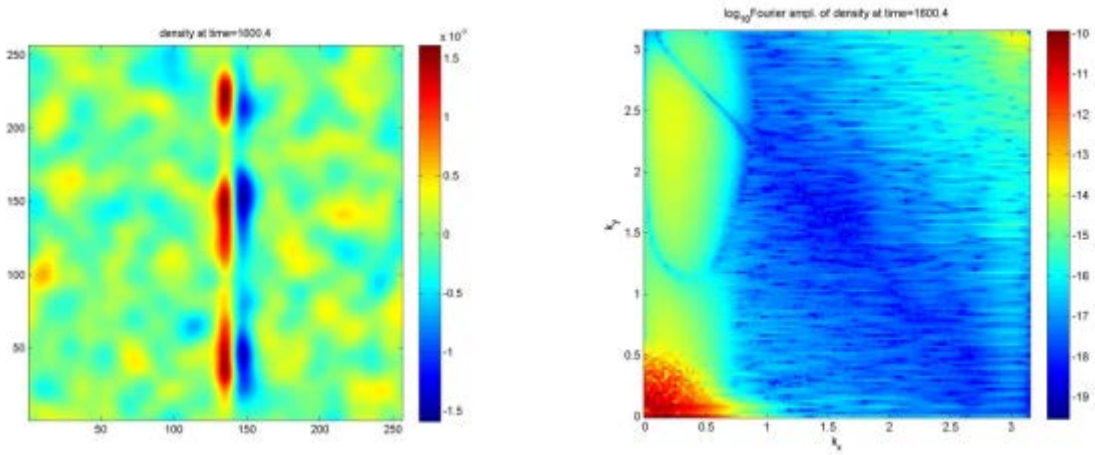


Figure 13: Plasma density irregularity spatial distribution at the left) and its 2D spectrum (at the right) at time $t = 1600$; nonlinear term starts to play only when electric field increases up to 10^{-4} .

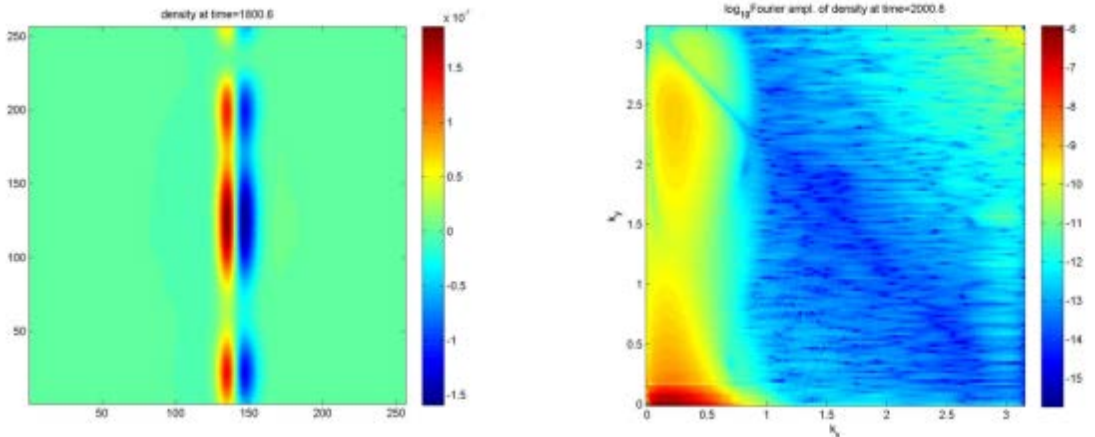


Figure 14: Plasma density irregularity spatial distribution at the left) and its 2D spectrum (at the right) at time 1800; instability is fully developed, amplitude is still small.

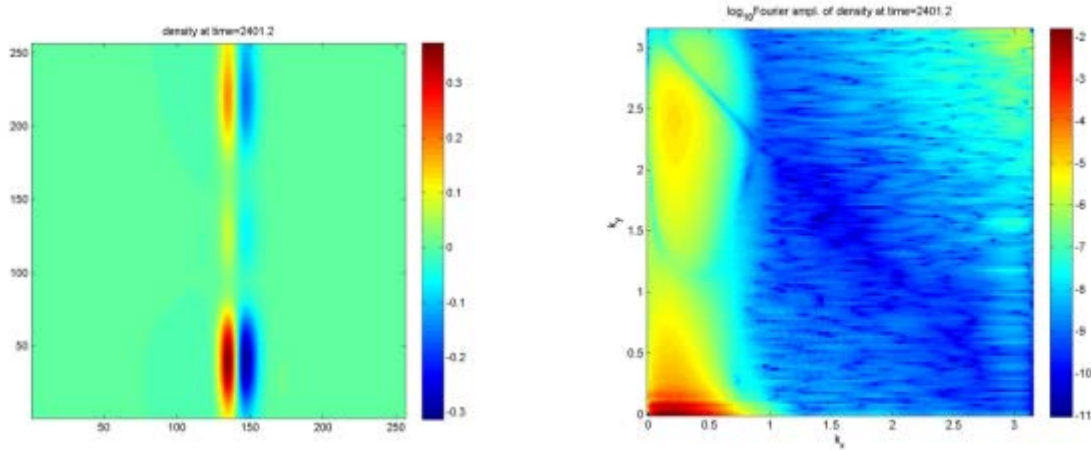


Figure 15: Plasma density irregularity spatial distribution (at the left) and its 2D spectrum (at the right) at time $t = 2400$; amplitude is large already.

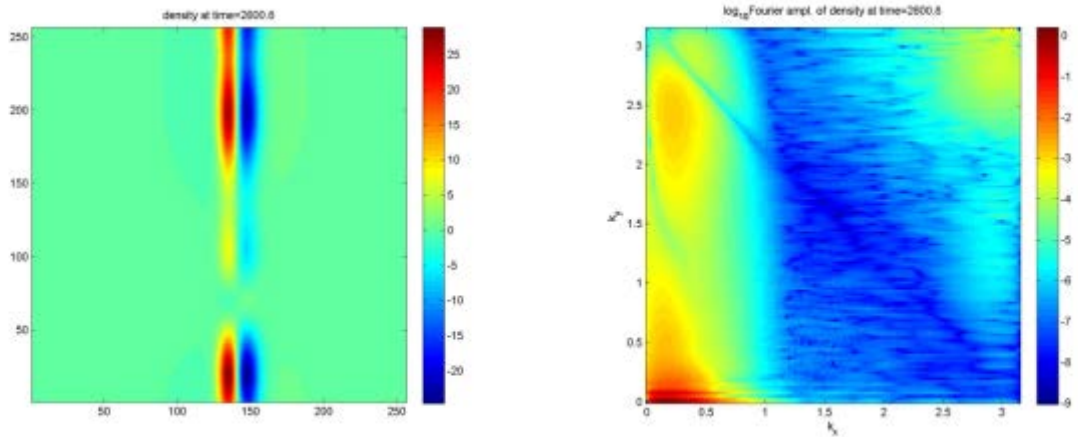


Figure 16: Plasma density irregularity spatial distribution (at the left) and its 2D spectrum (at the right) at time $t=2600$. Amplitude is very large (more than 1), this stage is already out of model applicability.

3.4 Modulation Instability of magneto sonic waves

For the parameters of ionosphere plasma considered above, the parameter C has a value $0.71 \cdot 10^{-7}$. Comparison of the results of calculation of instability dynamics with this value of C with the results obtained in the previous section on page 16 shows that they are practically identical. In other words, the electromagnetic correction term is negligible, i.e., C is too small. However, in a case when plasma has such conditions that C is larger than 10^{-6} (for example for plasma with density order of magnitude larger than was used in the above example) the influence of the correction term becomes obvious. Figure 17-21 depict the electric field distribution for the lower-hybrid and magnetosonic waves at different times. One can see that at earlier time ($t=400$) the electric field still has a stochastic distribution in the case of lower-hybrid waves, i.e., instability is not developed yet. In contrast, in the case of magnetosonic waves 1) the amplitude of the field is in order of magnitude larger and 2) the large-scale structure is developed (Figure 17). The same is true for the $t=600$.

However, now amplitude difference is in two orders of magnitude and large-scale objects start to align along y-axis for the magnetosonic waves (Figure 18).

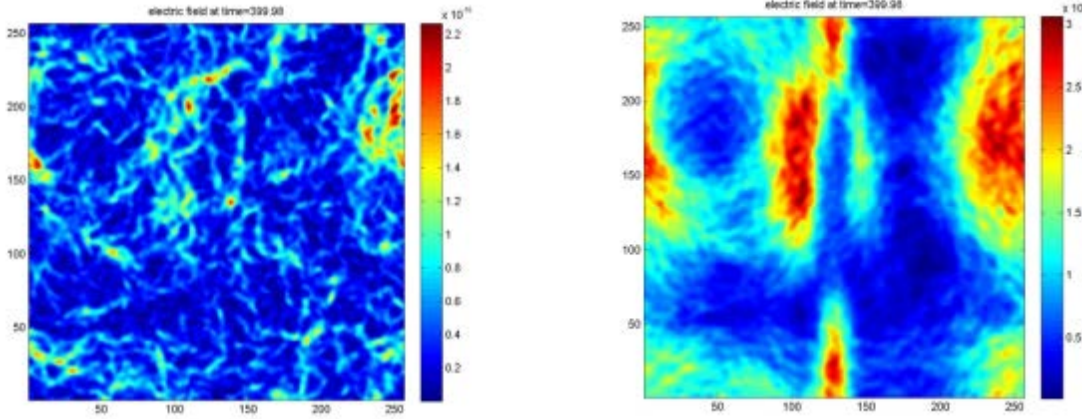


Figure 17: Electric field distribution for lower-hybrid (at the left) and magnetosonic (at the right) waves after $t = 400$. The difference is visible: stochastic distribution of the field for the lower-hybrid waves in contrast to magnetosonic waves where amplitude of the field is order of magnitude larger and large-scale structure is developed.

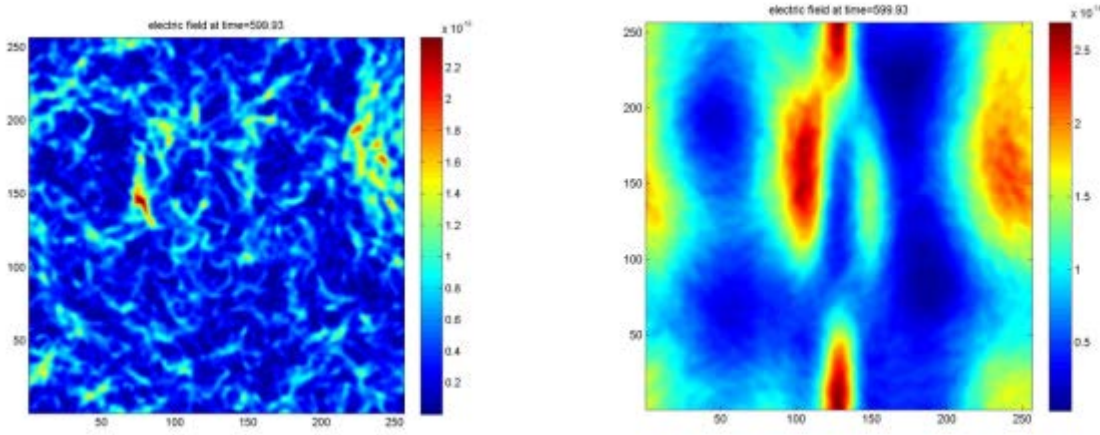


Figure 18: Electric field distribution for lower-hybrid (at the left) and magnetosonic (at the right) waves after $t = 600$. Instability is not developed for the lower-hybrid waves (still stochastic distribution). Large-scale objects start to align along y-axis for the magnetosonic waves. Amplitude of the magnetosonic waves is larger than amplitude of the lower-hybrid waves in two orders of magnitude.

At time $t = 1000$, the modulation instability is developed for the lower-hybrid waves, but is not yet developed for the magnetosonic waves. The large-scale objects aligned along y-axis are still in place for the latter waves and amplitude of these waves is larger than amplitude of the lower-hybrid waves by four orders of magnitude (Figure 19). At time $t = 1400$, instability is fully developed for the lower-hybrid waves and just start to develop for the magnetosonic waves. The amplitude of the waves is in the same order of magnitude already (Figure 20). Finally, starting from the time $t=1600$, the electric field distribution and plasma density distribution are almost indistinguishable between lower-hybrid and magnetosonic waves (Figure 21 and Figure 22). Here we observe the transition of magnetosonic wave to lower-hybrid wave predicted by Shapiro et al. [19].

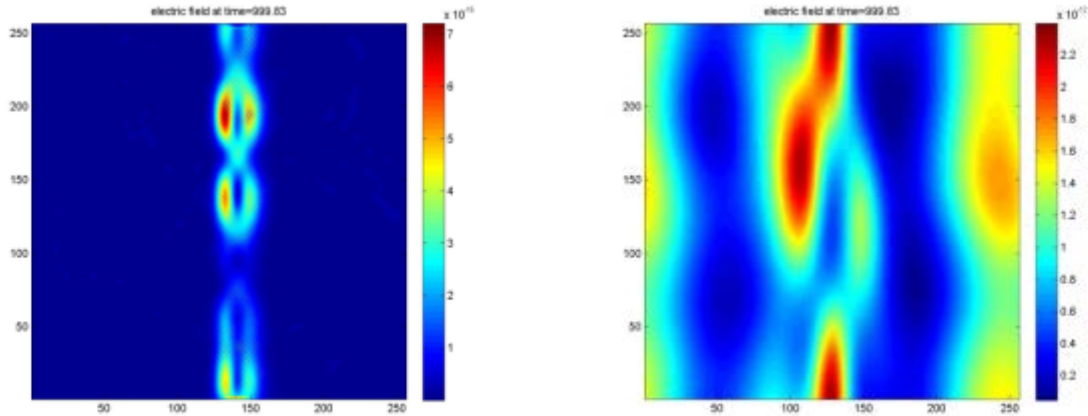


Figure 19: Electric field distribution for lower-hybrid (at the left) and magnetosonic (at the right) waves after $t = 1000$. Modulation instability is developed for the lower-hybrid waves. Large-scale objects aligned along y-axis are still in place for the magnetosonic waves. Amplitude of the magnetosonic waves is larger than amplitude of the lower-hybrid waves in four orders of magnitude.

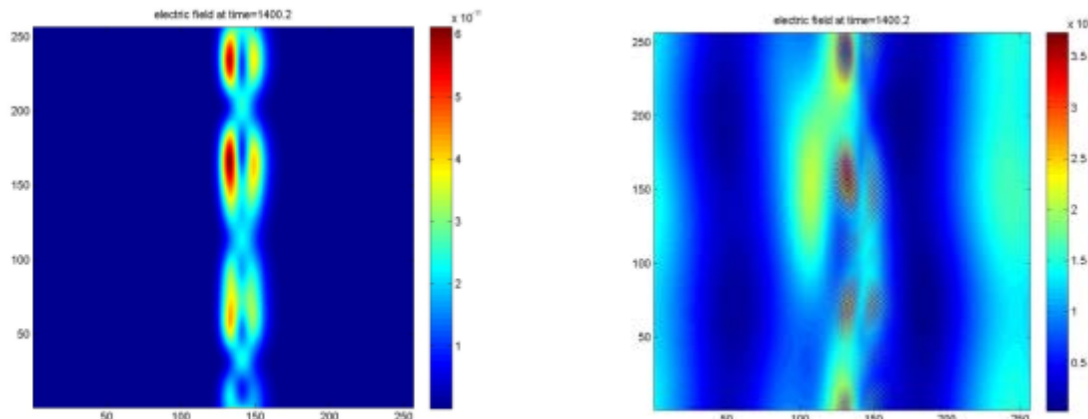


Figure 20: Electric field distribution for lower-hybrid (at the left) and magnetosonic (at the right) waves after $t = 1400$. Modulation instability is fully developed for the lower-hybrid waves and just start to develop for the magnetosonic waves. The amplitude of the wave is in the same order already.

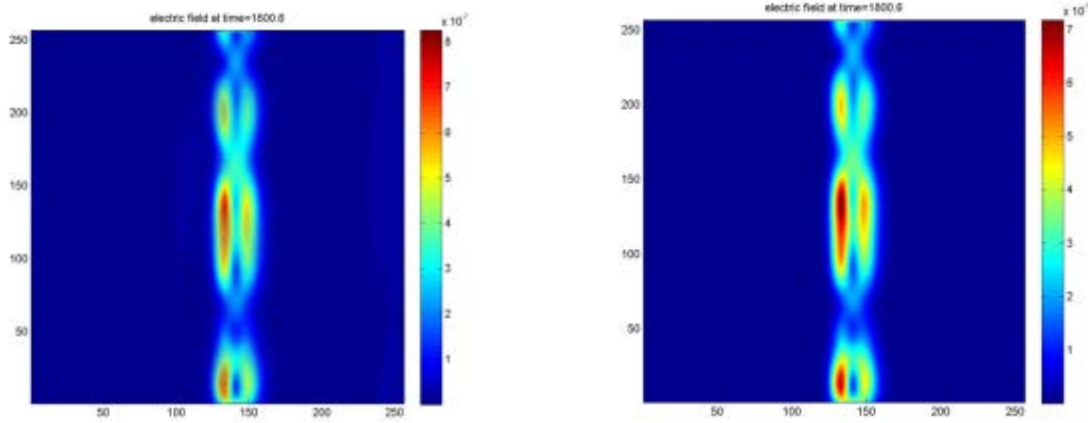


Figure 21: Electric field distribution for lower-hybrid (at the left) and magnetosonic (at the right) waves after $t = 1600$. Starting from this time, the electric field distribution is almost indistinguishable between lower-hybrid and magnetosonic waves.

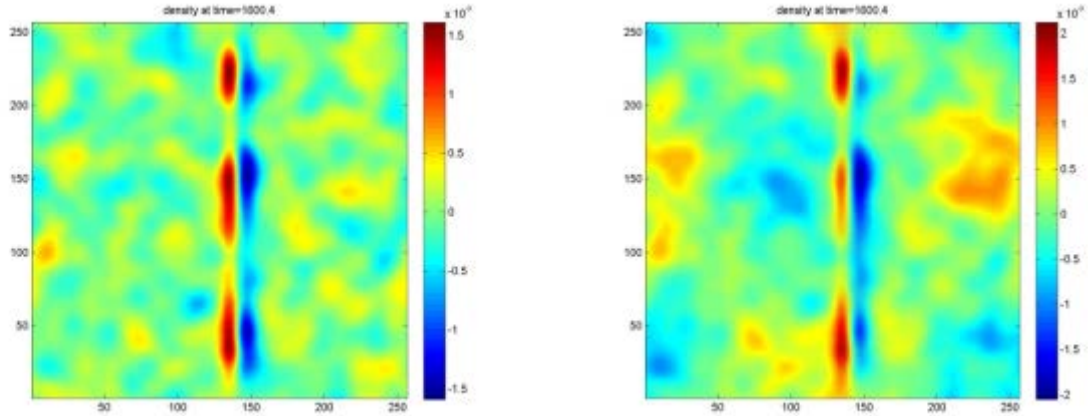


Figure 22: Plasma density distribution for lower-hybrid (at the left) and magnetosonic (at the right) waves after $t = 1600$. Starting from this time, the density distribution is almost indistinguishable between the two types of waves.

3.5 Influence of electron- neutral collisions

Electron – neutral collision may essentially affect the development of modulation instability. Indeed, as we can see in Figure 23 the increase of value of the electron – neutral collision coefficient 1) increases the time necessary for instability development and 2) decreases the increment of instability development. Moreover, if collision frequency is too large the modulation instability is not developed (see dotted curve at Figure 23). This work corresponds to the implementation of the second task of the project (Task 2: Modify developed “Beavercreek 2D” code to include electron-neutral collisions and density gradients).

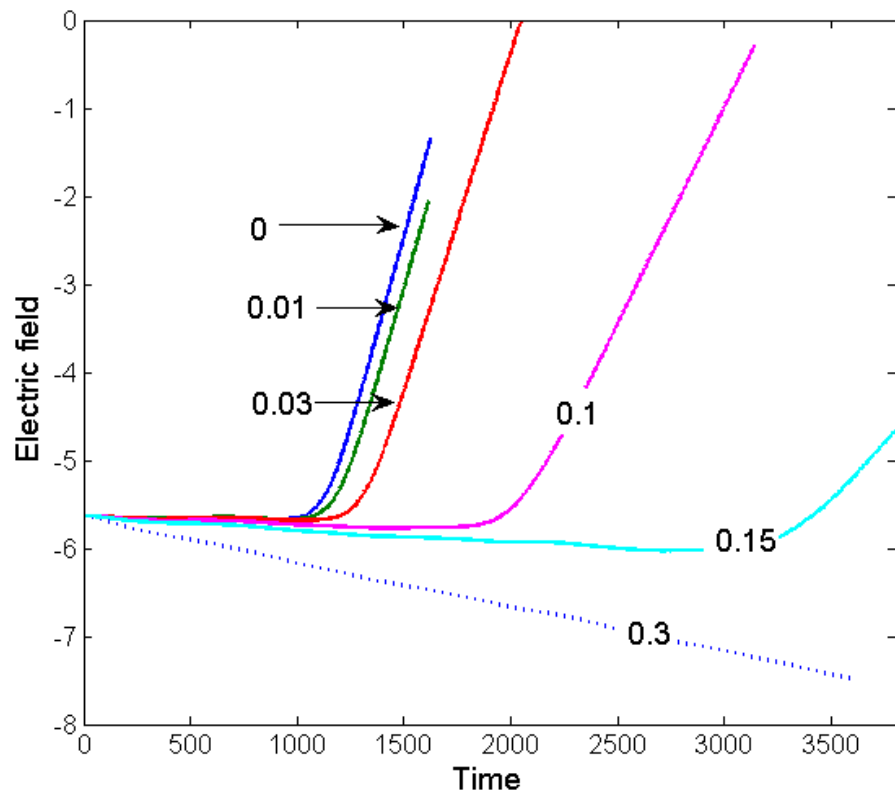


Figure 23:Squire of electric field density as a function of time for various values of normalized electron-neutral collision coefficient.

4.0 Analytical and Experimental Investigations High frequency RF Interaction With Localized Density Structures at the Naval Research Laboratory

In a series of experiments, Amatucci *et al.* [13] demonstrated that strongly sheared electron flows perpendicular to the background magnetic field with scale size smaller than an ion gyroradius but larger than an electron gyroradius can drive electrostatic oscillations near the lower hybrid frequency. These observations were consistent with the theoretical predictions of Ganguli et al. [11] and Ganguli and Romero [12] and lent support to the relaxation scenario for highly stressed magnetospheric boundary layers. For example, during intense solar activity, the plasma sheet boundary layer can become highly compressed, with gradients in the plasma across the layer self-consistently generating localized electric fields and highly sheared flows across the magnetic field. These sheared flows generate plasma instabilities that work to dissipate differential flows and widen the boundary layer. An analogous situation can arise in the flowing plasma surrounding a hypersonic vehicle, resulting in the generation of strong plasma turbulence.

The experiments on the generation of shear-driven lower hybrid waves were conducted in the Space Physics Simulation Chamber (SPSC) at the Naval Research Laboratory. The main chamber part of the SPSC consists of a 1.8 m diameter, 5 m long cylindrical vacuum vessel designed for controlled, scaled experiments of space plasma processes. For these experiments, a large area (~ 75 cm diameter) hot filament plasma source was placed at one end of the chamber, while a smaller filament source (~ 2 cm diameter) is placed at the opposite end. As can be seen in a schematic of the experimental setup in Figure 24, an isolated electrode blocks a small portion of the plasma generated by the large area source, which is filled with the plasma generated by the small plasma source. The blocking disk and the outer grid of the small source allow for control over the plasma potential of the small area plasma column. Strong radial dc electric fields can be generated by this steep variation of plasma potential across the cylindrical boundary layer between the two plasmas. This in conjunction with the filament heater currents on both sources enables independent control over the electric field and density gradients across the boundary of the two interpenetrating plasmas, simulating the stressed plasma sheet boundary layer conditions.

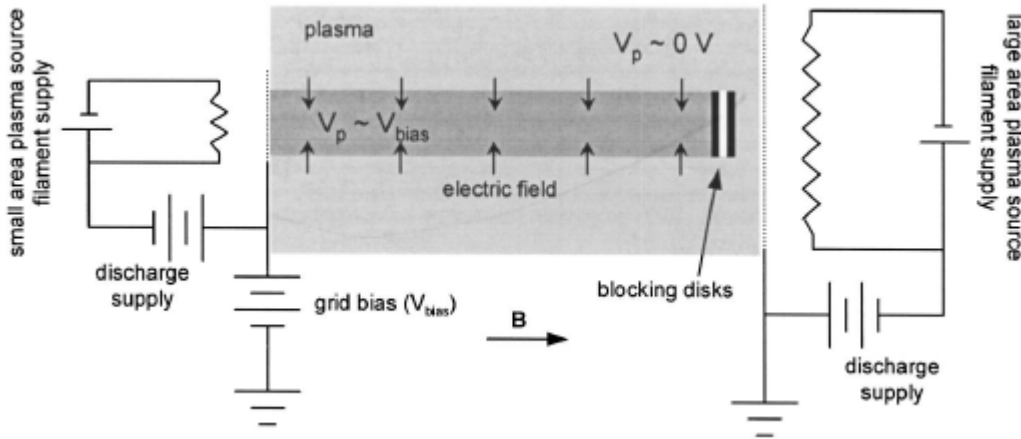


Figure 24: Schematic diagram of the experimental setup showing the two interpenetrating plasmas.

Typical parameters for the steady-state argon plasma are: plasma density $n \sim 10^9\text{-}10^{10} \text{ cm}^{-3}$, ion and electron temperatures $T_i \sim 0.05 \text{ eV}$ and $T_e \sim 0.25 \text{ eV}$, ion and electron thermal speeds $v_{ti} \sim 5 \times 10^4 \text{ cm/s}$ and $v_{te} \sim 2 \times 10^7 \text{ cm/s}$, and an axial magnetic field $B = 40 \text{ G}$. This yields ion and electron gyrofrequencies $\Omega_i \sim 1.5 \text{ kHz}$ and $\Omega_e \sim 110 \text{ MHz}$, ion and electron gyroradii $\rho_i \sim 3.5 \text{ cm}$ and $\rho_e \sim 0.03 \text{ cm}$, and lower hybrid frequency $f_{LH} \sim 400 \text{ kHz}$. The neutral density n_n is variable from $10^{11}\text{-}10^{14} \text{ cm}^{-3}$, and the plasma column diameter and effective length are 75 cm and 3 m, respectively.

Plasma potential was measured using radial emissive probes. The derivative of the resulting profile is the electric field profile. The measured electric field yields a typical transverse electric field scale length L_E from 0.6-1.0 cm ($0.17\text{-}0.3 \rho_i$) and the magnitude can be controlled up to 40 V/cm. Typical plasma potential (solid line without symbols) and electric field (dashed line) radial profiles can be seen in Figure 25. Since the electric field scale length is in the range $\rho_e < L_E < \rho_i$, the electrons $\mathbf{E} \times \mathbf{B}$ drift but the ions do not. For sufficiently strong electric fields, an instability with frequency in the lower hybrid frequency range is observed within the shear layer. Figure 25 shows an overlay of mode amplitude (solid circles) as a function of radial position localized to the edge of the transverse electron flow layer. A sample wave spectrum is also inset showing a mode with frequency $\sim 780 \text{ kHz}$ ($\sim 1.9 f_{LH}$), indicating that sheared transverse electron flows without the presence of a density gradient can drive lower hybrid waves.

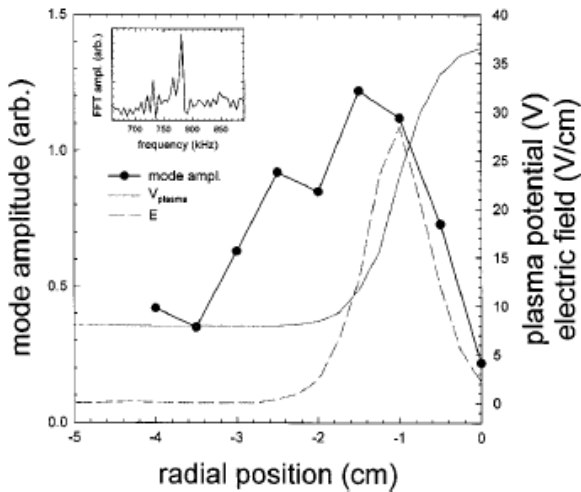


Figure 25: Radial profile of lower hybrid wave amplitude for the uniform density case and wave spectrum as inset.

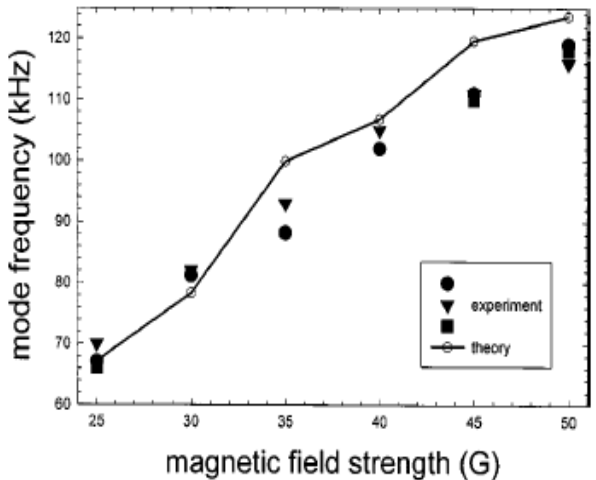


Figure 26: Comparison of experimentally observed (filled symbols) and theoretically predicted (line) values of mode frequency as a function of magnetic field strength.

Figure 26 shows a comparison between theoretically predicted mode frequency for these velocity shear-driven waves and the experimentally measure values as a function of the magnetic field strength. There is good agreement between the theoretical predictions and the measure mode frequencies. The observed instability also exhibits a threshold electric field ($\sim 7.5 \text{ V/cm}$) for the waves to appear. This coupled with the spatial localization of the mode amplitude to the shear layer suggests that the shear in the electron $\mathbf{E} \times \mathbf{B}$ flow is responsible for driving the observed lower hybrid waves.

While these experiments were scaled to magnetospheric boundary layer conditions, they could equally be applied to hypersonic vehicle plasmas. Future experimentation will focus on increasing the overall size of the flowing plasma region while maintaining the steep gradients. By driving the mode well in the nonlinearly saturate state, we will investigate the formation of turbulent plasma density structures and the effect of such structures on the scattering and transmission of electromagnetic waves.

Building on this experience, we have designed a large linear plasma source to generate sheet plasma that can be biased in the same manner as the small area cylindrical plasma source used previously. The linear source has several advantages for this project: the large sheet plasma and subsequent large area of plasma turbulence will present a simpler target for the electromagnetic waves used in the scattering experiments and the slab geometry is the same as that used in the theory, which will make for easier comparison between theory and experiment. The linear source is approximately 1 meter tall and generates a plasma that is approximately 4-8 ion gyroradii wide using thermionically emissive filaments. For typical plasma parameters and magnetic fields used in the experiments, this translates to a plasma sheet that is 10-20 cm wide. This plasma sheet will be immersed in a background plasma that is approximately a 1 m square. Figure 27 shows a photograph of the linear source in the SPSC. We have characterized the plasma generated by the linear plasma source and some representative profiles are shown in Figure 28. The width of the plot is equivalent to the size of the chamber. The line at the top of the plot represents the blocking disk that will be used to block the background plasma and bias the plasma sheet. The purple bars represent the size of the background plasma column.

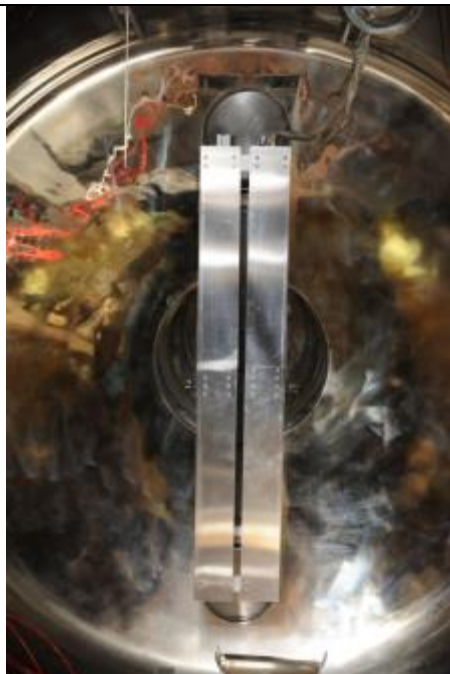


Figure 27: New linear plasma source installed in the SPSC.

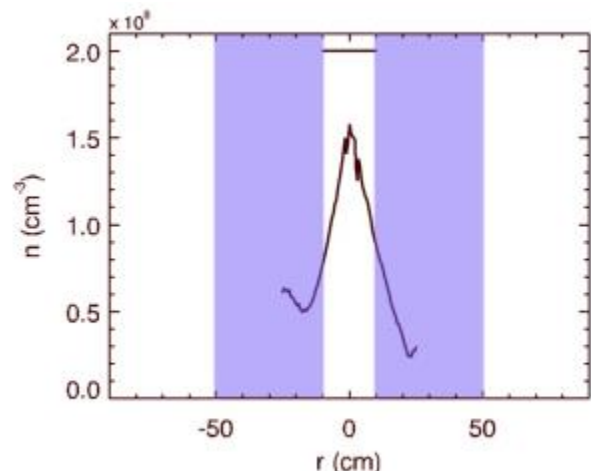


Figure 28: Density profile produced by new linear plasma source with the width of the plot representing the size of the chamber. The blocking disk is shown at the top of the plot and the purple bars represent the size of the background plasma.

The presence of plasma turbulence can strongly influence the propagation characteristics of electromagnetic signals used for surveillance and communication. In particular, we are interested in the generation of low frequency plasma turbulence in the form of coherent vortex structures coexisting with short scale density irregularities. These coherent vortex structures are characteristic of lower hybrid turbulence, and we will study the effects of this turbulence driven by two types of plasma instabilities. The first type is the Electron-Ion Hybrid (EIH) instability, which is driven by in-homogeneities in the flow of a magnetized plasma where the scale size of the inhomogeneity is smaller than the ion gyroradius. In this limit, the instability will be generated near the lower hybrid frequency and the nonlinear state has been shown simulations to exhibit the desired structure. The second type is the interchange or flute instability in a magnetized plasma that is associated with the Rayleigh-Taylor instability. Both of these density irregularities play an important role in refraction and scattering of high frequency electromagnetic signals propagating in the Earth's ionosphere, in the sheath of reentry and hypersonic vehicles, and in many other applications.

The scattering of high-frequency (HF) electromagnetic (EM) waves is a fundamental phenomenon in plasma physics. In a stable plasma EM scattering occurs due to Thomson scatter, which is scattering from thermal electron density fluctuations. The nonlinear interaction of waves in a plasma can also lead to scattering off of the density fluctuations due to the daughter waves from a parametric decay of a large amplitude wave. Scattering can also take place due to the interaction of HF waves with electrostatic solitons or from charged dust particles. In this project, we seek to analyze the formation of plasma density irregularities due to the development of lower hybrid velocity-driven and interchange instabilities. These types of density of density irregularities play an important role in the analysis of high frequency EM scattering and refraction in the ionospheric plasma, since the spatial scales of these plasma waves are comparable or smaller than typical wavelengths of EM signals used for surveillance, communication, and OTH radar applications.

4.1 Linear Theory Extension

In order to create a more realistic simulation of the plasma environment surrounding a hypersonic vehicle, we expanded the linear theory for the EIH instability to include density gradients and electron-neutral collisions. In order to make the simulation more representative of the experimental setup, we generalized the linear theory to cylindrical coordinates and assumed an azimuthally symmetric electric field profile. The results of the numerical shooting code can be seen in Figure 29. The theory does in fact predict an unstable mode for the experimental conditions, and the predicted eigenvalue is in good agreement with the observed values.

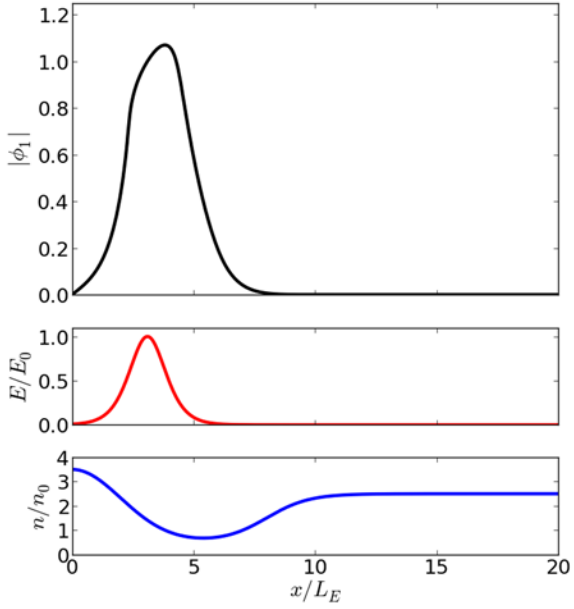


Figure 29: Typical eigenfunction magnitude (top pane) resulting from the numerical shooting code for experimental conditions with normalized electric field (middle pane) and density (bottom pane) profiles used in the calculations.

In order to arrive at the above solution, we tracked the pure EIH mode (without a density gradient) for experimental parameters as we slowly increase the density gradient until we reach the above profile. This ensures that the solution is the density gradient modified EIH mode. The mode shows a dramatic decrease of the real frequency of approximately 79% with the inclusion of a density gradient compared to the pure EIH solution. There is also a more modest decrease in the growth rate of approximately 26%. The location of the peak wave amplitude predicted by the theory is consistent with the experimental observations. The solution presented in Figure 29 exhibits the characteristic electric field threshold observed in the experiments.

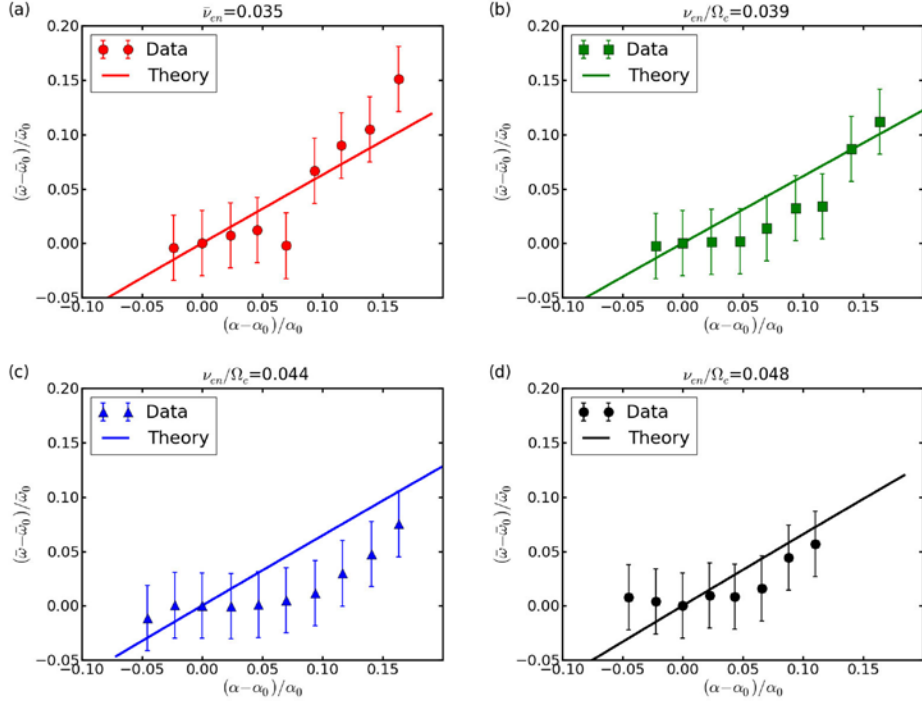


Figure 30: Comparison between trends in real frequency for theory and experimental data as the electric field is varied for various normalized electron –neutral collisions frequencies: (a) 0.035, (b) 0.039, (c) 0.044, and (d) 0.048.

Figure 30 shows a series of comparisons of the trends in the real frequency between theory and experimental data as the electric field is varied. Trends are shown as fractional variation from a reference level associated with an electric field that is just above threshold. Plotting the data in this fashion emphasizes the agreement in the frequency vs electric field trend, though the predicted real frequencies are still in relatively good agreement with the experimental data. The general trend of increasing observed real frequency as a function of maximum applied electric field is predicted by the theory. In general, a 15% change in the applied electric field yields a change in frequency of approximately 10-15%. It is important to note that the electric field in the experiment is the means by which we generate the plasma flows that are expected in the plasma environment surrounding a hypersonic vehicle. These trends are those that would be observed for different plasma velocities.

Plotted in Figure 31 is the variation in real frequency as a function of normalized electron-neutral collision frequency determined by the theory for four values of normalized $\mathbf{E} \times \mathbf{B}$ drift velocities. The four values of alpha correspond to experimental values of normalized electric field. Although the numerical predictions of the variation in the real frequency as a function of electron-neutral collision frequency do not decrease as quickly as the experimental observations, they do demonstrate the same general trend of decreasing frequency with increasing collisions frequency.

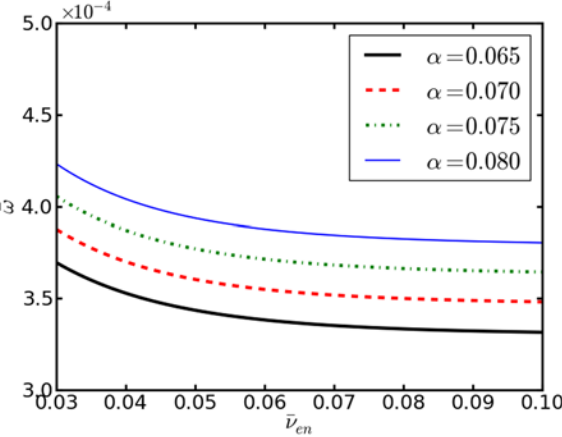


Figure 31: Variation in real frequency as a function of electron-neutral collision frequency as determined from the theory for four different normalized $E \times B$ drift velocities for experimental parameters.

The decrease in real frequency as the neutral pressure increases is due to the drag force imposed on the flowing electrons from collisions with neutrals. The collisions reduce the perturbed electron flow altering the Doppler-shifted frequency as seen by $\hat{\omega}_e = \omega_{1e} + iv_{en}$, which in general will lower the growth rate of the mode. It can also lower the real frequency since it enters the Poisson equation as $\hat{\omega}_e^2$ from the contribution to the density fluctuations due to the parallel wave electric field. In the theory, the electron-neutral drag force comes in through the momentum balance equation to first order and is neglected in the equilibrium calculations. It may be that the effects on the equilibrium flow need to be considered to fully capture the rapid rate at which the real frequency decreases in the experimental data. In addition, the theory does not reproduce the convergence of the real frequency for large values of neutral pressure as is demonstrated in the experiment. While we have conjectures about what might be causing this, we do not have the necessary experimental support to confirm these, and this behavior will be the subject of future research.

We demonstrated experimentally the substantial effects that collisions between charged and neutral species have in the development of the EIH instability. Not surprisingly charged/neutral collisions strongly affect the growth rate of these waves, though they do not stabilize the plasma. Increasing the neutral density relative to the electron density increases the threshold velocity required for the waves to develop and limits their saturation amplitude. Less intuitively, but of at least equal importance, the background neutral density affects the frequency of the dominant mode of the wave, not only reducing the frequency but reducing the dependence of frequency on the velocity as neutral density increases. The linear theory does a good job of reproducing the observed experimental results and gives us a firm foundation for exploring the nonlinear evolution of this instability.

4.2 EM Scattering Experiments

The scattering experiments that will be described in this section were intended to provide a solid foundation and develop the infrastructure for more complicated experiments of scattering off of turbulent structures. These experiments were conducted in three geometries, as shown in Figure 32. The first (baseline) geometry, shown in (a), launched microwaves in the x -direction into a plasma slab generated by a uniform linear array of electron-emitting filaments. The plasma naturally had a density variation in x but was uniform in y . Then, the filament array was re-arranged to introduce

periodic variations in the electron flux, and hence periodic variations in the plasma density, in the y -direction. The microwaves could then be emitted by a horn antenna aligned with either a minimum (Figure 32(b)) or a maximum (Figure 32(c)) in the plasma density. Microwave transmission through the plasma was monitored by an identical receiving horn antenna whose position on the far side of the plasma slab was movable.

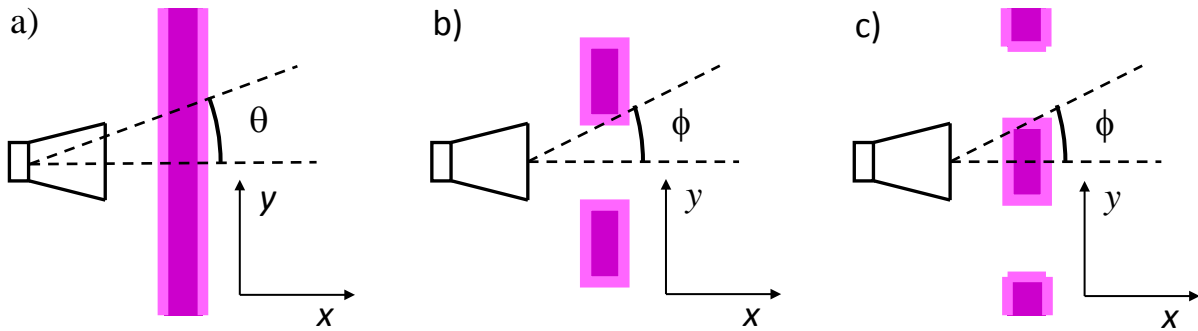


Figure 32: Experimental setup, in which microwaves were launched into a) a uniform plasma slab or b, c) a patterned plasma slab.

The plasma is well-localized in the x -direction, as shown in Figure 33 for the case of a relatively high magnetic field (100 G in the z -direction). The FWHM of the plasma depends primarily on the gyroradius of the plasma ions, and to a lesser extent on cross-field diffusion. When patterned, the profile of plasma density similarly depends on the magnetic field, and is shown in Figure 34, for several values of the magnetic field, B . As Figure 34 illustrates, increasing the magnetic field has two effects on the plasma structure of the patterned plasma: it increases the magnitude of the density gradients in the y -direction and it increases the “contrast” in the plasma—that is, the ratio between the maximum and minimum densities along the y -axis. The consequences of both of these effects may be seen in the behavior of microwaves traversing the plasma region.

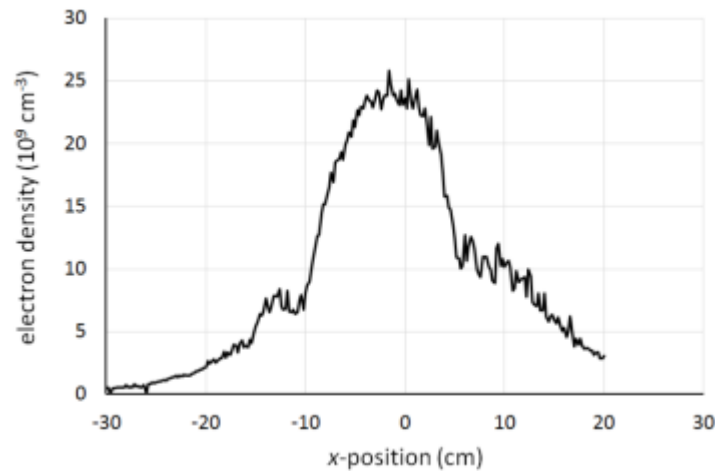


Figure 33: Typical profile of the plasma slab in the x -direction.

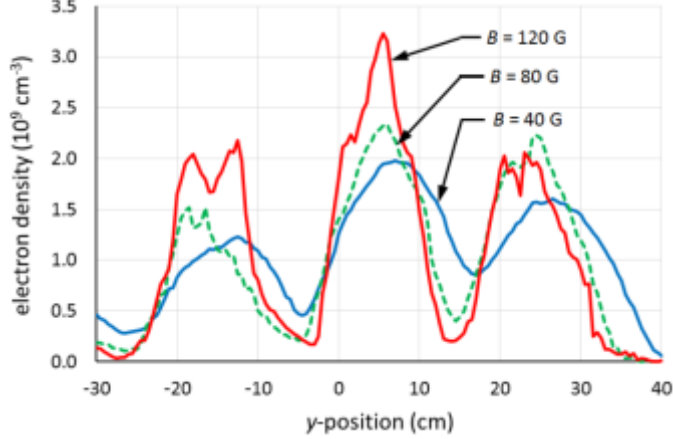


Figure 34: Representative density profiles of the plasma in the y-direction, with the patterned plasma slab.

Figure 35 shows the relative transmission of microwave power through the uniform plasma slab for three different microwave frequencies as a function of angle. The reference transmission level of $T = 1.0$ is taken to be the vacuum case at zero angle, where the primary lobe of the antenna pattern is centered without plasma present. The plasma density for this case is relatively high, $n_e = 2.7 \times 10^{10} \text{ cm}^{-3}$, and the behavior of microwaves at three different frequencies is shown, $f = 2.0$ GHz, 2.5 GHz, and 3.0 GHz. At the lowest frequency, the microwave is simply cut off in the plasma and cannot propagate through the plasma slab—we attribute any signal that is picked up in the receiving antenna to paths around the plasma, which would not be unusual since the vacuum chamber wall is entirely conducting. At the intermediate frequency, the wave is still cut off in the plasma, but unlike the lower-frequency case, the plasma sheet is not thick enough to entirely attenuate the wave. Both of these cases are behaving as expected.

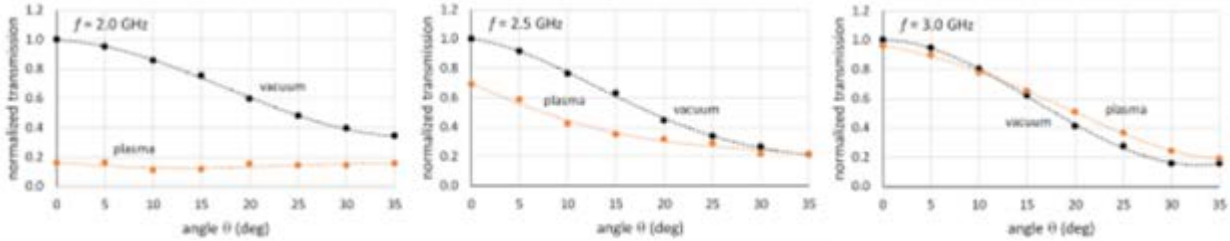


Figure 35: Microwave transmission through a uniform plasma slab at frequencies of 2.0, 2.5, and 3.0 GHz.

The behavior of the high frequency case is worth considering, because at a frequency of 3.0 GHz, the microwaves are well above the nominal cutoff frequency in the plasma. Nonetheless, the presence of the plasma slab has an effect on the transmission of microwaves through it. The presence of the plasma is a negative perturbation on the index of refraction, so that waves entering the plasma at other than normal incidence are bent away from the normal, by Snell's law. Since the antenna pattern of the transmitting horn antenna has some breadth, many of the wave fronts reaching the plasma will do so off-normal. We would then expect these waves to be refracted in such a way that the width of the antenna pattern with the plasma present increases, even though the plasma is transparent to the microwave radiation. This is just what we do, in fact, observe: at angles

larger than 10 degrees, the transmission through the plasma increases, relative to the vacuum case, at the expense of transmission at more shallow angles.

The effects of a plasma patterned in the y -direction are characteristically different than the effects arising from propagation through a uniform slab. The uniform slab may affect the amplitude of the transmitted wave substantially if the frequency of the wave is below the cutoff frequency, but the pattern remains single-lobed and forward directed. Figure 36 shows the transmission as a function of angle when the transmitting horn is centered at a minimum in the plasma density (that is, the case shown in Figure 32(b)) for microwave frequencies of 2.0 GHz, 2.4 GHz, and 2.8 GHz, respectively.

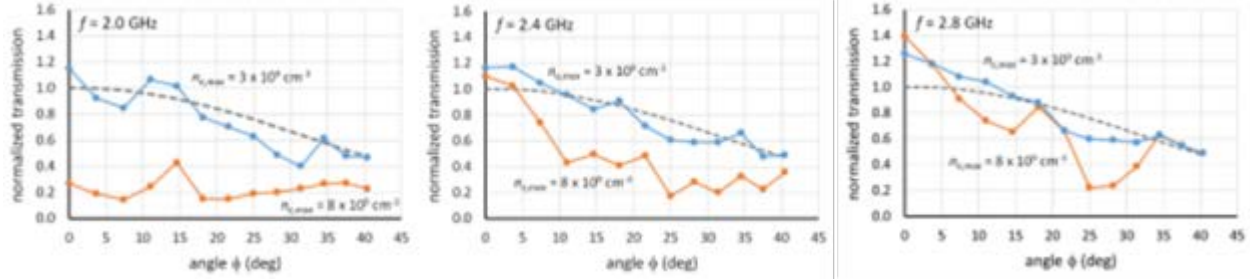


Figure 36: Microwave transmission through a density minimum in a patterned plasma slab at frequencies of 2.0, 2.4, and 2.8 GHz. The dashed line is the transmission through vacuum.

It is clear that the effects that are caused by the presence of the plasma are more pronounced with higher plasma density. The microwave signal may be attenuated (especially if the frequency is low compared to the cutoff frequency) but this is not universally true—there are also locations in space where the microwave signal is enhanced by several tens of percent compared to its vacuum-transmission value. Enhancement and attenuation depend not only on density but geometry, resulting in multiple lobes in the antenna pattern once it passes through the plasma.

The complementary data set, in which the transmitting antenna is aligned with a maximum in the plasma density, is shown in Figure 37 again for microwave frequencies of 2.0 GHz, 2.4 GHz, and 2.8 GHz, respectively. Directly opposite from the transmitting horn, the presence of the plasma attenuates the signal (and this is true whether the microwave frequency is above or below cutoff), but off-normal there are regions where the received microwave power is enhanced. Interestingly, in this particular geometry there are conditions where pronounced lobes in the antenna pattern appear off-axis.

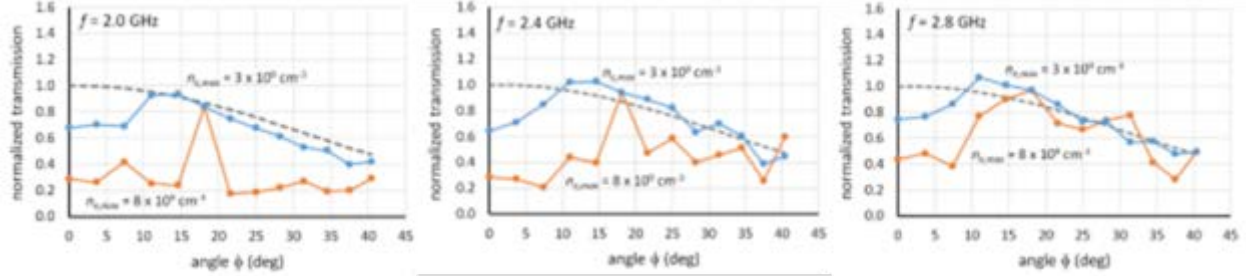


Figure 37: Microwave transmission through a density maximum in a patterned plasma slab at frequencies of 2.0, 2.4, and 2.8 GHz. The dashed line is the transmission through vacuum

We can arrive at additional insight into the processes involved in the microwave's interaction with the plasma by exploring the parameter space with a fixed geometry of the receiving antenna, specifically, at zero angle, aligned with the transmitting horn either through a minimum (Figure 32(b)) or a maximum (Figure 32(c)) in the plasma. Figure 38 shows the response for a variety of plasma densities for the same

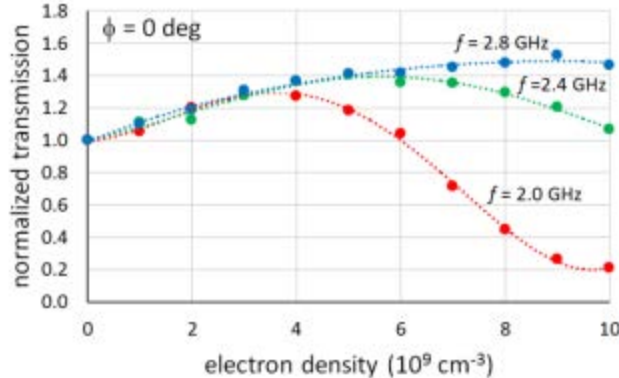


Figure 38: Transmission through a minimum in the plasma density for various frequencies used in Figure 36 and Figure 37

For each of these cases, the magnetic field was set to $B = 80\text{G}$, so the intermediate profile from Figure 34 is representative of the variation in the plasma density along the y -axis. The enhancement in the transmitted power varies from 30% to in excess of 50% depending on the microwave frequency used and the maximum plasma density. As the maximum plasma density increases beyond $n_e \max = 4 \times 10^9 \text{ cm}^{-3}$, we see that the lowest-frequency waves (2.0 GHz) are strongly cut off, the intermediate-frequency waves (2.4 GHz) are mildly but not completely cutoff, and the highest frequency waves (2.8 GHz) are essentially not cut off, for the range of densities used. The effects of the plasma are pronounced, however, well below $n_e \max = 4 \times 10^9 \text{ cm}^{-3}$ where none of the waves are operating in a cut off regime.

Figure 39 is the analog of Figure 38, except with the transmitting and receiving antennas aligned across a plasma maximum. Here, the net effect (a reduction in the transmitted power) is common across all conditions except for the case of $n_{e \text{ max}} = 4 \times 10^9 \text{ cm}^{-3}$ where the attenuation effect disappears and for some frequencies even a slight enhancement appears

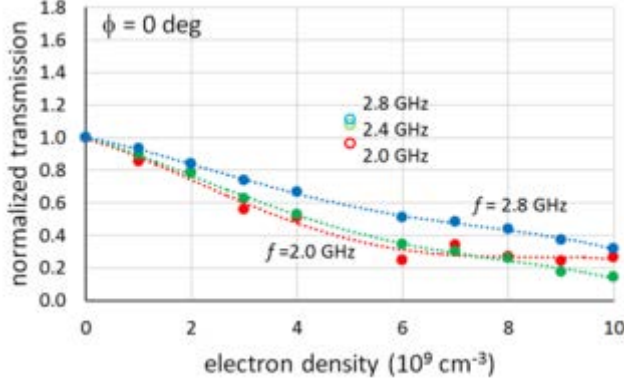


Figure 39: Transmission through a maximum in the plasma density for various conditions.

The picture becomes clearer when we take, for each microwave frequency and density, the average between the responses shown in Figure 38 and Figure 39. This is the best representation we can construct of the overall behavior of a plane wave front impinging on our patterned plasma across multiple structures. The results of this analysis are shown in Figure 40.

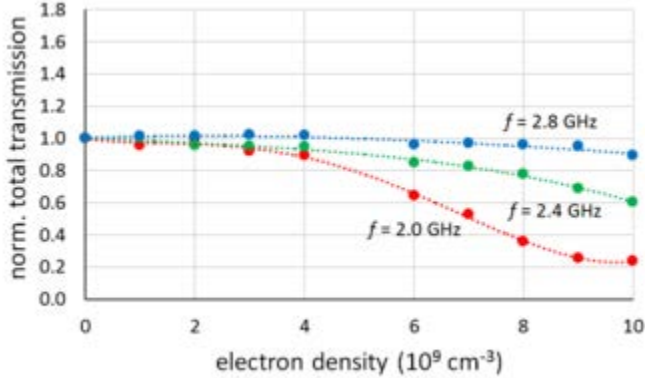


Figure 40: Total transmission through a patterned plasma slab as a function of density for different frequencies.

The result is an overall transmission of unity, independent of frequency, for low plasma densities, with the transmission falling off with increasing plasma density, and falling off faster for lower microwave frequencies.

The conclusion we can draw from these data is this: There is no physical mechanism for any substantial absorption of microwave power by the plasma, so no microwave power is lost when it impinges on the patterned plasma, but power is re-directed, and often to a substantial degree. The patterned plasma can act as both a reflecting and a refracting optical element, the former due to cutoff effects in the dispersion relation of the wave in the plasma, and the latter due to gradients in the index of refraction that the plasma introduces. Both effects occur simultaneously, and which is most important depends on the density and length scales in the plasma and the frequency of the microwaves themselves. Comparing Figure 38 and Figure 39, for example, we would say that refraction is the dominant mechanism for our setup when $n_{e \text{ max}} < 4 \times 10^9$. On the other hand, we

can look at the transmission through the plasma for different magnetic field configurations, shown in Figure 41 for low (2.0 GHz) and high (2.8 GHz) frequencies, respectively.

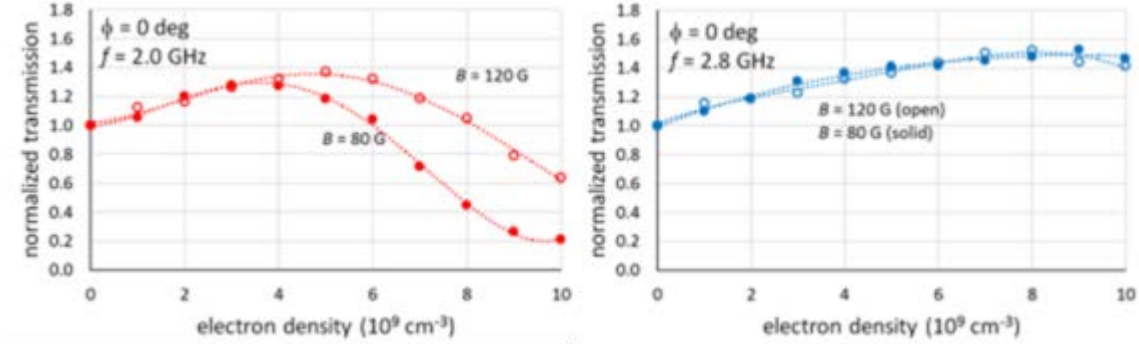


Figure 41: Transmission through a minimum in the plasma for two different magnetic field configurations at frequencies of 2.0 and 2.8 GHz.

We see that the effect of increasing the B -field from 80 G to 120 G is substantial for the low-frequency wave but negligible for the high-frequency wave. Looking at Figure 34, we would say that increasing the B -field from 80 G to 120 G increases the contrast between the maximum and minimum densities more than it does the gradient scale length. Since we are holding the maximum density constant, the chief effect of increasing the B -field is lowering the density in the minima, and this affects the reflection due to the plasma more than it affects its refraction—hence the deviation in the curves for 2.0 GHz, where increasing the field makes the plasma in the minima less reflective to waves below the cutoff frequency. In contrast, waves above the cutoff frequency see the plasma as a transparent medium, so the curves for 2.8 GHz lie on top of each other. However, just as a glass lens is transparent to visible wavelengths but nonetheless bends visible light, refraction occurs in this “plasma lens”.

The behavior of the waves traversing the patterned plasma seems consistent with a top-level understanding of plasma optics. However, even in these straightforward cases, there are features in the data (for example, the anomalous points in Figure 39) that point to the fact that the details of the plasma structure can be critical in producing substantial variations in transmission for particular conditions. A modeling effort, which will be important to fleshing out the physics behind the data presented here, should include sufficiently fine spatial and frequency resolution to reveal such behavior over relatively small ranges in parameter space.

4.3 EM Scattering Theory

Initial ray tracing simulations of the experiments described in the previous section have indicated complications due to the presence of both a cutoff and resonance for the microwaves in the plasma separated in space within a wavelength of the launched modes. Due to this, a full wave solution is necessary to capture all of the underlying physics. To model the uniform plasma slab experiments, we launch an initial wave and numerically integrate across the plasma density gradient to the receiving antenna. Since the microwave antenna launches polarized waves with the electric field directed perpendicular to the background magnetic field, it should predominantly launch the extraordinary wave. For normal incidence, we must solve the following differential equation:

$$\frac{d^2E_y}{dx^2} + \frac{\omega^2}{c^2} \left[1 - \frac{\omega_{pe}^2}{\omega^2} \frac{(\omega + iv_{en})^2 - \omega_{pe}^2}{(\omega + iv_{en})^2 - \Omega_e^2 - \frac{(\omega + iv_{en})}{\omega} \omega_{pe}^2} \right] = 0, \quad (32)$$

where ω_{pe} is the plasma frequency and is a function of x , Ω_e is the electron cyclotron frequency, and v_{en} is the electron-neutral collision frequency. Figure 42 shows the results from the numerical integration for normal incidence on a plasma slab matching the experimental conditions for three frequencies: 2.0, 2.5, and 3.0 GHz. The resulting transmission coefficients from these numerical runs are 0.02, 0.79, and 1.00 respectively. These results compare favorably for the 2.5 and 3.0 GHz cases, though the resulting transmission coefficient for the 2.0 GHz case is approximately an order of magnitude too low compared to the experimental results. This could be due to the fact that the antenna launches a broader spectrum than the purely normal incidence and these waves should all be taken into consideration when comparing to the experiment.

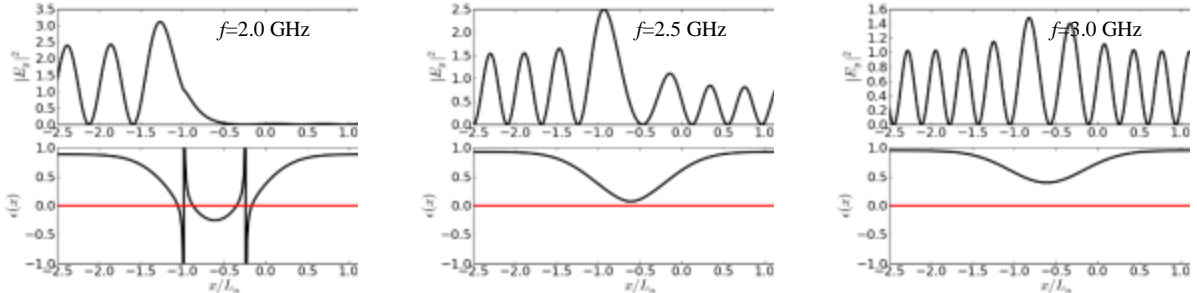


Figure 42: Results from numerical integration for normal incidence on a plasma slab matching experimental conditions for three frequencies: 2.0, 2.5, and 3.0 GHz.

In order to account for arbitrary propagation angle for the initial wave, we are writing a numerical shooting code that uses the full cold plasma dielectric tensor and solves the resulting fourth order equation for both the full wave electric field vector as a function of position. This code will launch an ensemble of waves for the full range of propagation angles scaled according to the antennas radiation pattern and aggregate the waves that intercept the receiving antenna. This code will allow us to examine the effects the angular dependence of the transmission coefficient.

4.4 Summary of NRL Effort

Over the past year, we have increased our numerical tools for modeling the unstable plasma environment when density gradients and sheared flows are present. These tools have been validated through careful experimental measurements. This effort has resulted in a solid foundation and predictive capability for the development of the nonlinear theory and numerical simulations. Experimentally, we have demonstrated the ability to generate the necessary environmental conditions and the resulting unstable behavior of the plasma leading to nonlinear structuring. In addition, the infrastructure and initial scattering experiments off stationary density structures have

been completed. Even these simplified experiments have demonstrated strong refraction and scattering of communications signals even when the plasma density is below the threshold for complete cutoff. It is also suspected that there is significant phase distortion resulting from these interactions. We shall continue to extend the theoretical and numerical modeling basis for the scattering of electromagnetic signals off turbulent density structures while continuing the experimental probing to validate these codes.

5.0 Interchange Instability

The interchange instability plays important role in understanding of physical processes in the earth ionosphere and magnetosphere. In particular it is considered as the driving mechanism for the equatorial spread F (ESF) events. In order to analyze interchange instability we employed a two-fluid non-ideal MHD model with inclusion of kinetic effects. This is a step forward in comparison with previously developed models. This approach allows us to resolve spatial scales of turbulent plasma density irregularities comparable with the ion Larmor radius – the spatial scale in the ionospheric F layer of the order of the wavelength of the OTH radar signals. This is the reason why it is important to develop a model which can adequately describe short scale plasma density irregularities. We formulated and derived system of nonlinear two fluid hydrodynamic equations for description of interchange turbulence with included kinetic effects in a high-beta and low beta plasmas and analyzed linear stage of interchange instability with plasma parameters relevant to the equatorial Spread F in the ionosphere. Next, we obtained analytical solutions to the nonlinear equations for density irregularities in the form of double vortex structures.

5.1 Nonlinear Equations for Description of Interchange Turbulence

Our analysis of the interchange instability will be based on the following complicated system of nonlinear equations for density N , electrostatic potential Φ and magnetic field δB_z :

$$\begin{aligned} \frac{\partial \Delta_{\perp} \Phi}{\partial t} - \frac{V_{Ti}^2}{\omega_{ci}} \frac{\kappa_N + \kappa_B}{1 + \frac{\beta}{2}} \frac{\partial \Delta_{\perp} \Phi}{\partial y} + \frac{g B_{0z}}{n_{i0} c} \left(1 + \frac{\rho_i^2 \frac{\beta_e}{2}}{1 + \frac{\beta}{2}} \Delta_{\perp} \right) \frac{\partial \delta n}{\partial y} - \\ \frac{V_{Ti}^2}{\omega_{ci} c} \left(\frac{\partial \Delta_{\perp} \delta B_z}{\partial t} + \frac{g}{\omega_{ci}} \frac{\partial \Delta_{\perp} \delta B_z}{\partial y} \right) - \frac{g}{\omega_{ci}} \left(\frac{\partial \Delta_{\perp} \Phi}{\partial y} + \frac{V_{Ti}^2}{\omega_{ci} c} \frac{B_{0z}}{n_{i0}} \frac{\partial \Delta_{\perp} \delta n}{\partial y} \right) = \\ \frac{V_{Ti}^2}{\omega_{ci} n_{0i}} \vec{\nabla}_{\perp} \cdot \{ \vec{\nabla}_{\perp} \Phi, \delta n \} + \frac{c}{B_{0z}} \{ \Delta_{\perp} \Phi, \Phi \} \end{aligned} \quad (33)$$

$$\frac{\partial \delta n}{\partial t} + \frac{c}{B_{0z}} \frac{\kappa_N + \kappa_B}{1 + \frac{\beta}{2}} \frac{\partial \Phi}{\partial y} - \frac{\beta_e V_{Ti}^2}{\beta_i \omega_{ci}} \frac{\kappa_B - \frac{\beta}{2} \kappa_N}{1 + \frac{\beta}{2}} \frac{\partial \delta n}{\partial y} = \frac{c}{B_{0z}} \{ \delta n, \Phi \} \quad (34)$$

$$\delta B_z = \frac{\beta}{2} \delta n \quad (35)$$

In equations (33)-(35) we used quasi-neutrality condition $\delta n_i = \delta n_e = \delta n$ and Poisson brackets are defined as:

$$\{a, b\} = \frac{\partial a}{\partial x} \frac{\partial b}{\partial y} - \frac{\partial a}{\partial y} \frac{\partial b}{\partial x} \quad (36)$$

Equations (33)-(35) describe the excitation and nonlinear evolution of compressible electromagnetic interchange modes in a finite beta plasma with inhomogeneous density and magnetic field. As one can see, the nonlinear terms in equations (33)-(35) are rather complicated. They contain so-called vector nonlinearities (represented through Poisson brackets) which are the source for generation of large scale vortex structures coexisting with short scale spectral components produced on the nonlinear stage of modulation instability of interchange modes.

5.2 Solution in the Form of a Double Vortex

In this section we will find the stationary solution of nonlinear system of equations (33)-(35) in the form of the double vortex. Such vortex structures are formed on the nonlinear stage of the interchange instability. Density perturbations associated with vortex structures are the cause of wave scattering for high frequency electromagnetic waves used for communications, sensing and OTH radar applications. Note that vortex structures produced by drift waves and described by the Hasegawa – Mima equation were described in [20- 21]. In [22] a procedure to obtain flute type vortex structures in a low beta plasma was analyzed. In order to obtain such a solution, we will rewrite equations (33)-(35) in the following dimensionless form:

$$\frac{d\delta n}{dt} = \frac{\tilde{\omega}_{ci}}{\tilde{\Omega}} \frac{\tilde{\rho}_s^2}{\tilde{L}^2} \frac{(\kappa_B - \kappa_N \beta/2)}{(1 + \beta/2)} \frac{d\delta n}{dy} - \frac{\tilde{\omega}_{ci}}{\tilde{\Omega}} \frac{\tilde{\rho}_s^2}{\tilde{L}^2} \frac{(\kappa_N + \kappa_B)}{(1 + \beta/2)} \frac{d\varphi}{dy} + \frac{\tilde{\omega}_{ci}}{\tilde{\Omega}} \frac{\tilde{\rho}_s^2}{\tilde{L}^2} \{\delta n, \varphi\} \quad (37)$$

$$\begin{aligned} \frac{d}{dt} \Delta \varphi = & \left(\tau \frac{\tilde{\omega}_{ci}}{\tilde{\Omega}} \frac{\tilde{\rho}_s^2}{\tilde{L}^2} \frac{(\kappa_N + \kappa_B)}{(1 + \beta/2)} \left(1 - \frac{\beta}{2} \right) + \frac{\tilde{\Omega}}{\tilde{\omega}_{ci}} g \right) \frac{d}{dy} \Delta \varphi + \\ & \frac{1}{\left(1 + \frac{\beta}{2} \right)} \left(\frac{\tilde{\Omega}}{\tilde{\omega}_{ci}} g \left(1 + \frac{\beta_{i+} + \beta_e}{2} + \frac{\beta^2}{4} \right) + \frac{\tilde{\omega}_{ci}}{\tilde{\Omega}} \frac{\tilde{\rho}_s^2}{\tilde{L}^2} \frac{\beta}{2\tau} \left(\kappa_B - \frac{\kappa_N \beta}{2} \right) \right) \frac{d}{dy} \Delta \delta n - \\ & \frac{\tilde{\Omega}}{\tilde{\omega}_{ci}} \frac{\tilde{\Delta}^2}{\tilde{\rho}_s^2} g \frac{d\delta n}{dy} + \frac{\tilde{\omega}_{ci}}{\tilde{\Omega}} \frac{\tilde{\rho}_s^2}{\tilde{L}^2} \{\Delta \varphi, \varphi\} + \tau \frac{\tilde{\omega}_{ci}}{\tilde{\Omega}} \frac{\tilde{\rho}_s^2}{\tilde{L}^2} \left(\{\Delta \delta n, \varphi\} + \left\{ \frac{d\delta n}{dx}, \frac{d\varphi}{dx} \right\} + \left\{ \frac{d\delta n}{dy}, \frac{d\varphi}{dy} \right\} \right) \end{aligned} \quad (38)$$

Where $\tilde{\rho}_s$ is the ion gyro radius, \tilde{L} is the fundamental distance scale length, $\tilde{\omega}_{ci}$ is the ion cyclotron frequency, $\tilde{\Omega}$ is the fundamental frequency, g is the external force, τ is the ratio of the electron temperature to the ion temperature, $\tilde{\Delta}$ is the Laplace operator, and all other variables are defined as usual but are in units normalized to the fundamental distance and frequency. The \sim implies un-normalized units.

Setting the fundamental distance scale length equal to the ion gyro radius and the fundamental frequency equal to the ion cyclotron frequency, the expressions simplifies to:

(5.7)

$$\begin{aligned} \frac{d\delta n}{dt} &= \frac{(\kappa_B - \kappa_N \beta/2)}{(1+\beta/2)} \frac{d\delta n}{dy} - \frac{(\kappa_N + \kappa_B)}{(1+\beta/2)} \frac{d\varphi}{dy} + \{\delta n, \varphi\}, \\ \frac{d}{dt} \Delta\varphi &= \left(\tau \frac{(\kappa_N + \kappa_B)(1-\beta/2)}{(1+\beta/2)} + g \right) \frac{d}{dy} \Delta\varphi + \frac{1}{(1+\beta/2)} \left(g(1 + \beta_i + \beta_e/2 + \beta^2/4) + \right. \\ &\quad \left. \frac{\beta}{2\tau} (\kappa_B - \kappa_N \beta/2) \right) \frac{d}{dy} \Delta\delta n - g \frac{d\delta n}{dy} + \{\Delta\varphi, \varphi\} + \tau \left(\{\Delta\delta n, \varphi\} + \left\{ \frac{d\delta n}{dx}, \frac{d\varphi}{dx} \right\} + \left\{ \frac{d\delta n}{dy}, \frac{d\varphi}{dy} \right\} \right). \end{aligned} \quad (39)$$

Introducing:

$$A_1 = \tau \frac{(\kappa_N + \kappa_B)(1-\beta/2)}{(1+\beta/2)} + g. \quad (40)$$

$$A_2 = \frac{1}{(1+\beta/2)} \left(g(1 + \beta_i + \beta_e/2 + \beta^2/4) + \frac{\beta}{\tau^2} (\kappa_B - \kappa_N \beta/2) \right). \quad (41)$$

$$A_3 = \frac{(\kappa_B - \kappa_N \beta/2)}{(1+\beta/2)}. \quad (42)$$

the equations can further be simplified to:

$$\frac{d\delta n}{dt} = A_3 \frac{d\delta n}{dy} - \frac{(\kappa_N + \kappa_B)}{(1+\beta/2)} \frac{d\varphi}{dy} + \{\delta n, \varphi\}. \quad (43)$$

$$\frac{d}{dt} \Delta\varphi = A_1 \frac{d}{dy} \Delta\varphi + A_2 \frac{d}{dy} \Delta\delta n - g \frac{d\delta n}{dy} + \{\Delta\varphi, \varphi\} + \tau \left(\{\Delta\delta n, \varphi\} + \left\{ \frac{d\delta n}{dx}, \frac{d\varphi}{dx} \right\} + \left\{ \frac{d\delta n}{dy}, \frac{d\varphi}{dy} \right\} \right). \quad (44)$$

In order to study the vortex structure that is a solution to these equations, it's convenient to describe the density and potential inside such a vortex in the following way:

$$\Delta\varphi = -b^2\varphi + f_1(x) = -b^2\varphi + F_1x. \quad (45)$$

$$\delta n = D\varphi + f_2(x) = D\varphi + F_2x. \quad (46)$$

And outside the vortex, a similar system of equations can be used:

$$\Delta\varphi = h^2\varphi. \quad (47)$$

$$\delta n = H\varphi. \quad (48)$$

Finally, we can move to the frame that is co-moving with the vortex.

$$y \rightarrow y' - Ut. \quad (49)$$

$$\frac{d}{dt} = -U \frac{d}{dy}. \quad (50)$$

These assumptions allow us to express the physics equations fully in terms of the potential:
(For $r < R_o$)

$$0 = (A_3 + U)D \frac{d\varphi}{dy} - \frac{(\kappa_N + \kappa_B)}{(1 + \beta/2)} \frac{d\varphi}{dy} + F_2 \frac{d\varphi}{dy}. \quad (51)$$

$$0 = (A_1 + U) \frac{d\Delta\varphi}{dy} + A_2 D \frac{d\Delta\varphi}{dy} - g \frac{d\delta n(\varphi)}{dy} + F_1 \frac{d\varphi}{dy} + \tau D F_1 \frac{d\varphi}{dy}. \quad (52)$$

And for $r > R_o$:

$$0 = (A_3 + U)H \frac{d\varphi}{dy} - \frac{(\kappa_N + \kappa_B)}{(1 + \beta/2)} \frac{d\varphi}{dy}. \quad (53)$$

$$0 = (A_1 + U) \frac{d\Delta\varphi}{dy} + A_2 H \frac{d\Delta\varphi}{dy} - g \frac{d\delta n(\varphi)}{dy}. \quad (54)$$

We now can begin solving for the parameters describing the vortex. The first parameter comes from solving (5.22):

$$H = \frac{(\kappa_N + \kappa_B)}{(U + A_3)(1 + \beta/2)}. \quad (55)$$

With that, we can derive the quantity h from (5.23):

$$h^2 = H \frac{g}{(U + A_1 + H A_2)} = \frac{(\kappa_N + \kappa_B)}{(U + A_3)(1 + \beta/2)(U + A_1 + H A_2)} g. \quad (56)$$

The solutions for inside the flute vortex are easily related to each other, but exact solutions require more constraints on the system. In the meantime, it is possible using (5.20) and (5.21) to solve the coefficients of the linear part of the vortex equations in terms of H and D :

$$\frac{b^2 \left((U + A_1) + D \left(A_2 + \frac{g}{b^2} \right) \right)}{(1 + \tau D)} = F_1. \quad (57)$$

$$(H - D)(U + A_3) = F_2. \quad (58)$$

It is easily noticed here that in the case where $D = H$, the density is proportional to the potential inside and outside the vortex. This particular solution is undesired as it is effectively the adiabatic case and allows for the electrons to have a Boltzmann distribution which is incompatible with flute modes.

The solutions to the vortex potential, assuming both the potential and the density perturbations go to zero at infinity and are finite at the origin, are of the form:

$$\varphi = \begin{cases} C_1 J_1(br) \cos\theta + \left(\frac{F_1}{b^2}\right) r \cos\theta, & r < R_o \\ C_2 K_1(hr) \cos\theta, & r > R_o \end{cases}. \quad (59)$$

Inserting this solution into the density equations yields:

$$\delta n = \begin{cases} DC_1 J_1(br) \cos\theta + \left(D\left(\frac{F_1}{b^2}\right) + F_2\right) r \cos\theta, & r < R_o \\ HC_2 K_1(hr) \cos\theta, & r > R_o \end{cases}. \quad (60)$$

Here the function J is the Bessel function of the first kind and K is the modified Bessel function of the second kind. It is reasonable to assume that the potential, density, and electric field are continuous over the boundary and that the electric field is smooth over the same.

$$\varphi_{in}(R_0) = \varphi_{ext}(R_0). \quad (61)$$

$$\frac{\partial \varphi_{in}}{\partial r} \Big|_{r=R_0} = \frac{\partial \varphi_{ext}}{\partial r} \Big|_{r=R_0}. \quad (62)$$

$$\frac{\partial^2 \varphi_{in}}{\partial r^2} \Big|_{r=R_0} = \frac{\partial^2 \varphi_{ext}}{\partial r^2} \Big|_{r=R_0}. \quad (63)$$

$$\delta n_{in}(R_0) = \delta n_{ext}(R_0). \quad (64)$$

These relations allow for solutions of the coefficients C_1 and C_2 :

$$C_1 = \frac{\rho_o R_o}{(D - H) J_1(bR_o)}. \quad (65)$$

$$C_2 = \frac{-F_2 R_o}{(D - H) K_1(hR_o)}. \quad (66)$$

$$\rho_o = -\frac{F_1}{b^2} (D - H) - F_2. \quad (67)$$

We can define the useful quantity \mathcal{E} as the ratio of ρ_o to F_2 . By using then the properties of the derivatives of the Bessel functions and using the continuity equations, we can solve \mathcal{E} to be:

$$-\frac{hK_2(hR_o)J_1(bR_o)}{bK_1(hR_o)J_2(bR_o)} = \frac{\rho_o}{F_2} = \mathcal{E}. \quad (68)$$

Combine this definition with the definitions of F_1 and F_2 and one can get the expression for D in terms of the physical parameters and the yet unknown term b.

$$\frac{((U+A_3)(\mathcal{E}+1)-U-A_1)}{A_2+\frac{g}{b^2}-\tau(U+A_3)(\mathcal{E}+1)} = D. \quad (69)$$

To determine b, we can make use of equation (63). This is analogous to setting:

$$-b^2\varphi + F_1R_0 = h^2\varphi. \quad (70)$$

Which leads to the alternative definition of \mathcal{E} :

$$\mathcal{E} = \frac{h^2}{b^2}. \quad (71)$$

Thus the quantity b is fully defined by the expression:

$$-\frac{K_2(hR_o)J_1(bR_o)}{K_1(hR_o)J_2(bR_o)} = \frac{h}{b}. \quad (72)$$

5.3 Generating Simulated Flute Vortices

A Matlab program was developed for the purpose of computing the coefficients of a flute vortex, given specific physical parameters. This program is used as a basis for the calculations performed in the next section. This section illustrates some of the general properties of flute vortices as described by the results of the previous section.

Equation (72) relating b, U, and R_o was used to complete the definition of the vortex. It was decided that both the most straightforward and physically intuitive choice for which variables to be assigned was U and R_o . As both of these represent easily observable physical quantities, namely vortex velocity and vortex radius, they are good choices. Also, the calculation of b values is computationally easier than computing U or R_o .

Newton's method, with line back searching, was used to determine b. One dimensional density and potential profiles for a particular vortex with R_o set to twenty Larmor radii, U set to 1% of the ion thermal velocity. The remaining primary physical parameters were:

$n_0 \sim 2 \times 10^5 \text{ cm}^{-3}$ - plasma density

$B_0 \sim 0.4 \text{ G}$ - magnetic field

$g \sim 500 \text{ cm/s}^2$ - gravitational constant

$T_i = T_e \sim 1.4 \text{ eV}$ - ion and electron temperature

$m_i = 16 \times m_p$ - ion mass and m_p - proton mass

It should be noted that there are many solutions in equation (72) for b for any particular set of physical parameters, and thus each solution for b effectively describes a different mode of the vortex solution. To demonstrate structural behavior for the different modes, radial profiles of a vortex with various values of b are shown in Figure 43-45. For a pure bimodal vortex, the lowest possible real value of b should be taken. The general mode behavior is that for larger b, the higher the number of local minima and maxima there are inside the vortex radius, but the smaller the amplitude of those oscillations relative to the linear radial behavior. There are exceptions to this general rule that may rule out the lowest mode. For very large b, the Bessel function term inside the vortex radius can effectively be ignored.

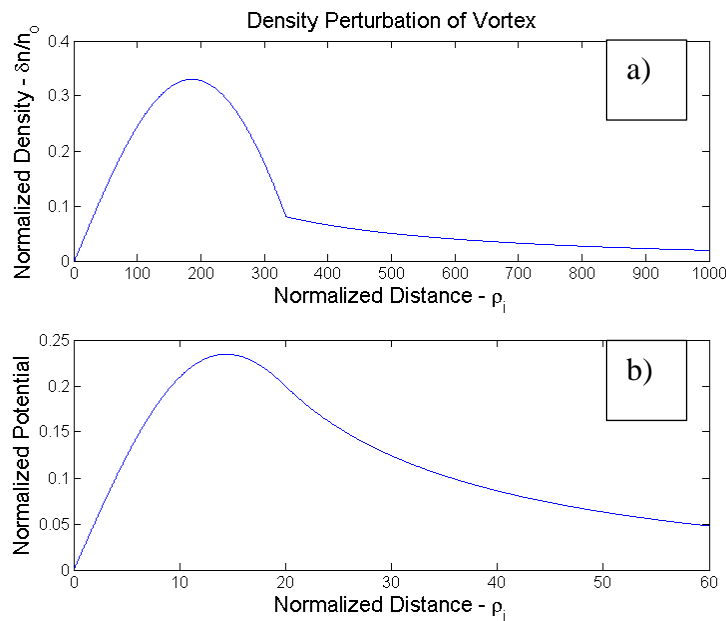


Figure 43: Density (a) and Potential (b) profile plots in the radial direction for a vortex with b value of 0.1439.

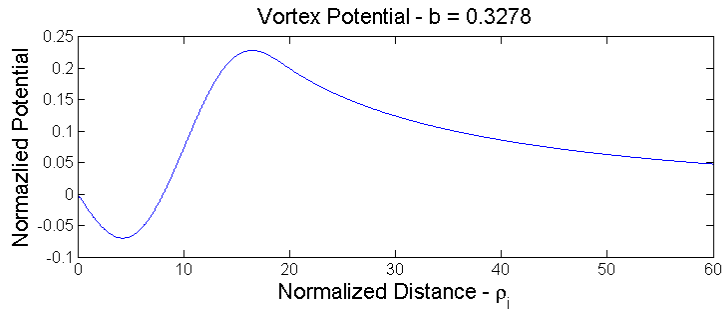


Figure 44: Potential profile for b of 0.3278.

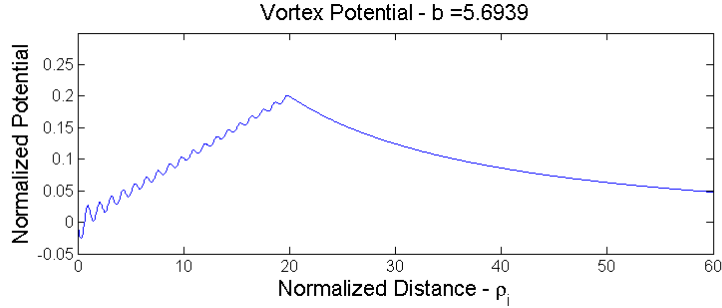


Figure 45: Potential profile for b of 5.6939. As can be seen, as b increases, the profile for $r < R_o$ is dominated by the linear component. For large b , H is nearly equal to D . As such, high b values are not fitting with the desired solution for the vortex quantities.

We can also plot contour maps of the density and potential perturbations. Potential contour maps are shown in Figure 46. In Figure 46, bimodal structure of the potential perturbations is obvious as is the increased number of nodes for the vortex with the larger b parameter.

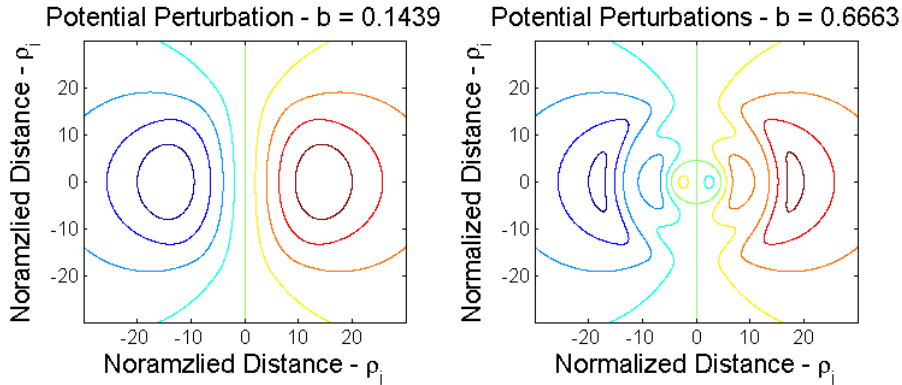


Figure 46: Two dimensional maps of the potential for b values of 0.1439 (left) and 0.6663 (right).

When varying the free parameters, it is necessary that the resulting vortex does not produce density perturbations equal to or larger than the background density. As such, there are parameters where this vortex model breaks down or doesn't apply. It is then important to verify that the vortex defined by a set of parameters is possible before trusting any product derived from those parameters. All vortices generated in this section and the next met this criteria.

5.4 High Frequency Electromagnetic Wave Scattering by Vortex Density Structures

In this section we will analyze scattering of high frequency electromagnetic waves from flute type double vortex structures generated on the nonlinear stage of interchange instability. As it was shown in section 5.2, flute type double vortex structures can be described by exact solutions of the system of two dimensional nonlinear equations (33) and (34). It is worth mentioning that scattering of electromagnetic waves by drift vortices was examined in [20] and [21]. Estimates for scattering by flute vortices [22-24] in a low beta plasma were given in [25].

Assume an incident high frequency electromagnetic plane wave in the form:

$$\mathbf{E}_i = E_i \mathbf{a}_i \sin(\mathbf{k}_0 \mathbf{r} - \omega_0 t). \quad (73)$$

In (5.42) \mathbf{a}_i is the unit polarization vector of the incident wave and \mathbf{k}_0 and ω_0 are the wave vector and frequency. Choosing the incident wave in the form of a plane wave implies that its width is much larger than the size of the vortex radius R_o .

In the co-moving frame, with speed U_0 , along the y-direction, the frequency and wave vector of an incident wave are:

$$\omega_i = \omega_0 - k_{0y} U_0 \quad \text{and} \quad \mathbf{k}_i = \mathbf{k}_0. \quad (74)$$

Defining scattering cross section as the ratio of the average scattered power (defined as the work done per unit time by the field created by the nonlinear current) to the energy flux of the incident EM signal for the scattering cross section we can write:

$$\sigma = \frac{\operatorname{Re}(P_{av})}{c \frac{|\mathbf{E}_i|^2}{8\pi}}. \quad (75)$$

In (5.44) P_{av} is averaged over time scattered power and we retain only the real part of it, and \mathbf{E}_i is the electric field of an incident wave. The spectrum of the scattered electromagnetic waves are defined as:

$$\mathbf{E}_{\mathbf{k}_\pm} = E_{\mathbf{k}_\pm} \mathbf{a}_\pm e^{i(\mathbf{k}_\pm \mathbf{r} - \omega_\pm t)}. \quad (76)$$

In (5.45) \mathbf{k}_\pm is the wave vector of the scattered wave and ω_\pm is its frequency. The scattered wave spectrum in fact consists of two parts $\mathbf{E}_{\mathbf{k}_+, \omega_+}$ and $\mathbf{E}_{\mathbf{k}_-, \omega_-}$, where:

$$\mathbf{k}_\pm = \mathbf{k}_i \pm \mathbf{q}. \quad (77)$$

$$\omega_\pm = \omega_0 \pm \omega_q. \quad (78)$$

In (5.46-47) \mathbf{q} is the wave vector from the spectrum of interchange modes and ω_q is the corresponding frequency. Following the procedure outlined in [18], [4], and [19] after lengthy but straightforward calculations the expression in cylindrical coordinates for the scattering cross section can be obtained:

$$\sigma_{\pm} = -\frac{9\omega_{pe}^4}{4\pi} \int Re \left(\frac{i \cos\left(\frac{\mu_{\pm}}{2} + \theta_0\right)}{\varepsilon^*(\mathbf{k}_{\pm}, \omega_{\pm}) \omega_i^4} \right) |I_1(k_{\pm}, k_i, \mu_{\pm}) + I_2(k_{\pm}, k_i, \mu_{\pm}) + I_3(k_{\pm}, k_i, \mu_{\pm})|^2 k_{\pm} dk_{\pm} d\mu_{\pm}. \quad (79)$$

where θ_0 is the angle of incidence of the incoming wave relative to the vortex alignment, μ_{\pm} is the angle between \mathbf{k}_i and \mathbf{k}_{\pm} , and I_1 , I_2 , and I_3 are given by:

$$I_1 = \frac{iDC_1R_o}{b^2 - q^2} (qJ_1(bR_o)J_0(qR_o) - bJ_0(bR_o)J_1(qR_o)). \quad (80)$$

$$I_2 = i \left(D \left(\frac{F_1}{b^2} \right) + F_2 \right) J_2(qR_o) \frac{R_o^2}{q} \quad (81)$$

$$I_3 = -\frac{iHC_2R_o}{h^2 + q^2} (qK_1(hR_o)J_2(qR_o) - hK_2(hR_o)J_1(qR_o)) \quad (82)$$

Below we will be interested in the case when scattered waves are plasma Eigen modes. In this case:

$$Re \left(\frac{-i}{\varepsilon'^*(\mathbf{k}_{\pm}, \omega_{\pm})} \right) = \pi \frac{\delta(\omega_{\pm} - \omega(\mathbf{k}_{\pm}))}{\left. \frac{\partial \varepsilon'_1}{\partial \omega} \right|_{\omega_{\pm} = \omega(\mathbf{k}_{\pm})}} \quad (83)$$

The frequency of interchange modes ω_q in (5.47) is very small in comparison with the frequency of an incident wave, i.e. $\omega_{k_0} \gg \omega_q$. This implies that for the scattered wave to be a plasma eigenmode ($\omega_{\pm} = \omega(\mathbf{k}_{\pm})$) the absolute value of the wave vector of a scattered wave should be of the order of the absolute value of the wave vector of an incident wave $|\mathbf{k}_{\pm}| \sim |\mathbf{k}_0|$. In other words, wave vectors in the spectrum of interchange modes which can efficiently scatter the incident wave should satisfy: $|\mathbf{q}| \leq 2|\mathbf{k}_0|$. In this case scattered waves will be plasma eigenmodes which can satisfy (5.52). As an example, in Figure 47 the spectral distribution of a normalized density of vortex structure as a function of the absolute value of the wavenumber $|\mathbf{q}|$ is presented and the arrow indicates the absolute value of the wavenumber $|\mathbf{k}_0|$ of an incident wave. In this particular example the part of the vortex spectrum with $|\mathbf{q}| \leq 0.266 \times 10^{-3} \text{ cm}^{-1}$ can effectively scatter incident electromagnetic wave with $|\mathbf{k}_0| \sim 0.133 \times 10^{-3} \text{ cm}^{-1}$ and the produced scattered electromagnetic waves will be plasma eigenmodes.

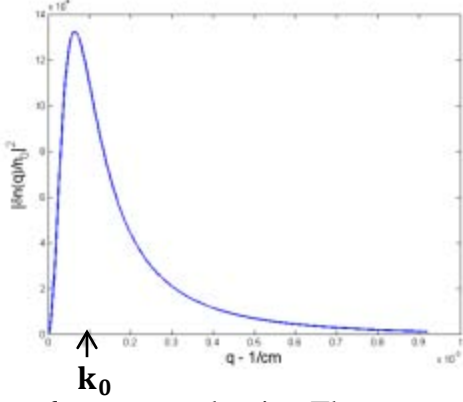


Figure 47: Fourier spectrum of the vortex density. The wave number, marked above, of the incoming wave with the frequency 1 GHz is $|\mathbf{k}_0| \sim 0.133 \times 10^{-3} \text{ cm}^{-1}$.

The total scattering cross section can be calculated as a function of the frequency of incident wave. Results are presented in Figure 48.

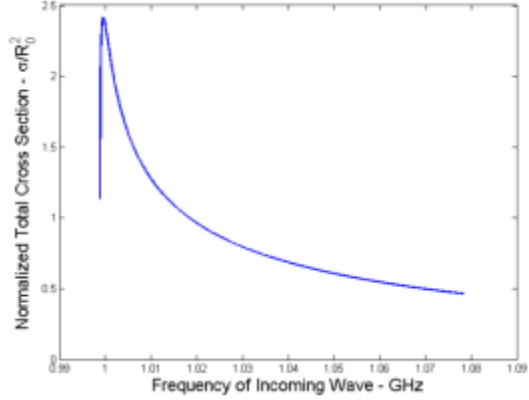


Figure 48: Calculated normalized cross section for a vortex with background density of $1.238 \times 10^{10} \text{ cm}^{-3}$, radius of 7.02 cm, velocity of 280.2 cm/s, and magnetic field of 715 G.

Next we present the differential scattering cross section in terms of scattering angle:

$$d\sigma_- = \frac{9\omega_{pe}^4 R_o^2}{8} \frac{1}{c^2} \frac{\cos^2 \alpha}{\omega_i^2} \left| \frac{DC_1}{b^2 - q^2} (qJ_1(bR_o)J_0(qR_o) - bJ_0(bR_o)J_1(qR_o)) + \right. \\ \left. + \left(D \left(\frac{F_1}{b^2} \right) + F_2 \right) \frac{J_2(qR_o)R_o}{q} - \frac{HC_2}{h^2 + q^2} (qK_1(hR_o)J_2(qR_o) - hK_2(hR_o)J_1(qR_o)) \right|^2 d\alpha \quad (84)$$

The results of such a calculation for plasma parameters listed below and a 1 GHz incoming wave are presented in Figure 49.

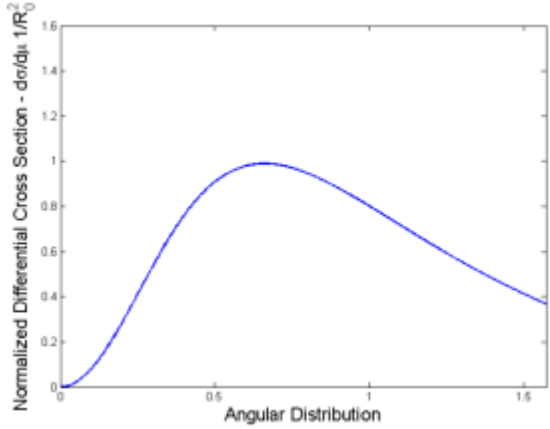


Figure 49: Expected differential cross section of a 1 Ghz wave from the analytic results in the case where the background plasma frequency is 0.998 GHz.

5.5 LSP Simulation Results

A series of simulations were performed in the LSP particle-in-cell plasma simulation suite using the analytic description of the flute vortex (equation (60)) as the basis for density perturbations to an otherwise uniform plasma. The physical parameters used in the simulations and in the Figure 49 were selected to be:

$$\begin{aligned}
 n_o &\sim 3.131 * 10^8 \text{ cm}^{-3} - \text{plasma density} \\
 B_0 &\sim 715 \text{ G} - \text{magnetic field} \\
 g &\sim 500 \text{ cm/s}^2 - \text{'gravitational' constant} \\
 T_e \sim T_i &= 0.026 \text{ eV} - \text{ion and electron temperature} \\
 m_i &= 16 * m_p - \text{ion mass}
 \end{aligned}$$

These are partially the same as ionospheric conditions. The scale length was normalized to an ion Larmor radius. To that end, the magnetic field was increased to reduce the Larmor radius and as a result overall size of the system is reduced. To keep the scale of the incoming wavelength similar to the vortex size, the input frequency of 1 GHz was used.

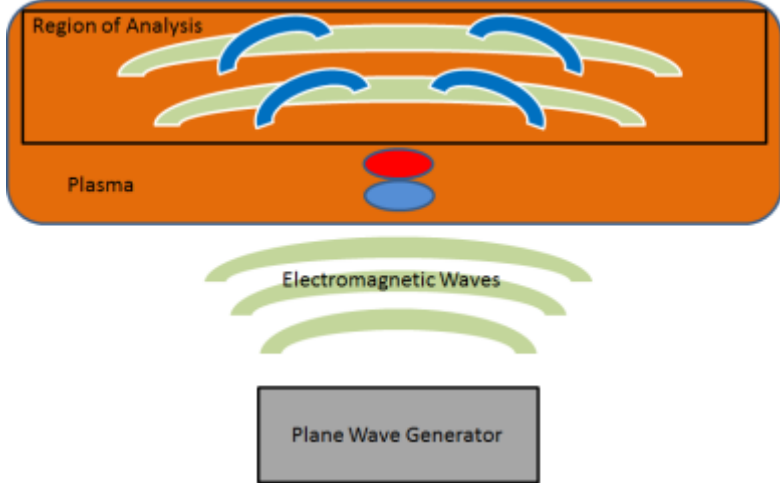


Figure 50: Diagram of LSP simulation. An electromagnetic plane wave is generated at the edge of the simulation (bottom) and propagates until it makes contact with the plasma. The wave travels through the plasma (orange), interacting with the vortex (red and blue) and produces scattered waves (blue arcs).

The simulation box was comprised of a 800 cm long, 1100 cm wide plasma and a 941 cm long plasma free region through which incoming electromagnetic waves were injected and allowed to propagate, generating an effective plane wave upon contact with the plasma. The peak variance from background for the vortex was 48%. The vortex had a characteristic radius of 7.02 cm, a velocity parameter of 280 cm/s, and it was located 45 cm from the edge of the plasma on the incoming wave side. The vortex as used in the simulation is shown in Figure 50.

A simulation with the same plasma parameters but without the vortex was also performed to provide a baseline. A time series Fourier analysis was performed on both simulations at each spatial location. The magnitude of the difference between the vortex and non-vortex simulation waves in Fourier space at 1 GHz was used to determine the effective scattering power at each location. Assuming the center of the vortex as the point of scattering, each location was assigned an angle relative to the direction of the unscattered waves. This allows for the determination of the angular scattering power profile (Figure 51) which can then be compared with the expected differential angular cross section (Figure 49). As the forward directed waves through a vortex will have less power compared to the non-vortex case, at small angles this procedure oversubtracts from the result. This may explain the sharper distribution in the simulations compared to the analytical results.

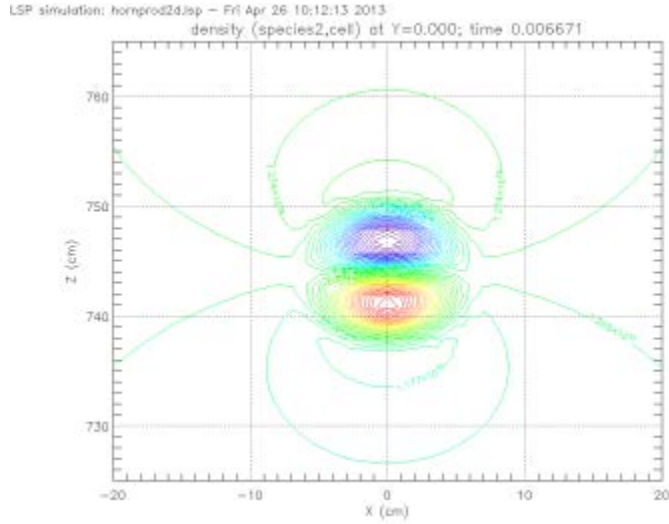


Figure 51: Density profile of vortex portion of simulation. The scattering cross section calculation and this density profile were generated using the same physical parameters.

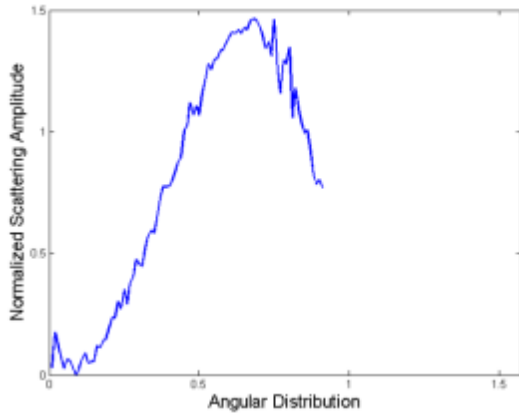


Figure 52: Normalized angular distribution of scattered wave output from LSP simulation of a 1 Ghz electromagnetic wave hitting a flute vortex. The physical parameters of these simulations were the same as those used for Figure 49.

As can be observed in Figure 49 and Figure 51, there is agreement between simulations and predictions for the general form of the angular scattering cross section, including nearly identical angles of maximum scattering. As with any simulation, there is numerical noise caused by the use of finite time and spatial steps and this is believed to be the cause of the noise on the simulated scattering profile. The profile is cut off for larger angles due to the finite size of the simulation hall, but such larger angles can be probed by producing a much wider simulation which has the trade off of requiring more time or computing resources. But despite that noise, the general scattering profile is very clear and meets the expectations of the analytic result. To our knowledge this is the first ever comparison of analytical and fully PIC kinetic simulations to determine the differential scattering cross section on vortex density structure in a magnetized plasma.

6.0 Additional Scattering Simulations: Ray Tracing

The objective of this portion of the research is to investigate and quantify the effect of flute vortex structures, large scale plasma irregularities which occur in the equatorial spread F-region, on high frequency electromagnetic propagation through the ionosphere. Such large scale irregularities impact long-range surveillance and communication in sometimes un-predictable ways. In the case in which the propagating frequency is high and thus the wavelength is small compared to the characteristic size of the density irregularities, the geometric ray tracing optics approximation is valid. When compared with full electromagnetic propagation equations, the Hamilton-Jacobi ray tracing approximation is a highly simplified approach which yields computationally efficient code and simulations.

In these simulations, flute type vortex structures in a low beta plasma are generated and used as the scattering medium for high frequency Hamilton-Jacobi ray tracing propagation. The code was written in C++ for Linux machines and outputs ASCII data files which are read and displayed via Matlab for simplicity.

6.1 Hamilton-Jacobi Ray Tracing approximation

The Hamilton-Jacobi ray tracing or geometric optics approximation is valid under the following assumption: the wavelength must be small in comparison to distance at which the index of refraction changes significantly, as shown in equation (85), where R_o is the characteristic scale length of a density perturbation. [20] In the case of high frequency radio waves propagating in the ionosphere, this may not necessarily be the case as electron densities often vary over short distances. However in the case of certain large ionospheric structures, such as the flute dipole vortex, this approximation becomes both valid and useful.

$$\lambda \ll R_o \quad (85)$$

In the most general form, the ray tracing equations which approximate propagation through an anisotropic dispersive plasma were formulated by S. Weinberg in 1962 [10], and are presented here absent the time dependent terms.

$$\frac{d\mathbf{r}}{dl} = \frac{\partial \omega}{\partial \mathbf{k}} , \quad \frac{d\mathbf{k}}{dl} = -\frac{\partial \omega}{\partial \mathbf{r}} \quad (86)$$

The localized dispersion relation for a homogenous plasma can easily be written as

$$\omega^2 = k^2 c^2 + \omega_{pe}^2(r) \quad (87)$$

More explicitly we can define

$$\omega_{pe}(r) = \frac{[n_o(1 + \delta N(r))]e^2}{m\epsilon_o} \quad (88)$$

Where the spatially dependent plasma frequency, $\omega_{pe}(r)$ is expressed in terms of the fractional perturbation from the background density, δN . In these terms, the dispersion relation for an ordinary wave is then

$$\omega^2 = k^2 c^2 + [\omega_{po} + \delta\omega_{pe}(r)]^2 \quad (89)$$

Where

$$\delta\omega_{pe}(r) = \frac{N_o \delta N(r) e^2}{m\epsilon_o} \quad (90)$$

Then substituting the above into equation (86) we get

$$\begin{aligned} \frac{d\mathbf{k}}{dl} &= -\frac{1}{c} \frac{\partial}{\partial \mathbf{r}} \left\{ \sqrt{k^2 c^2 + [\omega_{po} + \delta\omega_{pe}(r)]^2} \right\} \\ &= -\frac{1}{c} \frac{\omega_{pe(r)}^2 \frac{\partial}{\partial \mathbf{r}} \delta\omega_{pe}(r)}{\sqrt{k^2 c^2 + [\omega_{po} + \delta\omega_{pe}(r)]^2}} = -\frac{\omega_{po}^2 (1 + \delta N(r)) \frac{\partial \delta N(r)}{\partial \mathbf{r}}}{c\omega} \end{aligned} \quad (91)$$

And for $\frac{d\mathbf{r}}{dl}$ we have

$$\frac{d\mathbf{r}}{dl} = \frac{\partial}{\partial \mathbf{k}} \left\{ \sqrt{k^2 c^2 + [\omega_{po} + \delta\omega_{pe}(r)]^2} \right\} = \frac{c\mathbf{k}}{\omega} \quad (92)$$

We can now write a full system of equations for describing this high frequency ray tracing approximation, in six-dimensional phase space the equations (91-92) become

$$\begin{aligned} \frac{dx}{dl} &= \frac{c}{\omega} k_x & \frac{dk_x}{dl} &= -\frac{\omega_{po}^2 (1 + \delta N(r)) \frac{\partial \delta N(r)}{\partial x}}{c\omega} \\ \frac{dx}{dl} &= \frac{c}{\omega} k_x & \frac{dk_y}{dl} &= -\frac{\omega_{po}^2 (1 + \delta N(r)) \frac{\partial \delta N(r)}{\partial y}}{c\omega} \\ \frac{dx}{dl} &= \frac{c}{\omega} k_x & \frac{dk_z}{dl} &= -\frac{\omega_{po}^2 (1 + \delta N(r)) \frac{\partial \delta N(r)}{\partial z}}{c\omega} \end{aligned} \quad (93)$$

These 6 coupled ordinary differential equations can be solved easily numerically; in our case we applied a fourth order Runge-Kutta algorithm. The simulation is initialized by setting

$$|\mathbf{k}| = \frac{\sqrt{\omega^2 - \omega_{pe}^2}}{c} \quad (94)$$

While the initial values for x, y, z as well as the initial direction of \mathbf{k} are left as input parameters.

6.2 Analytical Solution to Flute-Type Density Structures

The derivation of the following solution, which describes density perturbations for double vortex structures, is lengthy and was detailed in the previous section regarding interchange instabilities. In brief, a stationary solution to a system of nonlinear equations describing the interchange modes in finite beta plasmas was found in terms of the spatially dependent density perturbation, δN . The general assumptions made in this procedure are as follows: 1) The flute modes have frequency such that $\omega \ll \Omega_i$, where $\Omega_i = ZeB_{0z}/m_i c$ is the ion cyclotron frequency. 2) The coordinate system is set such that the perturbations and oscillations are uniform along the magnetic field lines. 3) The quasi-neutrality condition is assumed in which $N_e = ZN_i$. For the particular case as described above, the density perturbation function, $\delta N(r, \theta)$ is given (95). [11]

$$\delta N = \begin{cases} DC_1 J_1(br) \cos\theta + \left(D\left(\frac{F_1}{b^2}\right) + F_2\right) r \cos\theta, & r < R_o \\ HC_2 K_1(hr) \cos\theta, & r > R_o \end{cases} \quad (95)$$

Here r and θ are in a plane perpendicular to the magnetic field, b and h describe the vortex mode internally and externally, respectfully, and are related by the boundary condition, $r = R_o$ by

$$\frac{K_2(hR_0)J_1(bR_0)}{K_1(hR_0)J_2(bR_0)} = -\frac{h}{b} \quad (96)$$

where

$$h^2 = \frac{(\kappa_N + \kappa_B)}{(U + A_3)(1 + \beta/2)(U + A_1 + HA_2)} g. \quad (97)$$

The remainder of constants, defined in order to simplify the expression, in equation (95): H, D, C_1, C_2, F_1 and F_2 are composed of standard plasma parameters as well as b, h, R_o , and U , which is the drift or co-moving velocity. Thus, the only unknown in equation (95), is the internal flute mode, b , which we must solve for using the boundary condition, equation (96) and the definition of h in equation (97). This is accomplished by graphically solving equation (96) and selecting a flute mode

which is closest to our best guess (judged from literature). This explicit approach isn't computationally efficient, however, because our parameters will not be varying beyond a handful of desired cases, it is a simple matter to compute all of the solutions and store flute mode values for repeated computations.

As an example, the flute vortex generating code was used with the following input parameters to generate the example density perturbation map shown in **Table 2.**

Physical Vortex Parameters	
Background Density	$n_{0e} = n_{oi} = 4 \times 10^6 \text{ cm}^{-3}$
Magnetic Field	$B_0 = 0.3 \text{ G}$
Acceleration	$g = 500 \text{ cm/s}^2$
Atomic Mass	16 amu
Temperature	$T_e = T_i = 0.026 \text{ eV}$
Density Scale Length	$\kappa_N = 1/300000 \text{ cm}^{-1}$
Velocity	$U = 2.7 \text{ cm/s}$
Characteristic Radius	$R_0 = 2200 \text{ cm}$
Vortex Mode (Normalized)	$b = 0.05034$ (<i>guess</i> = 0.4945)

Table 2: Flute vortex input parameters for density perturbation shown in figure below.

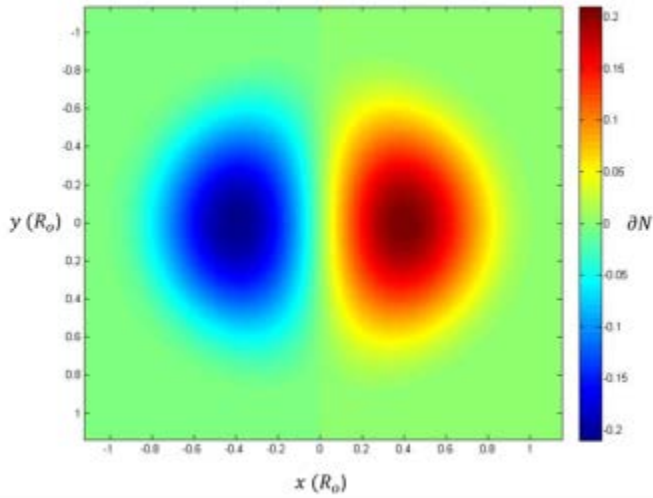


Figure 53: Example of ionospheric flute vortex density perturbation

6.3 Integration of Ray Tracing Algorithm with Vortex Solutions

In attempt to model more realistic atmospheric conditions, it is desired to study scattering and diffusion through multiple, randomly located vortex structures. As such an algorithm was developed to iteratively generate the structures discussed in the previous section and randomly place the structures in a density map. The algorithm accepts a tolerance for how close each structure can be placed to one another based on each structures characteristic radius, which can also be a random value for each structure. Below in Figure 55 and Figure 54 there are two examples of the iteratively generated density maps each with a different separation tolerance.

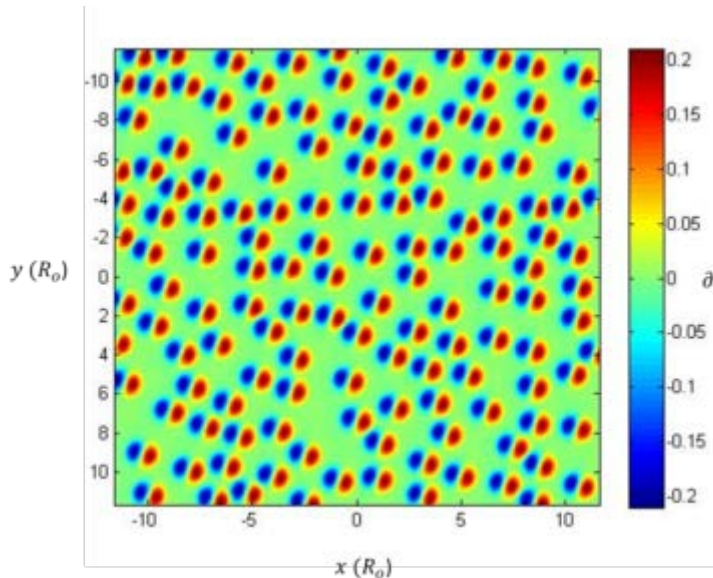


Figure 55: Iteratively placed flute vortex field having high separation tolerance

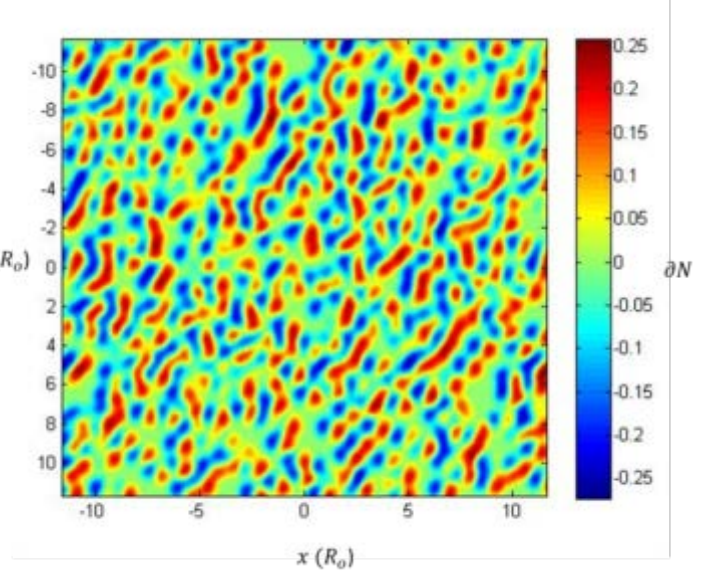


Figure 54: Iteratively placed flute vortex field having low percentage radius separation tolerance.

To

make this density distribution three dimensional we simply extend this distribution so that it is uniform in the Z direction (parallel to magnetic field lines). Now, introducing our ray tracing algorithm and using density fields as presented above, we can simulate high frequency scatter through such density structures. A buffer is placed on both the entrance and exit side of the simulation box in order to allow for accurate measurement of initial and final ray vectors.

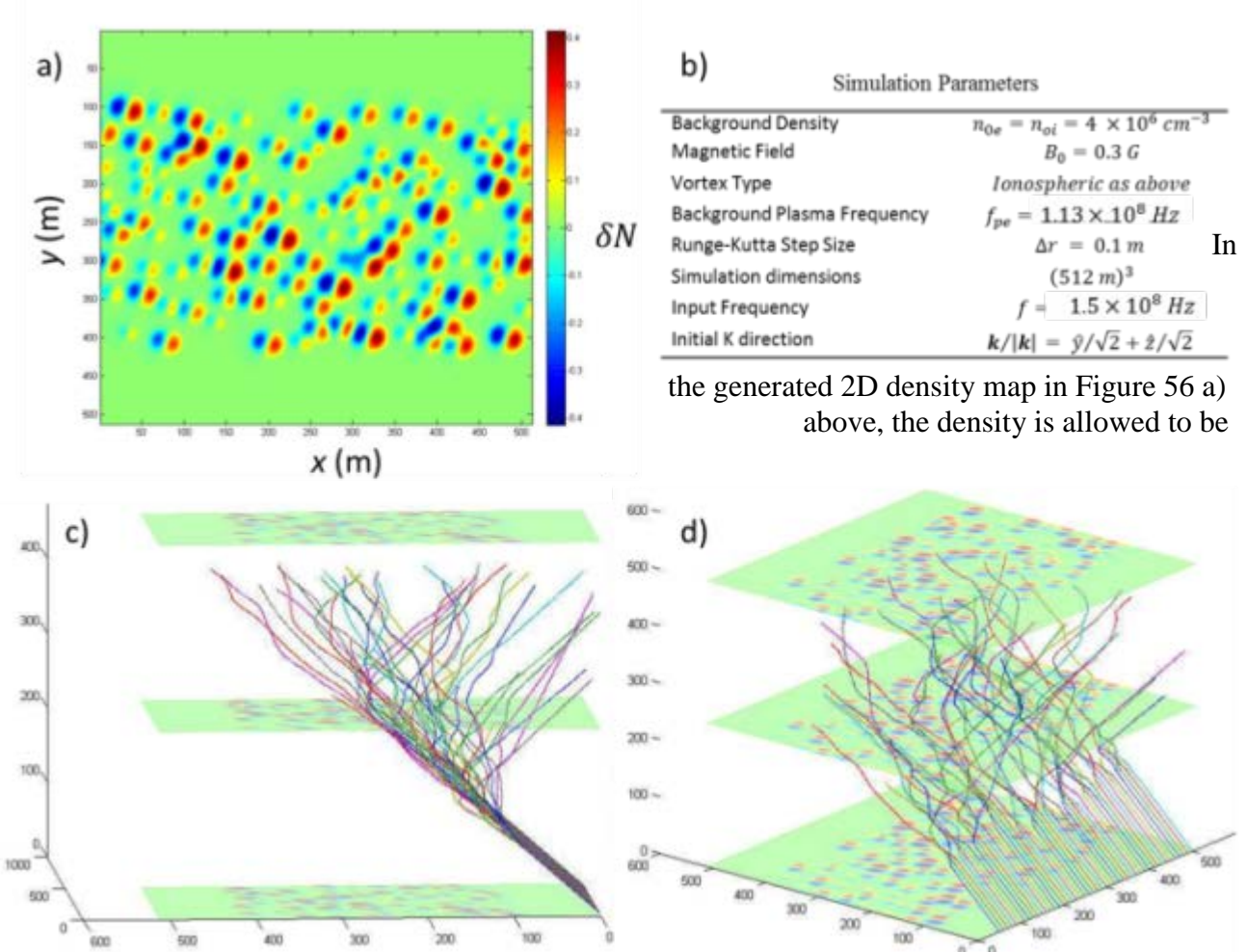


Figure 56: a) Generated 2D density map, b) simulation parameters, c) 3D line plots of ray tracing predominately in the y - z plane with slices of the density map superimposed, d) 3D line plot of the same data rotated so that it is approximately isometric.

uniform near the y boundaries so that the rays may propagate linearly before and after interaction with the density perturbations. This is to aid post-processing, for instances it enables the calculation of the total angle of deviation. However, it is obvious from c) and d) that we need to extend our simulation box so that the rays can propagate in homogenous space both before and after interaction with the perturbations. In addition to the homogenous boundaries, we have added randomly sized flute vortices. As the density map is iteratively created, the vortex characteristic radius, R_o , is randomly generated within some range. For this particular simulation the vortex radius was randomly generated between 16 and 28 meters. Figure 56 c) and d) show the ray propagation, with initial k vectors propagation at 45 degrees in the y - z plane. Superimposed on the 3D line plots are

slices in the x-y plane at 3 z locations. Again, the density perturbations are constant in the z direction.

6.4 Fokker-Planck description of Diffusion, Future Work

Due to the random, stochastic nature of the scattering simulated in this study, it is useful to describe the phenomenon in a statistical context. For this purpose let us consider a ray which encounters a random density perturbation and is subsequently scattered some angle α . Because this process can be approximated as a Markovian process, that is the time evolution of α is only dependent upon the current or previous state, we can model it's evolution using the Fokker-Planck equation. [22] [23] Additionally, the Fokker-Planck equation assumes a Markov process whose individual steps are small. In the most general form the Fokker-Planck equation is a second order differential equation given by [13]

$$\frac{\partial P(y, t)}{\partial t} = -\frac{\partial}{\partial y} A(y) + \frac{1}{2} \frac{\partial^2}{\partial y^2} B(y)P \quad (98)$$

The first term on the right hand side of equation (98) is known as the “drift” or “friction” term while the second term is the “diffusion” term. To model the total deflection of a ray encountering randomly located scatterers, y becomes or final angle of deflection, α . For a small Δt , by definition the two coefficients are then given by

$$A(\alpha) = \frac{\langle \Delta \alpha \rangle}{\Delta t}, \quad B(\alpha) = \frac{\langle (\Delta \alpha)^2 \rangle}{\Delta t} \quad (99)$$

In which the scattering is defined in the following coordinate system, for one scatterer

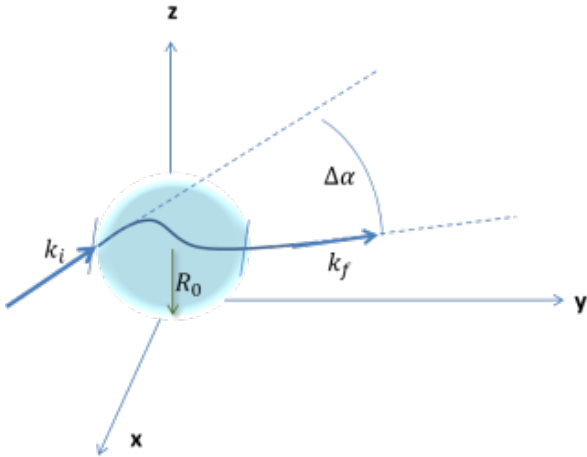


Figure 57: Scatter geometry for Fokker-Planck approximation

It is fair to assume that the ray scattering process will be symmetric, $\langle \Delta\alpha \rangle = 0$ and then the friction term vanishes leaving [13] [12]

$$\frac{\partial P(\alpha, t)}{\partial t} = \frac{\langle (\Delta\alpha)^2 \rangle}{2\Delta t} \frac{\partial^2}{\partial \alpha^2} P. \quad (100)$$

This simple result in the above equation is the starting point for our future work. Because the diffusion term is proportional to $\langle (\Delta\alpha)^2 \rangle$, it can be determined from our numerical ray tracing results. Additionally, this diffusion coefficient could be determined analytical using a method similar to that of Hizanidis et al 2010 [14]. Then, a solution to the Fokker-Planck equation can be found using both the analytical and numerically derived diffusion coefficient. This process and comparison is detailed by the flow diagram in the Figure 58.

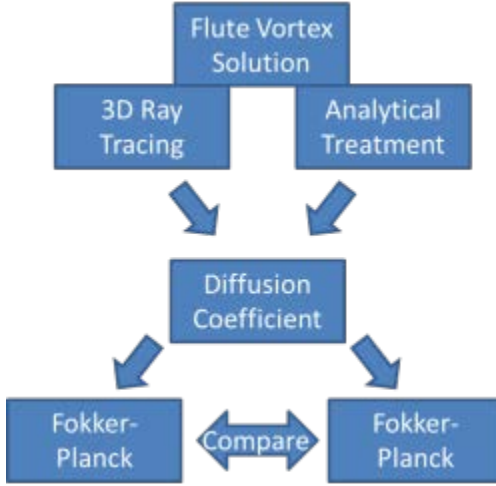


Figure 58: Fokker-Planck comparison; future work.

This process would enable us to verify accuracy and validity of the 3D ray tracing code in calculating the overall beam diffusion through such media. Once validated, we could use this simple ray tracing code to describe the propagation of high frequency waves through any type of plasma media in that follows the assumption that $\lambda \ll R_o$.

7.0 Scattering Simulations: Particle in Cell

In the AFOSR FY13 report, an analytic, stationary solution to the Flute type density irregularities was derived. This derivation was also published in reference [21] and is shown for completeness in Section 5. In the FY13 report and reference [21], the numerically calculated cross section due to Flute vortex structures was calculated using LSP (a fully kinetic particle-in-cell simulation). A comparison was made between the differential cross-section calculated from LSP (Fig. 10 in Reference [21]) and the analytic cross-section (Fig. 11 in Reference [2]) using parameters appropriate for high energy density physics. In order to further validate the analytic calculation, comparisons have been made between LSP and theory using ionospheric parameters, which are summarized in Table 3 below. For the LSP simulations, the simulation domain is established in the x-z plane with $\Delta x = \Delta z = 10$ cm, $L_x \times L_z = 10000$ cm $\times 22000$ cm, and $\Delta t = 0.23$ ns, which satisfies the CFL condition for light waves. The total number of macro-particles used in the simulation is $\sim 8 \times 10^7$. The simulation uses PML boundary conditions to dampen reflections of the EM waves at the boundaries. A vacuum layer is established around the edge of the simulation domain to keep the plasma particles from interacting with the PML layer. Because the plasma is quite cold, all particles remain in the simulation domain during the time that the simulation is run.

Plasma density	n_o	$4 \times 10^6 \text{ cm}^{-3}$
Magnetic Field	B_o	0.3 G
Acceleration	g	500 cm/s ²
Ion mass	M_i	16 AMU
Temperature	$T_i = T_e$	0.026 eV
Density scale length	κ_N	$1/3 \times 10^{-5} \text{ cm}^{-1}$
Characteristic Radius	R_o	2200 cm
Vortex Mode	b	0.4945
Input Frequency	f_o	35.9 MHz
Velocity	U	-2.4 cm/s

Table 3: Ionospheric plasma parameters used for generating Flute vortex structure shown in the figure below

The fluid solution to the Flute vortex structure (Equations 23-26 in Reference [21]) contains many solutions due to the variety of modes that exist involving the Bessel functions in the final general solution. The “Vortex Mode” shown in the table above is the lowest order mode and has the fewest oscillations in the Bessel function solution. The “Vortex Mode” is found via equation (27) in Reference [21], which is solved via The Bisection Method [25] using a Matlab function called “fzero”. The perturbed density (δn) and the potential (ϕ) due to the Flute Vortex structure using the parameters in the Table 1 are shown in Figure 59. The perturbed density is then embedded into an ambient plasma which has a background density given by n_o in the above table. The entire simulation domain with the Flute vortex structure is shown in Figure 60.

The scattering cross section is calculated by launching a TE wave-guide with a polarization in the y-direction, a k-vector in the z-direction and frequency given by f_o in Table 3. Note that the simulation domain is established in the x-z plane. The wave is launched at the $z = 0$ boundary as indicated by the arrows in Figure 60. Two simulations were performed with the exact same simulation setup and plasma parameters, except that one simulation contains the

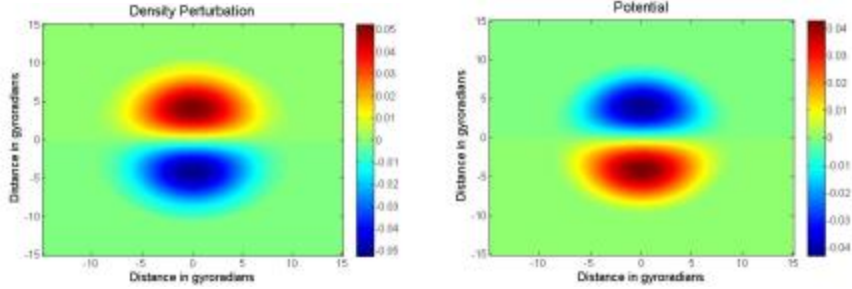


Figure 59: Perturbed Density (left) and the potential (right) of a Flute vortex structure using plasma parameters shown in the table above.

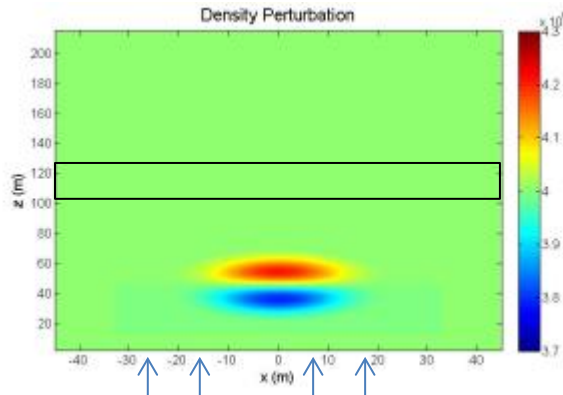


Figure 60: Total density profile imbedded in the ambient ionospheric plasma.

The arrows represent the TE wave guide which is launched through the $z = 0$ boundary. The black box indicates the region in which the differential cross-section is calculated.

Flute vortex and the other contains only the ambient plasma. To calculate the angular properties of the scattering cross section, a temporal FFT of E_y at each spatial grid point is performed in a region beyond the vortex. At each grid point, the FFT from the two simulations is then subtracted at f_0 and the magnitude of the differenced FFT is calculated. The result of the differenced FFT is binned by angle relative to the vortex center. The region in which the cross-section is calculated is shown by the rectangular box in Figure 60. The binned FFT is compared with the theoretical result, which is given by Equation (45) in Reference [21]. The results of this calculation is shown below in Figure 61, which is also shown in Figure (6.12) in Reference [21]. The left panel shows the differential cross-section from theory and the right panel shows the differential cross-section from LSP. Excellent agreement is found in the angle at which the differential cross-section peaks.

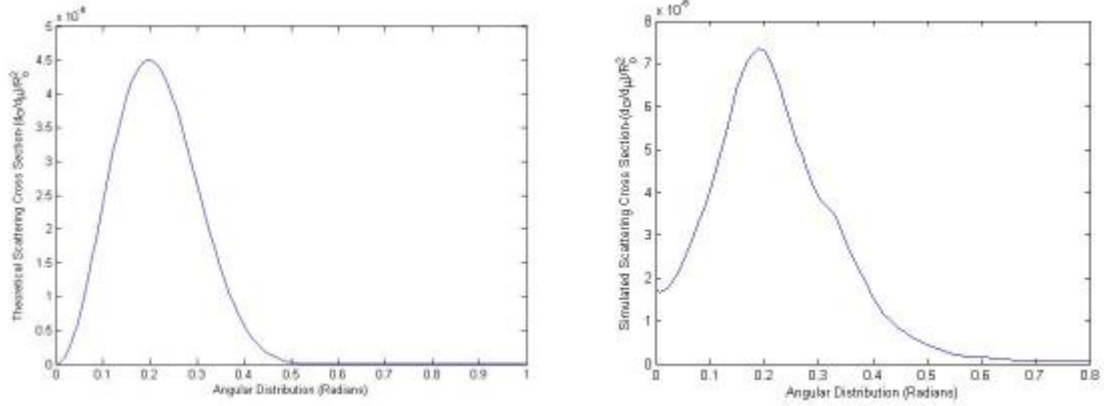


Figure 61: Theoretical (left) and numerically calculated (right) differential cross section due to the Flute vortex structure shown in Figure 2. Note that the y-axis values are multiplied by 10^{-6} in both plots.

We have also performed other simulations involving analytically calculated Flute vortex structures but with the density structure rotated. Shown below is an example of one such structure with the density profile rotated by 90° (left panel) and 45° (right panel). The rotated density structures are intended to mimic an incoming EM wave in a direction different than the one shown in Figure 60. In both cases, the density structures are imbedded in the same ambient plasma as shown in Figure 60 and a TE wave is launched from the $z = 0$ boundary.

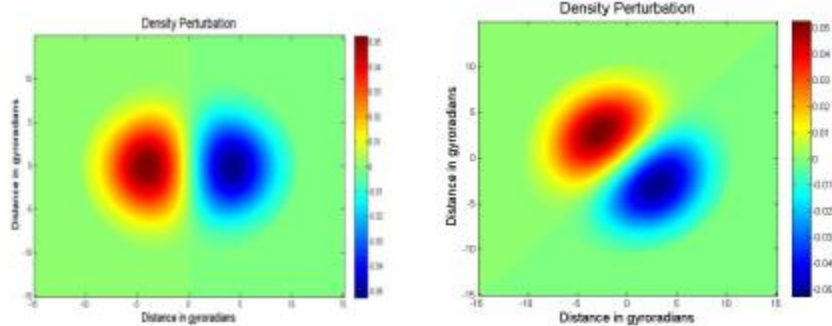


Figure 62: Flute vortex structures used to calculate the differential cross section shown in Figure 6.5. All plasma parameters are identical to Figure 60 as is the size of the simulation domain, cell size and time step.

The differential cross sections calculated from LSP for the two rotated vortex structures are shown in Figure 63. The peak in the differential cross section occurs at a similar angle to the vortex structure shown in Figure 60: Total density profile imbedded in the ambient ionospheric plasma.. However, in the rotated case, the curve is broader at $\theta \sim 0.2$ radians, and the curve is symmetric about $\theta=0$. Nevertheless, the peaks of the differential cross-sections are centered about $\theta \sim \pm 0.2$ radians. For negative angles, there is a minimum at -0.2 radians with peaks on both sides. Figure 60 and Figure 63 seem to indicate that the differential cross section is nearly independent of the angle in which the EM wave is launched through the Flute vortex structure. Furthermore the amplitude of the differential cross section due to the rotated vortex structures is nearly identical to non-rotated case.

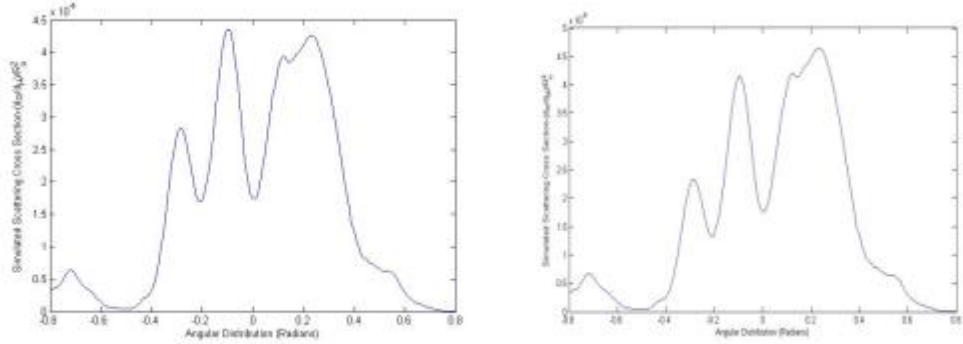


Figure 63: (Left) Differential cross section due to the Flute structure shown the left panel of Figure 62. (Right) Differential cross section due to the Flute structure shown in the right panel of Figure 62.

We have also calculated the differential cross section due to Flute vortex structure that has $\delta n \approx 15\%$. In order to generate a larger density perturbation, we set the acceleration term (g) to 450 cm/s^2 . All other parameters are the same as Table 3. The calculated differential cross section is shown in Figure 64: Differential cross section due to Flute vortex structure with $\delta n = 15\%$.

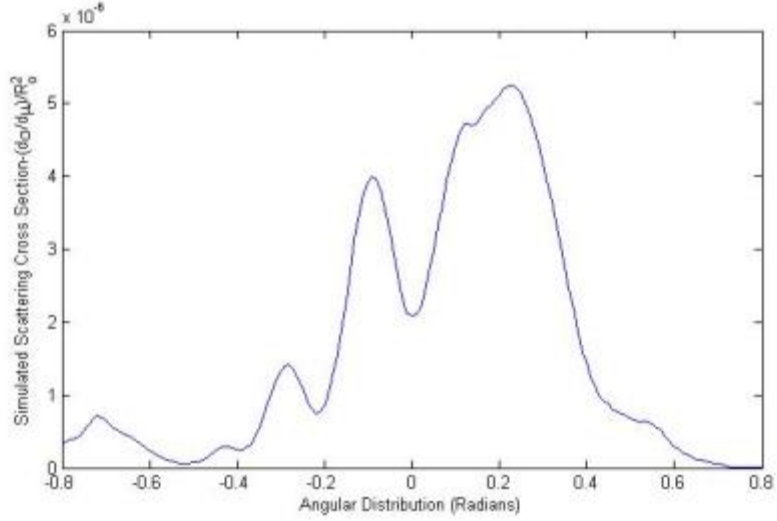


Figure 64: Differential cross section due to Flute vortex structure with $\delta n = 15\%$.

Significant scattering occurs at ~ 0.2 radians with significant scattering also occurring up to 0.6 radians, indicating that scattering occurs at larger angles for larger density perturbations.

We have also calculated the differential cross section due to a numerically calculated Flute-type structure. The density perturbations are calculated using a numerical algorithm called FLUTE [26]. The perturbation is then input into LSP and scattering is calculated off of this density perturbation. Figure 63 shows the density perturbation from FLUTE which is input into LSP. Note that the boundary conditions in FLUTE are periodic which is evident from the density profile.

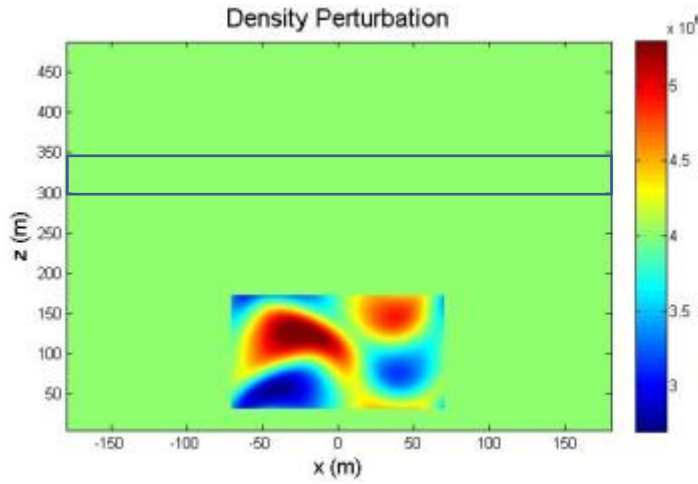


Figure 65: Initial density profile input into LSP. The density profile is calculated in a numerical program called FLUTE.

The simulation grid size is $L_x \times L_z = 40000 \text{ cm} \times 50000 \text{ cm}$, resulting in a larger simulation domain because we continue to set $\Delta x = \Delta z = 10 \text{ cm}$. The number of macro-particles used is $\sim 3.5 \times 10^8$. The differential cross section is calculated in the rectangular box shown in Figure 63. The peak density perturbation is $\sim 35\%$, which is significantly larger than the analytically calculated Vortex structure shown in Figure 59 and Figure 60. The differential cross section is shown in Figure 65. Notice that now significant scatter occurs at ~ 0 radians and extends out to ~ -0.6 radians. Furthermore, the magnitude of the differential cross section is ~ 10 times greater than the analytic vortex structures.

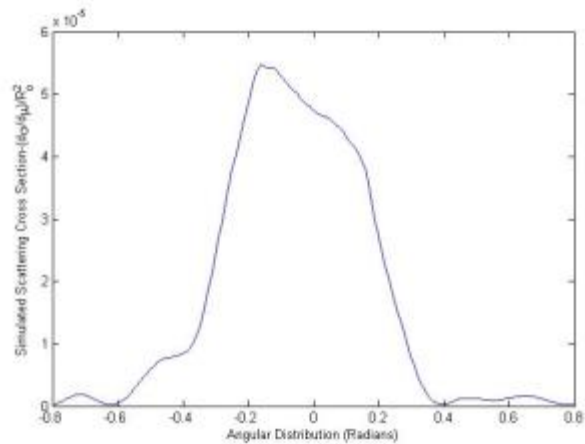


Figure 66: Differential cross section due to the numerically calculated vortex structure shown in Figure 63.

References

- [1] W. E. Amatucci, M. E. Koepke, J. J. Carroll III and T. E. Sheridan, "Observations of ion-cyclotron turbulence at small values of magnetic-field-aligned current.,," *Geophys. Res. Lett.*, p. 21(15):1595, 1995.
- [2] W. E. Amatucci, D. N. Walker, G. Ganguli, J. A. Antoniades, D. Duncan, J. H. Bowles, V. Gavirshchaka and M. E. Koepke, "Plasma response to strongly sheared flow.,," *Phys. Rev. Lett.*, p. 77(10):1978, 1996.
- [3] G. Ganguli, M. J. Keskinen, H. Romero, R. Heelis, T. Moore and C. Pollock, "Coupling of microprocesses and macroprocesses due to velocity shear: An application to the low-altitude ionosphere," *J. Geophys. Res.*, p. 99(A5):8873, 1994.
- [4] G. Ganguli, Y. C. Lee and P. J. Palmadesso, "Kinetic theory for electrostatic waves due to transverse velocity shears.,," *Phys. Fluids*, p. 31(4):823, 1988.
- [5] G. Ganguli, Y. C. Lee and P. P, "Electrostatic ion-cyclotron instability caused by a nonuniform electric field perpendicular to the external magnetic field," *Phys. Fluids*, p. 28(3):761, 1985.
- [6] G. Ganguli, Y. C. Lee and P. Palmadesso, "Electron-ion hybrid mode due to transverse velocity shear," *Phys. Fluids*, p. 31(10):2753, 1988.
- [7] M. E. Koepke, W. E. Amatucci, J. J. Carroll III, V. Gavirshchaka and G. Ganguli, "Velocity-shear-induced ion-cyclotron turbulence: Laboratory identification and space applications," *Phys. Plasmas*, p. 2(6):2523, 1995.
- [8] M. E. Koepke, W. E. Amatucci, J. J. Carroll II and T. E. Sheridan, "Experimental verification of the inhomogeneous energy-density driven instability," *Phys. Rev. Lett.*, p. 72(21):3355, 1994.
- [9] K. I. Nishikawa, G. Ganguli, Y. C. Lee and P. J. Palmadesso, "Simulation of ion-cyclotron-like modes in a magnetoplasma with transverse inhomogeneous electric field," *Phys. Fluids*, p. 31(6):1568, 1988.
- [10] J. R. Penano and G. Ganguli, "Generation of electromagnetic ion cyclotron waves in the ionosphere by localized transverse dc electric fields," *J. Geophys. Res.*, p. 107(A8):1189, 2002.
- [11] J. R. Penano and G. Ganguli, "Generation of elf electromagnetic waves in the ionosphere by localized transverse dc electric fields: Subcyclotron frequency regime," *J. Geophys. Res.*, p. 105(A4):7441, 2000.
- [12] J. R. Penano and G. Ganguli, "Ionospheric source for low-frequency broadband electromagnetic signatures," *Phys. Rev. Lett.*, p. 83(7):1343, 1999.

- [13] J. R. Penano, G. Ganguli, W. E. Amatucci, D. N. Walker and V. Gavrishchaka, "Velocity shear-driven instabilities in a rotating plasma," *Phys. Plasmas*, p. 5(12):4377, 1998.
- [14] V. Sotnikov, T. Kim, E. Mishin, W. E. Amatucci, G. Ganguli, E. Tejero, T. A. Mehlhorn and I. Paraschiv, "Low frequency plasma turbulence as a source of clutter in surveillance and communication," in *AMOS 2012 Conference*, 2012.
- [15] H. Romero and G. Ganguli, "Nonlinear evolution of a strongly sheared cross-field plasma flow," *Phys. Fluids B*, p. 5(9):3163, 1993.
- [16] V. E. Zakharov, "Collapse of Langmuir waves.," *Sov. Phys. JETP*, pp. 908-914, 1972.
- [17] S. L. Musher and B. I. Sturman, "On the collapse of plasma waves near the low-hybrid resonance," *Pisma Zh. Eksp. Teor.*, pp. 22, 537, 1975.
- [18] V. Sotnikov, V. D. Shapiro and V. I. Shevchenko, "Macroscopic consequences of collapse at the lower hybrid resonance," *Sov. J. Plasma Phys*, p. 4(2):252, 1978.
- [19] V. D. Shapiro, V. I. Shevchenko, G. I. Solovev, V. P. Kalini, R. Bingham, R. Z. Sagdeev, M. Ashour-Abdalla, J. Dawson and J. J. Su, "Wave collapse at the lower-hybrid resonance," *Phys. Fluids B*, p. 5:3148, 1993.
- [20] T. H. Stix, *The Theory of Plasma Waves*, New York: McGraw-Hill, 1962.
- [21] V. Sotnikov, T. Kim, J. Lundberg, I. Paraschiv and T. A. Melhorn, "Scattering of electromagnetic waves by vortex density structures associated with interchange instability: Analytical and large scale plasma simulation results," *Physics of Plasmas*, no. 21, 2014.
- [22] C. Tsironis, A. G. Peeters, H. Isliker, D. Strintzi, I. Chatziantonaki and L. Vlahos, "Electron-cyclotron wave scattering by edge density fluctuations in ITER," *Physics of Plasmas*, vol. 16, 2009.
- [23] N. G. V. Kampen, *Stochastic Processes in Physics and Chemistry*, Hungary: Elsevier BV., 2007.
- [24] K. Hizanidis, "Fokker-Planck description of the scattering of radio frequency waves at the plasma edge," *Physics of Plasmas*, vol. 17, p. 022505, 2010.
- [25] R. Burden and D. Faires, *Numerical Analysis*, Brooks/Cole, 2001.
- [26] V. I. Sotnikov, V. V. Ivanov, R. Presura, E. Yassin, J. Kindel, J. N. Leboeuf, O. G. Onishchenko, B. V. Oliver, B. Jones, T. A. Mehlhorn and C. Deeney, "Investigation of flute instability in application to laboratory astrophysics and Z-pinch experiments," *Astrophys. Space Sci.*, pp. 209-213, 2009.

Appendix A: In house Activities

Publications in Peer Reviewed Journals, Books, etc:

1. V.I. Sotnikov, R.W. Deming, L. Perlovsky, Implementation of Dynamic Logic Algorithm for Detection of EM Fields Scattered by Langmuir Soliton, Chapter #11 in the book “Astrophysics”, ISBN 978-953-51-0473-5, INTECH, 2012.
2. V. Sotnikov, T. Kim, E. Mishin, W. E. Amatucci, G. Ganguli, E. Tejero, T. A. Mehlhorn, and I. Paraschiv. Low frequency plasma turbulence as a source of clutter in surveillance and communication. *Proceedings from the AMOS 2012 Conference*, 2012.
3. E. M. Tejero, V. Sotnikov, G. Ganguli, C. Crabtree, C. L. Enloe, and W. E. Amatucci, NRL Memorandum Report 9489, Approved for publication, October 2013.
- 4.C.L. Enloe, E.M. Tejero, W.E. Amatucci, C. Crabtree, G. Ganguli, and V. Sotnikov, “Effects of neutral interactions on velocity-shear-driven plasma waves”, *Phys. Plasmas*, **21**, 062114 (2014).
- 5.V. Sotnikov, T. Kim, J. Lundberg, I. Paraschiv, and T.A. Mehlhorn, “Scattering of electromagnetic waves by vortex density structures associated with interchange instability: Analytical and large scale plasma simulation results”, *Phys Plasmas*, **21**, 052309 (2014).
- 6.G. Ganguli, E. Tejero, C. Crabtree, W. Amatucci, and L. Rudakov, “Generation of electromagnetic waves in the very low frequency band by velocity gradient”, *Phys. Plasmas*, **21**, 012107 (2014).

Accepted/Submitted for Publication:

1. W. E. Amatucci, C. D. Cothran, E. M. Tejero, D. Blackwell, G. Ganguli, "Laboratory Investigation of Nonlinear Whistler Wave Processes", Talk given at USNC-URSI conference, January 2013 in Boulder, CO.
2. J. Caplinger, V. Sotnikov, A.J. Wallerstein, “Numerical Modeling of High Frequency Electromagnetic Wave Propagations Through Ionospheric Plasma With Randomly Distributed Flute Vortices”, *AGU Fall Meeting, San Francisco, CA, December 2014*.
3. D. Main, J. Caplinger, T. Kim, and V. Sotnikov, “Particle-in-cell simulations of electromagnetic wave scattering from numerically generated Flute-type density irregularities”, *AGU December Meeting, 2014*.

Invited Lectures, Presentations, Talks, etc:

1. V. Sotnikov , T. Kim and J. Lundberg, B. Amatucci, G. Ganguli, E. Tejero, T.A. Mehlhorn, Scattering of High Frequency Electromagnetic Waves in the Presence of Low Frequency Density Irregularities, oral presentation, *APS DPP Fall Meeting, 2012*.
2. V. Sotnikov, T. Kim, J. Lundberg, E. Mishin, W. Amatucci, E. Tejero, G. Ganguli and T. A. Mehlhorn, Low Frequency Plasma Turbulence as a Source of Clutter in Surveillance and Communication, *Poster, AGU Fall Meeting, 3-9 December 2012, San Francisco, CA*.
3. V. Sotnikov, T. Kim, E. Mishin, T. Genoni, D. Rose and D. Welch, Interchange and Flow Velocity Shear Instabilities in the Presence of Finite Larmor Radius Effects, *C/NOFS Workshop, 17-20 June 2013, Albuquerque, New Mexico*.

4. W. E. Amatucci, C. D. Cothran, E. M. Tejero, D. Blackwell, G. Ganguli, "Laboratory Investigation of Nonlinear Whistler Wave Processes", Talk given at USNC-URSI conference, January 2013 in Boulder, CO.
- 5 .V. Sotnikov, T. Kim, J. Lundberg, I. Paraschiv, T.A. Mehlhorn, "Interaction of High Frequency Electromagnetic Waves with Vortex Structures: Comparison of Analytical and LSP Simulation Results", Scheduled for presentation at APS Division of Plasma Physics meeting, New Orleans, LA Oct. 2014.
6. E.M. Tejero, C.L. Enloe, V. Sotnikov, C. Crabtree, E. Gillman, W.E. Amatucci, G. Ganguli, "Investigation of the Scattering of Electromagnetic Signals from Low Frequency Turbulence", Scheduled for presentation at APS Division of Plasma Physics meeting, New Orleans, LA Oct. 2014.
7. V. Sotnikov, "Refraction and Scattering of Electromagnetic Waves in a Plasma with Density Structures", Presented at Plasma Instabilities and Turbulence in Space and Laboratory Plasma Sheaths", Technical Interchange Meeting, Los Angeles, CA July 2014.
8. E.M. Tejero, C.L. Enloe, V. Sotnikov, C. Crabtree, E. Gillman, W.E. Amatucci, G. Ganguli, "Investigation of the Scattering of Electromagnetic Signals from Low Frequency Turbulence", Presented at Plasma Instabilities and Turbulence in Space and Laboratory Plasma Sheaths Technical Interchange Meeting, Los Angeles, CA, July 2014.
9. V. Sotnikov, "Models of Plasma Density Irregularities", JASON Meeting on Artctic Radar Study, San Diego, CA, July 2014.

"Professional activities" and awards

- V. Sotnikov, Convener of Mini-conference "Nonlinear Plasma Effects in Geospace Plasma" at the 54th Annual Meeting of the APS Division of Plasma Physics, Nov 2012, Providence, RI.
- V. Sotnikov, Convener of the Session "Magnetosphere-Ionosphere-Thermosphere Coupling and its Consequences" at the AGU Fall Meeting, December 2012, San Francisco, CA.
- V. Sotnikov, Organizer and Chair of the 1st Workshop on Ionospheric Turbulence, Dayton OH, 2012.
- E. Tejero, Chair of the "Waves in Laboratory Plasmas" session at the 2013 USNC-URSI Conference in Boulder, CO.
- V. Sotnikov, AFRL/RYM award for International Collaboration, 2013.
- V. Sotnikov, Organizer and Chair of the 1st Technical Interchange Meeting on Turbulence in Hypersonic Plasma Flows, UCLA, Los Angeles, CA, 2014.
- V. Sotnikov, Convener of Mini-conference "Nonlinear Plasma Effects in Geospace Plasma" at the 56th Annual Meeting of the APS Division of Plasma Physics, Oct 2014, New Orleans, LO.
- V. Sotnikov, AFRL/RYM Basic Research Award, 2nd quarter, 2014.

LIST OF SYMBOLS, ABBREVIATIONS, AND ACRONYMS

ACRONYM DESCRIPTION

Ω_i	Ion-cyclotron frequency
$T_{i,e}$	Ion, Electron temperature
$V_{Ti,Te}$	Thermal ion, electron velocities
n_0	Background density
κ_N	Density scale length
$\rho_{e,i}$	Electron, ion gyroradius
v_{en}	Electron-neutral collision coefficient
ω_{ce}	Electron-cyclotron frequency
ω_{pe}	Electron plasma frequency
ω_{pi}	Ion plasma frequency
ω_α	Lower-hybrid resonance
\mathbf{B}	Magnetic field
b	Flute mode
c	Speed of light
CSWAP	Cost, size, weight, and power
\mathbf{E}	Electric field
e	Charge of electron
EM	Electro-magnetic
ESF	Equatorial spread F
f	frequency
FFT	Fast-Fourier Transform
FWHM	Full width at half maximum
g	Acceleration due to gravity
h	Characteristic size
k	Wave vector
LE	Electric field scale length
LSP	Plasma simulation software
m	Electron mass
M	Ion mass
MHD	Magneto-hydrodynamics
NGOTHR	Next generation over the horizon radar
OTH	Over the horizon
P	Probability function
PIC	Particle in Cell
R	Dispersion length
\mathbf{r}	Position vector
t	Time
TE	Transverse-Electromagnetic
V,U	Particle velocity, drift velocities
VLF	Very low frequency
Z	Ionization
α	Scattered angle
β	Plasma beta
τ	Scale time

ACRONYM DESCRIPTION

Φ	Electric potential
δn	Density perturbation